UAM
UNIVERSIDAD AUTONOMA
DE MADRID

Science Faculty

Department of Applied Physics

Atomic force microscopy dynamic modes for the quantification of nanomechanical properties: From polymers to membrane proteins

A thesis submitted to the Universidad Autónoma de Madrid in accordance with the requirements of the degree of

Doctor in Philosophy by:

Alma Eva Pérez Perrino

Supervised by

Prof. Ricardo García García

Instituto de Ciencia de Materiales de Madrid

Consejo Superior de Investigaciones Científicas

December 2016

"Comienza haciendo lo que es necesario,
después lo que es posible
y de repente estarás haciendo lo imposible"
San Francisco de Asís

Agradecimientos

Como dijo un señor muy sabio, las tres palabras que más deberíamos repetir son: por favor, perdón y gracias, así que ahora voy a hacer lo propio con esta última.

Ricardo, cuando me hiciste la entrevista me preguntaste qué pensaba yo que era hacer una tesis, recuerdo muy vagamente mi respuesta pero tu cara decía claramente que yo no tenía ni idea, y en efecto, ni la más mínima idea. Muchas gracias por darme la oportunidad de hacer la tesis en tu laboratorio y por darme las herramientas necesarias y más para entender el mundo científico.

Estoy muy muy agradecida al grupo Forcetool. A lo largo de estos años mucha gente ha ido y venido pero siempre me ha sorprendido encontrarme con gente muy buena (no sólo científicamente hablando) que han compartido su experiencia conmigo, Marco, Jorge, Horacio, Elena, Amir, Fran y Ryu y los nuevos, Pablo, Carlos A., Carlos G., Stefano, Arancha y Manuel que han traído aire fresco al grupo. Elena, tú fuiste la que me enseñaste prácticamente todo lo que sé de AFM, muchas gracias por tu paciencia y por tu disponibilidad, has sido una pieza clave de esta tesis. Fuera del grupo también he conocido a gente muy especial que me ha apoyado y me ha dado ánimos siempre que lo he necesitado, Guilherme, muchas gracias por todo.

Dani y Andra, mi piñita, habéis sido uno de mis grandes apoyos durante este tiempo. Gracias por estar ahí cada vez que os he necesitado. Dani, tu manera de ver y analizar las cosas me ha enseñado a ser más observadora y, sobre todo, menos vaga mentalmente! Andra, me siento muy afortunada de haberte conocido y de haber recorrido este camino a tu lado, nuestras miles de conversaciones, desde calibrar la punta del AFM, pasando por el papel del científico en el mundo, hasta qué habrá hecho hoy Kim Kardashian, han hecho inigualable esta experiencia, la volvería a repetir mil veces si sé que tu vas a estar allí (y decir eso de una tesis, ¡es como ser masoca!).

Beguii, ¡qué suerte haber empezado en microelectrónica a tu lado! Esa "coincidencia" ha fortalecido tanto nuestra amistad como mi admiración hacia tu forma de ver la física, gracias por estar ahí siempre y por todas las cervezas y conversaciones que han hecho que la – tesis se haya hecho más llevadera.

Y a toda la gente que día a día, fin de semana a fin de semana han aguantado mis quejas proporcionándome risas, ánimos y muchísimos momentos de felicidad: friksicos, chicos, muchas gracias! Aún nos quedan muchas horas pi por compartir, a los jodidos fanegas que ya sea en los perros o una paella en casa de Mayte ;) siempre habeis estado ahí apoyándome e intentando entender qué hago. Muchas gracias a la gente de mundo viejuno por todos los consejos que me habéis dado y todo el apoyo que me disteis en mis primeras conferencias.

Un gracias especial al grupo de Jesús, y a los padres blancos, Manu, Eugenio y Óscar, todos habéis estado en este camino apoyándome y me ayudáis cada día en mi esfuerzo por ser mejor persona.

A mis hermanas, que con sus: ¡Tú eres la mejor! y ¡La científica de la familia! me habéis dado todo el cariño y la seguridad que muchas veces me falta, muchas gracias por cuidarme tanto y por las chorradas que me hacen reír hasta que me duele la barriga. Gracias también a mis sobris, Diego y Sofía, que me han sacado mil sonrisas con sus bromas sobre golpearme con microscopios y sus preguntas físicas! Muchas gracias también a Agustín ¡creo que eres el único de la familia que se entera de lo que hago! Y por último a mis padres, papá, mamá, gracias por quererme, gracias por todo el esfuerzo que habéis hecho cada día para que yo haya llegado a este punto. Gracias papá porque al final con tu sueño de que tus hijas tuvieran una carrera has conseguido empujarnos y darnos la educación que querías. Gracias mamá porque eres una heroína, cada día de mi vida has hecho miles de pequeñas cosas que me han hecho llegar hasta aquí. Ojala algún día pueda llegar a ser la mitad de buena que tú.

List of symbols

k	Cantilever spring constant
E	Material Young modulus
b	Width
h	Thickness
l	Length
ω_0	Angular resonance frequency, given by $\omega_0 = 2\pi f_0$
Q	Quality factor
k_B	Boltzmann constant
T	Temperature
F_{ts}	Tip-sample interaction force
z_0	Cantilever deflection
f_0	Free resonance frequency
A_0	Free oscillation amplitude
A_{sp}	Set-point amplitude
A'	Oscillation amplitude
Δf	Frequency shift
τ	Transient time
V_{exc}, $V_{exc,0}$	Far/Free Driving force amplitude in Chapter 3

ΔV_{exc}	Driving force amplitude shift in Chapter 3
E_{eff}	Effective Young modulus
R	Tip radius
δ	Indentation
E_s	Sample´s Young modulus
E_t	Tip´s Young modulus
σ	Stress
F	General force term
ε	Strain
v_t	Tip poisson ratio
v_s	Sample poisson ratio
z_c	Cantilever-sample distance (piezo displacement)
a	Contact radius
d_m	Tip-sample distance
$D_-^{1/2}F(z)$	Half derivative of the force
$I_-^{1/2}F(z)$	Half integral of the force
Δf_n	nth eigenmode frequency shift
A_n	nth eigenmode oscillation amplitude
A_{0n}	nth eigenmode free oscillation amplitude
k_n	nth eigenmode cantilever spring constant

a_0	Intermolecular distance
η	Viscous coefficient
f_{0n}	nth eigenmode free resonance frequency
F_{0n}	nth eigenmode free driving force amplitude
ΔF_{0n}	nth eigenmode free driving force amplitude shift

List of acronyms

AFM   Atomic Force Microscopy

NSOM   Near-field Scanning Optical Microscopy

PALM   Photo-Activated Localization Microscopy

STM   Scanning Tunneling Microscopy

SPM   Scanning Probe Microscopy

OBD   optical beam deflection

PID   Proportional, Integral and Differential controller

HOPG   Highly Ordered Pyrolytic Graphite

AM-AFM   Amplitude Modulation Atomic Force Microscopy

FM-AFM   Frequency Modulation Atomic Force Microscopy

DAM   Drive Amplitude Modulation

UHV   Ultra-High Vacuum

PLL   Phase-Locked-Loop

CA-FM   Constant Amplitude in Frequency Modulation

CE-FM   Constant Excitation in Frequency Modulation

UFM   Ultrasonic Force Microscopy

DART   Dual AC Resonance Tracking

THC	Torsional Harmonic Cantilever
DLVO	Derjaguin-Landau-Verwey-Overbeek theory
IgM	Immunoglobulin M
PAMAM	Polyamidoamine
DNA	Deoxyribonucleic Acid
PBS	Phosphate Buffered Solution
APTES	3-aminopropyl triethoxysilane
BEHC	Bottom Effect Hertz Correction
F_{ab}	Antigen binding fragment
F_c	Crystallisable fragment
oSPL	oxidation Scanning Probe Lithography
SiO_2	Silicon Oxide
Si	Silicon
PS	Polystyrene
LDPE	Polyolefin elastomer (ethylene-octene copolymer)
PDMS	Poly-dimethylsiloxane
PS-b-PMMA	Polystyrene-b-poly(methyl methacrylate)
PM	Purple Membrane
Ce-RPF-8	Cerium Rare-earth Polymeric Framework 8
MOF	Metal Organic Framework

BR   Bacteriorhodopsin protein

CP   Cytoplasmic side

EC   Extracellular side

Abstract

The atomic force microscope (AFM) has been established as the key tool for the development and the study of Nanoscience and Nanotechnology fields. The expansion of AFM configurations has increased its versatility and, now, it is possible to obtain high resolution images, meaning atomic and molecular resolution, on a broad variety of materials such as semiconductors, metals, polymers or biomolecules. In addition, the AFM works in all environments, from vacuum to liquid.

The AFM has evolved as a response to the need to provide non-invasive and high resolution methods for imaging surfaces and interfaces. These methods provide simultaneous information about different material properties which are needed to understand heterogeneous interfaces such as solid-liquid interfaces, polymer interfaces, energy-storage devices, cells or membrane proteins and to develop materials with tailored properties at the nanoscale. Ideally, those methods should complement the high spatial resolution of AFM with the following properties: (1) Material characterization independent of the probe properties. (2) Quantitative. (3) Minimal tip and sample preparation. (4) Compatible with high speed data acquisition and imaging. The approaches most widely used so far are the combination of force curves at each point of the surface with contact or near contact AFM imaging configurations. However, these approaches have some limitations, 1) The data acquisition speed is limited by the large number of data points per pixel needed to obtain accurate values of the mechanical properties, 2) The use of the same cantilever to measure complex surfaces is restricted since the sensitivity of the force curve depends on the cantilever force constant, 3) The expressions used to retrieve the mechanical properties are not analytical or there is a lack of theoretical approaches used to determine those expressions. In order to address these limitations, the development of nanomechanical spectroscopy methods has been inspired by bimodal excitation in combination with the main dynamic modes, amplitude modulation and frequency modulation.

This doctoral thesis focuses on the main dynamic AFM configurations: amplitude modulation AFM (AM-AFM), frequency modulation (FM-AFM) and bimodal excitation. The thesis is divided in five chapters and has two main goals, 1) to develop new AFM techniques based on single or bimodal excitation, that connect the experimental observables and the properties of the material. The development of the AFM techniques is specifically focused on the application of the techniques in liquid for the study of the nanomechanical properties of biomolecules and biomaterials in their native environment; 2) to study the established dynamic AFM modes and compare their performance for imaging biomolecules in air and liquid in a non invasive manner.

- In the first chapter, a basic introduction to the AFM is presented. The elements that compose the atomic force microscope along with the principal operating modes that will be applied during the progression of this thesis are described.

- In the second chapter, a study of the operational factors that control the applied force on soft matter samples in the main dynamic AFM operation modes is made. The study is performed in air and liquid environments on several biological samples. Additionally, a theoretical expression to calculate the peak force in FM-AFM measurements performed in air is provided.

- In the third chapter, a force microscopy method to determine the stress-strain curve of a single and isolated protein in physiological-like conditions is described. This approach has a force sensitivity of 5 pN and, lateral and vertical resolutions, respectively, of 2 and 0.1 nm.

- In the fourth chapter, the essential steps for the implementation of the bimodal FM-FM AFM configuration in a commercial microscope are described.

The method is applied in air to calculate the elastic modulus and the viscosity of several polymers with variations in the elastic modulus of near four orders of magnitude. The technique also allows the determination of some other operational parameters, such as the indentation and the peak force.

- In the fifth chapter, bimodal AFM with the AM-FM configuration is developed and applied in liquid to provide nanomechanical maps of biological membranes in liquid with molecular resolution. The method is also applied on muscovite mica and electric conducting Metal Organic Framework (MOF). The atomic and molecular resolutions are shown in both the topography and the nanomechanical maps.

Resumen

La microscopía de fuerzas (AFM por sus siglas en inglés) se ha establecido como una herramienta clave para el desarrollo y estudio de la nanociencia y la nanotecnología. El desarrollo de diversos modos de operación de la micropalanca ha aumentado la versatilidad de la microscopía de fuerzas para visualizar con resolución atómica, molecular o nanométrica una gran variedad de superficies y materiales como semiconductores, metales, polímeros o biomoléculas. Además, el AFM puede funcionar tanto en vacío, como a presión atmosférica o en líquido.

El AFM ha evolucionado para dar una respuesta a la necesidad de métodos de alta resolución y no invasivos para medir superficies e intercaras. Estos métodos proporcionan información simultánea de las distintas propiedades que son necesarias para entender materiales como polímeros, dispositivos para almacenamiento de energía, células o proteínas y para el desarrollo de materiales con propiedades personalizadas en la nano escala. Idealmente estos métodos deberían complementar la alta resolución proporcionada por el AFM con las siguientes propiedades: (1) Caracterización del material independientemente de las propiedades de la sonda del AFM. (2) Medidas cuantitativas. (3) Preparación de punta y muestra mínima. (4) Compatible con alta velocidad de adquisición de datos y de imagen. Hasta ahora, los métodos desarrollados utilizaban la combinación de curvas de fuerza en cada punto de la superficie de la muestra con configuraciones de AFM en contacto o fuera de resonancia. Sin embargo, estos métodos tienen algunas limitaciones, (1) Debido al gran número de puntos por pixel, la adquisición de los datos y de la imagen simultáneamente es más lento. (2) El uso del mismo cantiléver para medir superficies con distintas propiedades no es posible debido a que la sensibilidad de las curvas de fuerzas depende de la constante de fuerzas del cantiléver. (3) Las ecuaciones desarrolladas para obtener las propiedades mecánicas no son analíticas, aumentando el tiempo de adquisición de los datos.

En algunos casos la teoría para el desarrollo de estas ecuaciones no está explicada. Todas estas limitaciones han llevado a la comunidad de AFM a desarrollar métodos basados en la excitación bimodal en combinación con los principales modos dinámicos, amplitud modulada y frecuencia modulada.

Esta tesis doctoral se centra en las distintas configuraciones de AFM con los modos dinámicos: amplitud modulada (AM-AFM), frecuencia modulada (FM-AFM) y excitación bimodal. La tesis se divide en cinco capítulos y tiene dos objetivos principales, a) El desarrollo de nuevas técnicas de AFM, basadas en excitación simple o bimodal, que permiten conectar los observables experimentales con las propiedades del material. El desarrollo de las técnicas de AFM está especialmente enfocado en la aplicación de las técnicas en líquido para el estudio de las propiedades mecánicas de biomoléculas y biomateriales en su medio nativo; 2) El estudio de los modos dinámicos del AFM ya establecidos y comparar su comportamiento para medir biomoléculas en aire y en liquido de forma no invasiva.

- En el primer capítulo se presenta una introducción básica del AFM. Los elementos que componen el microscopio son introducidos junto con los modos de operación del AFM que serán utilizados en la tesis.

- En el segundo capítulo, se estudian los factores que controlan la fuerza ejercida por la punta sobre una muestra blanda en los principales modos dinámicos de operación del AFM. El estudio se ha realizado en aire y en líquido sobre muestras biológicas. Además, se ha proporcionado una ecuación para calcular la fuerza pico aplicada en FM-AFM en función de los parámetros operacionales en aire.

- En el tercer capítulo se describe un método para determinar la curva de fuerza-deformación de un anticuerpo de tipo Inmunoglobulina M (IgM) en condiciones fisiológicas.

Este método tiene una sensibilidad en la fuerza de 5 pN y resoluciones laterales y verticales de 2 y 0.1 nm, respectivamente.

- En el cuarto capítulo se presentan los pasos principales para la implementación de la configuración FM-FM con excitación bimodal. El método es aplicado en aire para calcular el módulo elástico y la viscosidad de varios polímeros con cambios en el valor de modulo elástico de casi cuatro órdenes de magnitud. Esta técnica también permite determinar otros parámetros operaciones como la indentación y la fuerza pico.

- En el quinto capítulo se presenta la configuración AM-FM con excitación bimodal. Este modo se aplica en líquido para calcular los mapas de elasticidad de membranas biológicas con resolución molecular. El método también se aplica en mica y en redes de materiales organometálicos. Tanto los mapas de topografía como los de elasticidad muestran resolución atómica y molecular.

Contents

Chapter 1

Introduction to Atomic Force Microscopy

1.1 Introduction

The atomic force microscopy (AFM) was invented in 1986 [1] by Gerd Binnig, Calvin F. Quate and Christoph Gerber. One could be easily tempted to look back and wonder how many advances its development has brought in this 30 years. It might be intimidating to see all the goals that have been achieved, from the chemical identification of atoms [2] to the visualization of the myosin, responsible of the contraction of our muscles, walking on an actin filament [3] not to mention the first image of a dust grain from a comet [4]. The accomplishment of these scientific breakthroughs might lead us to the thought that there is nothing left to achieve in the field but, on the contrary, these are the stimuli that drive us in our quest for new developments in the AFM field.

Scientists have tried to get a look on things which are invisible to the human eye. Microscopic is the quality of those objects which are characterized as being too small to be seen with the naked eye, thus in order to see microscopic things we need something between the eye and the specimen to be seen.

It is this questionable curiosity which makes us develop things that enable us to discover the world around, thus all the developments built so far (spectacles, microscopes, big telescopes…) are the results of this search. Resolution is described as the ability to distinguish between two objects and this definition led us to another description which is the resolution limit. We cannot discriminate between two points if we are looking at them with something bigger than the distance between them. When using light as the tool to visualize things, the resolution is determined by Abbe´s equation. The first microscopes used the combination of light and lenses to enlarge and form the optical image of a specimen, but, as mentioned above, optical microscopes are limited by the wavelength of light, being its resolution limit in the order of hundreds of nanometers.

To go deeper, the use of another tool, instead of light, is necessary. Ernst Ruska and Max Knoll discerned the way to overcome this limitation: the use of electrons. In 1931, they designed the first prototype of a scanning electron microscope. Other advances in the field of optical microscopy such as confocal microscopy, Near-field Scanning Optical Microscopy (NSOM/SNOM) or Photo-Activated Localization Microscopy (PALM), have enhanced the resolution limit in optical microscopes to the order of tens of nanometers [5-7].

The next big advance in the microscopy field was the development of the Scanning Tunneling Microscope (STM) in 1981 [8, 9]. The STM belongs to the Scanning Probe Microscopy (SPM) techniques. SPM techniques use the local interaction between a probe and the sample surface. The probe scans the surface along parallel lines and the detection system measures the local interaction in each point. One of the key steps in the development of SPM techniques was the use of piezoelectric materials. These materials are characterized by the piezoelectric effect, which is a reversible mechanical stress produced in the material due to an electric potential across it, or vice versa.

This mechanical stress can be of the order of angstroms and allows very accurate movements in the x, y and z axis.

The large variety of SPM techniques comes from the different interactions which can be measured by the probe. These interactions should have a dependence on the probe-sample distance. Based on this fact the STM is using, as interaction parameter, the tunneling current. The tunneling effect is characterized by the generation of an electric current between two conductive materials in an insulating medium when they are very close. The fact that the tunneling current between the conductive tip and the conductive sample grows exponentially with their closeness provides the fundamental feedback parameter to measure the sample surface.

Following the steps of the STM, Binnig, Quate and Gerber introduced the atomic force microscopy (AFM) in 1986. In this new instrument, instead of measuring the tunneling current, the interaction force between the probe and the sample surface is detected. In this way some of the STM requirements, such as the use of conductive samples or special environments and temperatures, are overcome. The interaction forces are measured by means of a cantilever with a sharp tip probe at its free end. The sharp tip is characterized by a radius ranging from 1 to 50 nm or it can be replaced by a polymeric sphere up to 3 μm radius depending on the AFM application. The tip interacts with the sample surface causing a deflection of the tip-cantilever ensemble. This change in deflection accounts for the tip-sample interactions which carry the information to reconstruct the sample surface and measure mechanical, electric and magnetic properties.
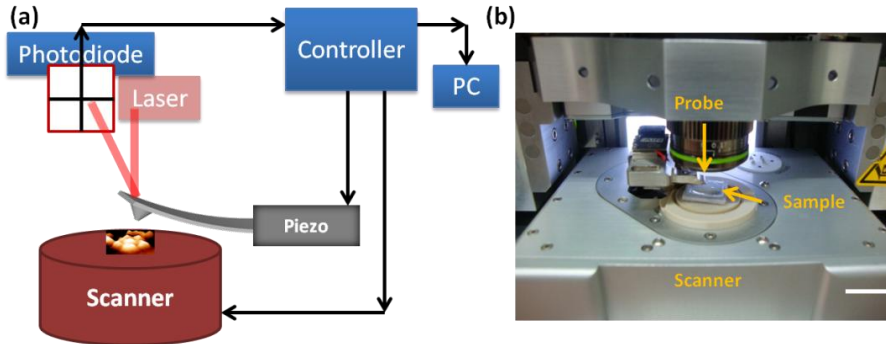
Figure 1.1. AFM main elements. (a) Schematic representation of the AFM with labeled main components. The deflection produced on the tip is reflected to the photodiode which receives the signal and sends it to the controller. The controller compares the signal with the set-point value chosen by the user and sends the corresponding order to the piezo actuator for the cantilever excitation and to the scanner to vary the z axis position. (b) Real picture of the AFM fabricated by Asylum Research with labeled main components (scale bar, 15 mm).

The first AFM used an STM to measure the tip deflection and the sample was placed in the vertical axis. This configuration restricted the measurement of several samples as well as hindered the spread of the technique. Since its invention, several advances regarding the components of the microscope have given the AFM its robustness and flexibility. In the next section, some of the most common elements of an AFM are presented.

1.2 The instrument

The scheme of an AFM is depicted in Figure 1.1 (a) with the main components. The scanner is usually placed on the lower part of the system but in other setups it can be placed in the upper part. When the scanner is in the lower part, the sample follows the movements of the scanner while in the other setup, the cantilever does.

The scanner is made of a piezoelectric material that allows precise movements in the horizontal *xy* axis and in the vertical *z* axis.

The cantilever is located in the upper part of the system, where the optical system is also placed. This is called the head of the microscope. The way the cantilever is monitored to scan the surface sample gives rise to the different operation modes. In the dynamic modes the cantilever can be excited at a certain resonance frequency. The excitation is produced by a piezo actuator when it is acoustically excited [10, 11] but there are also another techniques, such as magnetic [12] or photothermal excitation [13] to be applied in liquids.

As mentioned before, the operating principle of AFM is based on the local interactions between the tip and the sample surface. While scanning the surface, these local interactions produce small changes in the cantilever deflection, the smallest in the order of Å in distance, which corresponds to 10^{-12} N in force. The deflection is detected with the help of a laser beam focused on the back of the cantilever and reflected to a photodiode (Figure 1.1). The photodiode is divided in four sections so that it can register the flexural or the torsional changes of the tip. This optical detection method is called optical beam deflection (OBD) [14], it is the most widely used but there are some other techniques to calculate the deflection of the cantilever such as interferometric techniques [15-17].

The proportional, integral and differential (PID) controller detects the signal recorded by the photodiode and calculates the necessary changes to keep the feedback parameter, either in the *z* axis or in the cantilever dynamics, and scan the sample. It will send the information to the scanner, to the cantilever as well as to the computer. The computer processes the signal from the controller and creates the images in a visual interface where the user interacts with the microscope and chooses the operational parameters.

In the next section, the essential steps needed to obtain an AFM image are presented. The steps here will be presented with a general perspective without taking into account the operation mode.

1.2.1 Steps for taking an AFM image

The first step is the sample preparation. The preparation will be different if the measurement is performed in air or in liquid. In both cases the sample needs to be fixed to the sample holder and this is done by attaching the sample to a metal disk. The way to do this will depend on the environment used to measure the sample. For measurements in air, the fixation can be done with double-sided tape, silver paints or regular glue but for measurements in liquid it requires a more complex preparation. To obtain high resolution images, atomic or molecular, the sample needs to be fixed to the metal disk. When measuring in liquid, the liquid is likely to get between the sample substrate and the metal disk. To avoid this, Teflon disks are used. With the hydrophobic Teflon disks we prevent the liquid from getting between the substrate and the metal disk. But, even with the Teflon disk, we still have the problem of fixing the substrate to the Teflon disk. A possible solution is the use of biocompatible glue. This kind of glue hardens in contact with water and does not contaminate the sample. If this type of glue is not available, it is also possible to use two component epoxy adhesives. Typical substrates are muscovite mica, silicon wafer or Highly Oriented Pyrolytic Graphite (HOPG). The use of one instead of another will depend on the kind of biomolecules we want to measure and how they interact with the substrate.

The next step is the tip and laser positioning. The tip is placed on the cantilever which, in turn, is on a chip to facilitate the correct placing. The appropriate choice of the cantilever is a key point for proper measurement. The use of a given cantilever will be determined not only by the kind of sample we want to measure but also by the mode we will use to perform the measurement.

Once the cantilever is placed over the sample, the laser has to be aligned. This alignment consists of two steps. The first step requires the positioning of the laser on the cantilever so that the signal-noise ratio is maximized. The second step is the selection of the zero deflection for the photodiode. Both steps will be handled by the user but some instruments have an automatic zero deflection option for the photodiode (i.e Cypher).

The next step is the approach of the tip to the sample surface. Case 1 and case 2 in Figure 1.2 depict the approach performed by moving the motors and the piezoelectric. The steps are automatically calculated by the software once the user has given a set-point value. This value will indicate when the tip has reached the sample and the motors will stop. Depending on the type of sample and the kind of cantilever this procedure can be more or less effective and, probably, it has to be repeated due to the so-called "false engage". This happens when the tip reaches the set-point value due to the hydrodynamic damping or long-range attractive forces but is not close to the sample surface. In this case, the parameters can be calculated again and a new set-point can be chosen.

Finally, we can start acquiring an image of the sample. The essential parameters are the scan size, the number of pixels and the scan speed. Once the tip is scanning another two parameters take action, the integral and proportional gains of the PID controller. They are selected on a trial-and-error basis and depend on the topography of the sample and the feedback mechanism.

1.2.2 Calibration

For the correct measurement and interpretation of the images in AFM some parameters have to be calibrated. Here, it is shown how to calibrate some generic parameters.

- Piezoelectric sensitivity. The expansion or contraction of the piezoelectric actuators give rise to the *x*, *y* and *z* values of the images. Thus, an inaccurate calibration of these values could generate erroneous measurements. Each microscope has a procedure to calibrate the piezoelectric actuators but in all of them calibration grids are used.

- Photodiode sensitivity. The photodiode transforms the light in a voltage signal. To convert this voltage into *nm* of tip deflection it is necessary to calibrate the photodiode sensitivity. The photodiode sensitivity provides information about the deflection of the tip in *nm/V*. The calibration has to be done on a hard surface, in such manner that the surface does not deform with the cantilever indentation. Therefore, each *nm* the piezoelectric actuator has moved corresponds to 1 *nm* of deflection in the cantilever. The photodiode sensitivity in contact mode will be given by the inverse of the slope of a force curve taken in contact mode. In addition, the photodiode sensitivity in dynamic mode has to be measured as well. To calculate the photodiode sensitivity in dynamic mode, two approaches can be used as follows: first it can be calculated from the slope of the amplitude versus piezoelectric distance curve, or some theoretical approximations can be applied to transform the sensitivity in contact mode to the sensitivity in dynamic mode [18, 19].

- Spring constant. There are three different ways to obtain the cantilever spring constant.

First, the static force constant can be calculated from the spring constant equation for a beam:

$$k = \frac{3Ebh^3}{4L^3} \tag{1.1}$$

where E is the cantilever´s Young modulus, and b, h y L the width, the thickness and the length, respectively.

Unfortunately, some of these parameters are not always available and the use of scanning electron microscopy images of the tip to calculate them is needed.

Second, the Sader method can be employed [20, 21]. By recording a resonance curve in air, the resonance frequency, ω, and the quality factor, Q are extracted. With these parameters, the width, b, and the length, L, of the cantilever, we can use the next equation:

$$k = \frac{\pi}{16} \rho b^2 Q L \omega^2 \Gamma''(\omega) \tag{1.2}$$

which relates the spring constant of the cantilever with the hydrodynamic function at the resonance frequency, $\Gamma''(\omega)$, in a given medium of density ρ. This equation is only valid for rectangular cantilevers. In 2012, Sader and coworkers [22] calculated the hydrodynamic function for irregular and non-rectangular AFM cantilevers as well as the conversion factors for the static and dynamic spring constants of these cantilevers.

Third, the thermal noise method can also be used [23, 24]. It is based on the equipartition theorem and establishes that for a free cantilever at equilibrium with the environment, the kinetic energy stored in the system is equal to $k_B T/2$:

$$\frac{1}{2} k \langle z^2 \rangle = \frac{1}{2} k_B T \tag{1.3}$$

where k is the spring constant of the cantilever, $\langle z^2 \rangle$ is the mean deflection of the cantilever caused by thermal vibrations, k_B is the Boltzmann constant and T the temperature. $\langle z^2 \rangle$ is calculated from the thermal noise spectrum plot and the photodiode sensitivity by a Lorentz function fit.

When calibrating the tip to obtain the sensitivity of the photodiode along with the spring constant we have to be careful since by performing force curves the tip is likely to get damaged. Even though the calibrated parameters of cantilevers from the same cantilever box are almost steady, to perform quantitative measurements the parameters for each cantilever need to be calculated. In order to avoid irreversible tip damaging, the force curve will be acquired at the end of the experiment.
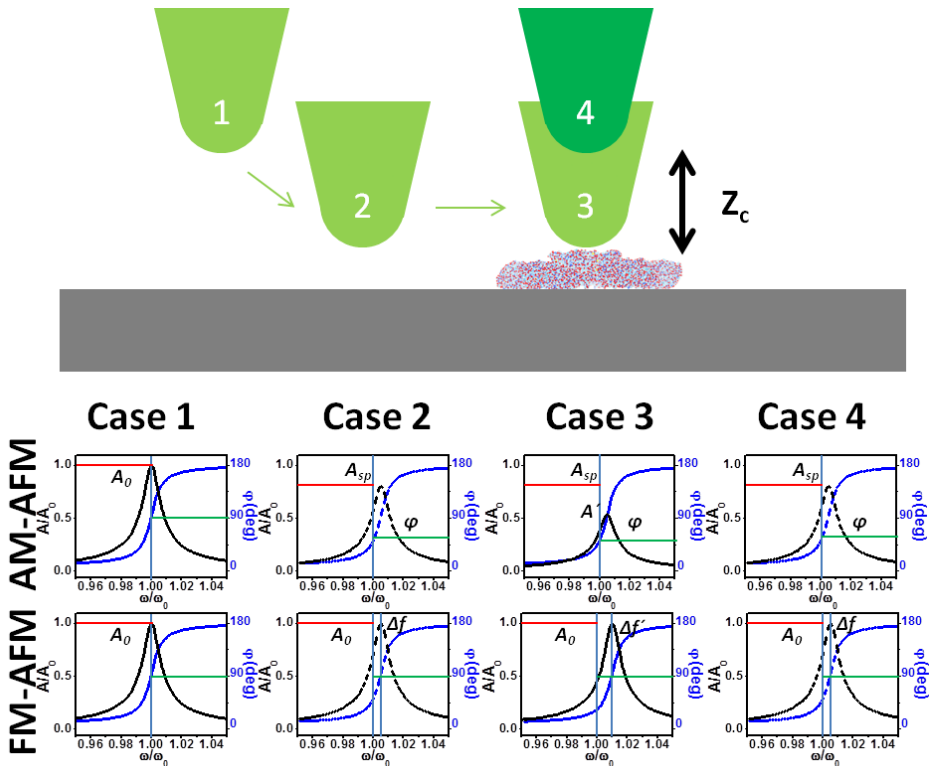
Figure 1.2. Scheme of the cantilever dynamics in the approach and scan steps. The different cases display the changes in the cantilever dynamics. Case 1 depicts the tip above the sample and no interaction force. The cantilever is excited at its resonance frequency, f_0, and it is characterized by a free amplitude A_0, as well as a phase shift of 90º between the excitation and the response signal. The z-piezo starts the approach of the tip to the sample and when the cantilever interacts with the surface (Case 2), the cantilever dynamics changes as follows: in AM-AFM the amplitude decreases and in FM-AFM the resonance frequency shifts (the graph shows resonance frequency shifts caused by repulsive interactions). Once the cantilever has reached the set-point value provided by the user, A_{sp} for AM-AFM and Δf for FM-AFM, the z-piezo remains at this position and the cantilever starts scanning the surface. Case 3 depicts the cantilever dynamics when the tip encounters a variation in topography. The tip-sample distance is less and in AM-AFM the amplitude reduces to $A´$ and in FM-AFM the frequency shift increases to $\Delta f´$. In Case 4, the feedback compensates for the change in $A´$ and $\Delta f´$ by varying the tip-sample distance until the cantilever dynamics is the same as in Case 2.

1.3 Operation Modes

The promising capabilities of AFM, such us measuring in physiological solution or high-resolution imaging of biomolecules, inspired the AFM community to develop new devices and techniques focused on biological research. All these developments have been applied, for instance, to obtain high resolution images or to study the elasticity of soft biological samples like cells, DNA or proteins.

In this section some of the main AFM modes are presented. They will be divided in two main groups, contact mode and dynamic modes. Within the dynamic modes, bimodal atomic force microscopy will be introduced as well.

1.3.1 Contact mode

Contact mode is the simplest mode in AFM and the first mode developed. This mode is called contact mode because the tip is in contact with the surface while scanning. The feedback parameter to track the topography is the deflection of the cantilever or the average cantilever-sample distance. The cantilever approaches the sample (see Case 1 in Figure 1.2) and when the contact between the tip and the sample is produced, the cantilever deflects until reaching the corresponding set point deflection (Case 2 in Figure 1.2). The cantilever scans the sample at this set point parameter but when the tip encounters a difference in composition or topography (Case 3 in Figure 1.2), a change in the deflection is caused and in order to keep the set point value constant, the feedback system will move the cantilever upwards or downwards to compensate the deflection shift (Case 4 in Figure 1.2). Regarding the control of the applied force in contact mode, when the tip approaches to the sample with no driving force acting on the cantilever, the cantilever will follow Hooke´s law $F_{ts} = -kz_0$, where z_0 is the deflection accounting for the interaction forces, F_{ts}. Therefore, in contact mode the sensitivity in the applied force is directly dependent on the cantilever deflection sensitivity.

Since the tip is always in contact with the sample, the applied forces are usually in the range of hundreds of pN or, even, nN, so special attention must be paid for the correct selection of the cantilever spring constant. Although it will depend on the kind of sample to be measured, it can be roughly argued that the k has to be softer than the bonds between atoms on the tip and the sample, so conventional values are 0.01-10 N/m.

In this mode the lateral forces caused by the lateral movement of the tip against the sample are high and are not well controlled by the system, thus tip and sample damage are likely to happen. Friction force microscopy has taken advantage of these lateral forces [25] and has studied friction, adhesion and wear forces at the nanoscale [26, 27].

The first images showing molecular resolution of membrane proteins in liquid were obtained in contact mode [28]. Contact mode has been routinely used to obtain molecular resolution of membrane proteins (see Figure 1.3) but molecular resolution on single proteins is not able in contact mode since the applied lateral forces are higher than the forces that maintain the protein fixed to the surface. In order to overcome this disadvantage the dynamic modes were developed.
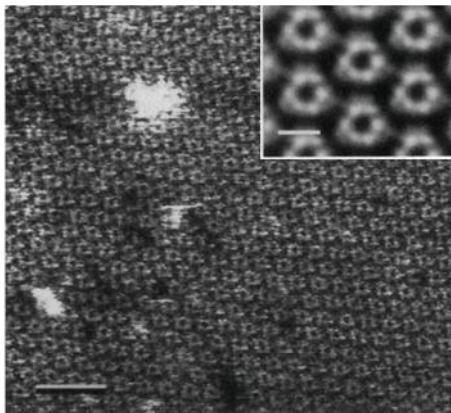

Figure 1.3. Molecular resolution AFM image on Purple membrane, adapted from [28].

1.3.2 Dynamic modes

In dynamic modes of operation the cantilever is oscillated perpendicular to the sample. The different parameters that can be used as topography feedback and the different channels that can be extracted from the cantilever dynamics give rise to the variety of dynamic modes developed. Here, basic methods, amplitude-modulation (AM) and frequency-modulation (FM) will be introduced, along with Hybrid AFM mode, also called drive amplitude modulation (DAM), which presents mixed characteristics of AM and FM. Bimodal AFM will be also introduced in this section.

Amplitude modulation AFM

In amplitude modulation atomic force microscopy (AM-AFM) the cantilever is excited at a fixed frequency [29]. Normally, this driving frequency coincides with the first mode of the cantilever at which the oscillation amplitude is maximized. The cantilever movement is then characterized by the oscillation amplitude and the phase shift between the driving signal and the response. When the cantilever approaches the sample, the elastic and inelastic interaction forces cause a change in the amplitude and in the phase of the oscillation; the change in the oscillation amplitude will provide the feedback parameter to follow the topography of the sample, usually called set-point amplitude, $A_{sp}=A'/A_0$. This is shown in Figure 1.2, the tip approaches to the sample surface and when the oscillation amplitude reaches the value fixed by the user, A_{sp} (Case 2), the tip starts scanning the sample surface. When the tip detects a change in topography or in the compositional properties of sample, the oscillation amplitude changes (see Figure 1.2, Case 3), and the feedback system will move the piezo upwards or downwards until the oscillation amplitude is again equal to A_{sp} (Case 4).

This change in amplitude does not occur instantaneously when there is a change in tip-sample interactions, but it is dependent on the oscillatory signal, the resonance frequency, ω_0, and the quality factor, Q, of the cantilever, with a transient time, τ, defined by [30]:

$$\tau = \frac{2Q}{\omega_0} \tag{1.4}$$

This constraint makes AM-AFM imaging in ultra-high vacuum (UHV), where Q factors are around 10000, very slow and, hence, unsuitable.

AM-AFM has been applied in air and liquid and has provided atomic and molecular resolution. As previously mentioned, high resolution images of single proteins in contact mode were impossible to obtain because of the large lateral forces exerted by the tip. Images of single proteins in air and liquid environments were obtained in AM-AFM (see figure 1.4 (a)) [10, 31], but high resolution images, meaning molecular and atomic resolution, were only feasible by using very small oscillation amplitudes, in the range of 1-2 nm [32]. In 2010, Stellaci and collaborators acquired atomic resolution images on several crystals and self-assembled monolayers by using very small amplitudes (see figure 1.4 (b)) [33]. When the tip is oscillating at such small amplitudes, it interacts almost constantly with the interfacial liquid and it is never in contact with the sample. The process to obtain molecular resolution also involved the application of very small amplitudes [34] (see figure 1.4 (c)). But one of the greatest achievements in amplitude modulation was the development of high speed AFM. The attempt to image biological dynamic processes was largely pursued since the development of AFM [35, 36] but the limitation in the speed of the feedback loop to maintain a constant amplitude while imaging prevented atomic force microscopy measurements from the increment in scan speed.

Finally, Ando´s group improved all the technical limitations in the feedback system to increase the scan speed without compromising the applied force. The first thing they did was to develop small cantilevers, as the one shown in Figure 1.4 (d). These cantilevers have a high resonant frequency to reduce the feedback bandwidth, but a low spring constant, necessary for imaging biological samples with small applied forces [37, 38]. Besides, the OBD detectors as well as the fast scanners and signal detectors needed to be improved. Nowadays, the microscope developed by Ando´s group is commercial and it can reach a scan rate up to 12 frames per second (fps). One of the early successful works performed by the group of Ando is shown in Figure 1.4 (e) [39]. It shows a sequence of four images taken at a scan rate of 1 fps of bacteriorhodopsin trimers. They could study the light-induced conformational changes of the trimers by illuminating the sample with green light (λ=532 nm) and showed that the conformational changes were reversible once the light went off, besides that these changes were induced only by green light, thus demonstrating the specific nature of the bacteriorhodopsin trimers.
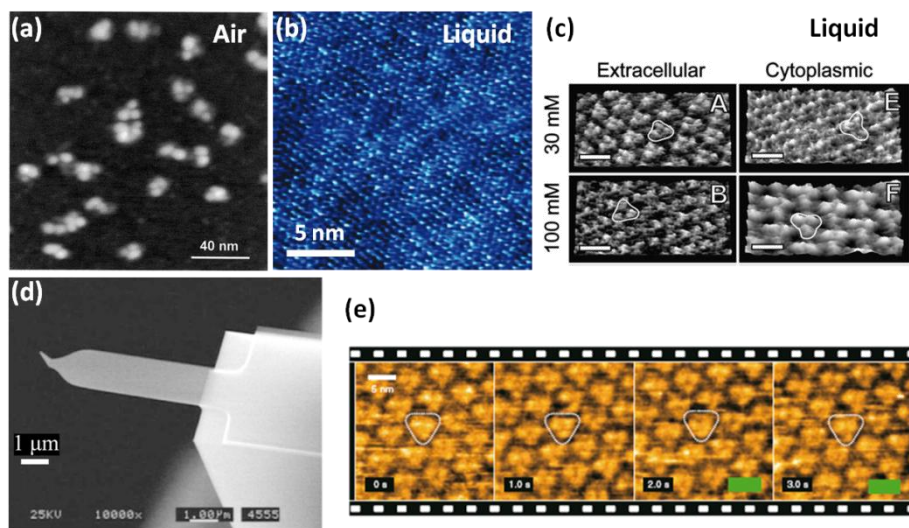
Figure 1.4. Amplitud modulation AFM. (a) Topography image of IgG antibodies on mica measured in air, adapted from [31]. (b) Atomic resolution on muscovite mica in liquid, adapted from [33]. (c) Molecular resolution images of purple membrane, extracellular and cytoplasmic sides, adapted from [34]. (d) Scanning electron microscopy image of a small cantilever developed for high speed imaging, adapted from [38]. (e) Sequence of high speed AFM images showing the structural changes of Bacteriorhodopsin induced by light absorption, adapted from [39].

Frequency modulation AFM

Frequency modulation atomic force microscopy (FM-AFM) uses the same operating principle as other modes in AFM [40]. An observable which is sensitive to tip-sample interactions is kept fixed to follow the topography of the sample. In FM-AFM, the tip is always oscillating at its resonance frequency. In this configuration the phase shift between the driving signal and the response is 90º thanks to a phase-locked-loop (PLL). When the tip approaches the sample, the tip-sample interaction is inducing a decrease in the oscillation amplitude and a shift in the resonance frequency.

A certain shift in the resonance frequency, Δf, is chosen as the feedback parameter for the topography in FM-AFM (see Figure 1.2, Case 2). This value will be negative if the curve moves to the left side implying an attractive interaction, or positive, if the curve moves to the right side, consequently measuring a repulsive interaction. This change in sign depending on the nature of the force (attractive or repulsive) could destabilize the tip oscillation. A method that overcomes this drawback will be presented in next section (see Hybrid AFM).

The tip will scan the sample at the frequency shift, Δf, chosen by the user, but when the tip detects a change in the sample properties or the topography, the frequency shift will change to $\Delta f'$ (Case 3 in Figure 1.2) and the feedback system will move the z scan to compensate for the change in the set-point value (Case 4). By taking into account the oscillation amplitude, there will be two different configurations in FM-AFM. The first one to have been developed was the constant amplitude configuration (CA-FM), in which the cantilever oscillates at a fixed oscillation amplitude [40]. The second one was the constant excitation mode (CE-FM), in which the excitation amplitude is kept constant [41]. During this thesis when referring to FM-AFM is always in the CA-FM configuration. In FM-AFM the time scale is defined as [42]:

$$\tau = \frac{1}{\omega_0} \tag{1.5}$$

and since it is not dependent on the Q factor, it has been mainly applied to measurements in UHV. The first image which showed true atomic resolution in AFM was possible by using FM-AFM in UHV (see figure 1.5 (a)) [43] and employing large amplitudes (~40 nm) and cantilevers with spring constants around 20 N/m. These large amplitudes were used to avoid the instabilities that could cause a sudden jump-to-contact (large adhesion forces) if the cantilever restoring force, kA, is not larger than the interaction force exerted on the tip, F_{ts}.

However, since the optimal amplitudes to obtain atomic resolution must be in the range of Å, the use of cantilevers with higher spring constants was further implemented [44]. In the attempt of using small amplitudes, working in liquids might provide successful operation even with relatively soft cantilevers for FM-AFM (~ 40 N/m) since in liquids attractive forces are small. The main drawback of FM-AFM in liquids is that the frequency noise increases as the Q factor decreases, as happens in liquid environment. Yamada´s group overcame this problem by developing a deflection sensor with a deflection noise sensitivity of 17 fm/$\sqrt{Hz}$ [45] and applied the FM-AFM scheme to liquids obtaining atomic and molecular resolution [46-48]. Nowadays, high resolution images in liquid environment are routinely achieved and impressive images have been obtained, for example the image of the DNA double helix [49] (see figure 1.5 (d)).

Another extended use of FM-AFM is its combination in UHV with STM. Recently, it has provided the possibility to observe *in situ* chemical interactions, as the Bergman cyclization by atomic manipulation (see figure 1.5 (e)) [50].
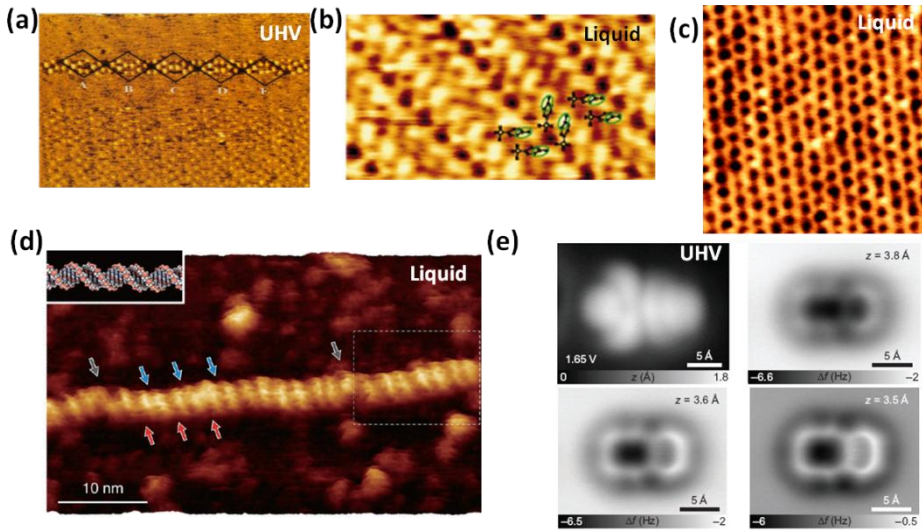
Figure 1.5. Frequency modulation AFM. (a) First atomic resolution image on Si(111) in UHV, adapted from [43]. (b) Molecular resolution image on poly-PTS crystal, adapted from [47]. (c) Atomic resolution on muscovite mica in liquid, adapted from [48]. (d) High resolution FM-AFM topography image of the plasmid DNA in liquid, adapted from [49]. (e) STM image along with FM-AFM images of diyne 4 on NaCl(2ML)/Cu(111) adapted from [50].

Hybrid AFM

In this section Hybrid AFM mode is introduced. This mode will be applied in chapter 2 and 3 for measurements in liquid. This mode was proposed as an alternative to frequency modulation AFM operation in air or liquid [51, 52]. In 2012 this mode was theoretically described and applied to UHV, air and liquid measurements on different samples [53]. This mode consists of using the driving amplitude, the driving force required to maintain a fixed amplitude in CA-FM, as the feedback parameter for topography. The scheme of this mode is shown in Figure 1.6. It has two main feedback loops. The first loop keeps the oscillation amplitude at a fixed value.

During the imaging process, the amplitude of the force that drives the oscillation of the cantilever V_{exc} is also kept at a fixed value which is higher than the one used initially to excite the cantilever $V_{exc,0}$. The second loop tracks the actual resonance frequency of the cantilever so the oscillation is always phase shifted 90º with respect to the driving force. The first feedback loop provides a robust imaging process and enables the acquisition of high resolution images while applying very small forces, whereas the second loop enables the accurate determination of the force. As opposed to the frequency shift, the driving voltage has a monotonic behavior which prevents changes in the slope of the interaction force (attractive or repulsive) that could destabilize the operation of the microscope. This mode has been called Hybrid AFM mode because it can be understood as a hybrid of frequency and amplitude modulation AFM methods. From amplitude modulation AFM [54], it incorporates the condition of keeping the driving force and oscillation amplitude fixed during imaging, while from frequency modulation AFM [40], it incorporates the condition of imaging with the oscillation tuned at the actual resonance frequency.
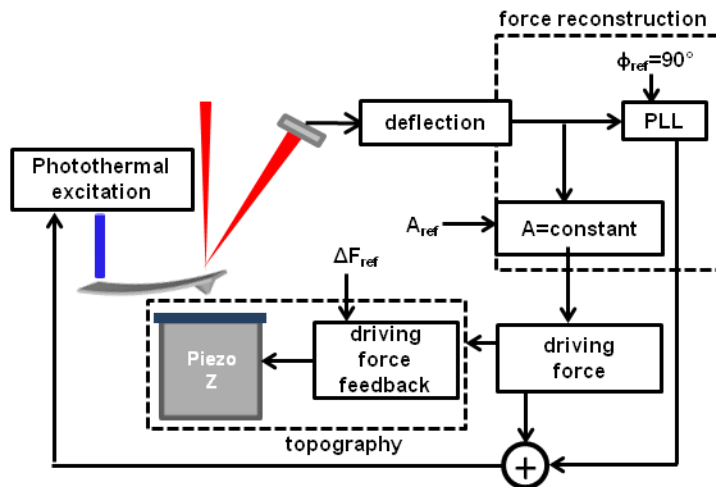

Figure 1.6. Scheme of the hybrid AFM mode. The feedback parameter to track the topography is the driving force, which is adjusted to maintain a constant oscillation amplitude. Besides, the cantilever is always at resonance frequency due to the PLL.

Bimodal Atomic Force Microscopy

Here, a brief introduction of multifrequency AFM is presented. Chapters 4 and 5 of this thesis present multifrequency AFM applications, especially in bimodal operation. Multifrequency force microscopy is based on the excitation of several frequencies of the cantilever [55]. These frequencies may correspond to the harmonics [56-58], which are positive integer multiple of the fundamental resonance frequency, and/or to the eigenmodes of the cantilever, either flexural or torsional [59-63]. When the cantilever interacts with the sample, the response of the excitation frequencies of the cantilever carries the information of the non linear tip-sample interaction force. Figure 1.7 (a) shows the frequency response of a rectangular cantilever under a non linear force. The graph displays the amplitudes of the harmonics and how this response is modulated by the excitation of the second ($6.27\omega_0$) and third ($17.5\omega_0$) eigenmodes of the cantilever. Through the detection of these excitations, multiple observables can be obtained and thus the interactions can be separated from the topography information. The multifrequency AFM approach has opened the path for the study of multiple properties and different materials in liquid, air and UHV [60, 64, 65]. Two examples are given in Figures 1.7 (c) and (d). The detection of torsional harmonics and their subsequent analysis, has been applied to the calculation of mechanical properties of polymers and membrane proteins and to detect and quantify single molecule interactions [66]. In addition, the detection of the frequency response when the cantilever is in contact with the sample has been used to image structures which are embedded in different materials [67].

Regarding the excitation of higher modes, the most used technique is bimodal excitation [59]. In this setup the first and the second eigenmodes are excited. The use of the main dynamic modes, Amplitude modulation (AM-AFM) and frequency modulation (FM-AFM), gives rise to the different schemes available in Bimodal AFM.

Bimodal Scheme	A_1	Φ_1	A_2	Φ_2
AM-AM	Set point	Free	Free	Free
AM-FM	Set point	Free	Fixed	90°
FM-AM	Fixed	90°	Free	Free
FM-FM	Fixed	90°	Fixed	90°

Table 1.1: Setups for bimodal operation.

The first studies published using higher modes relied on the idea of using higher modes to enhance the lateral resolution showing that by using the second mode antibody fragments could be revealed with better lateral resolution [68]. This technique has been explored not only theoretically but also experimentally and has shown its capability to extract high resolution maps of the mechanical properties of polymers and biomolecules in liquid and air environments. Figure 1.7 (e) shows the calculation of the mechanical properties map of an IgM antibody in liquid simultaneously with the acquisition of the topography image [69].
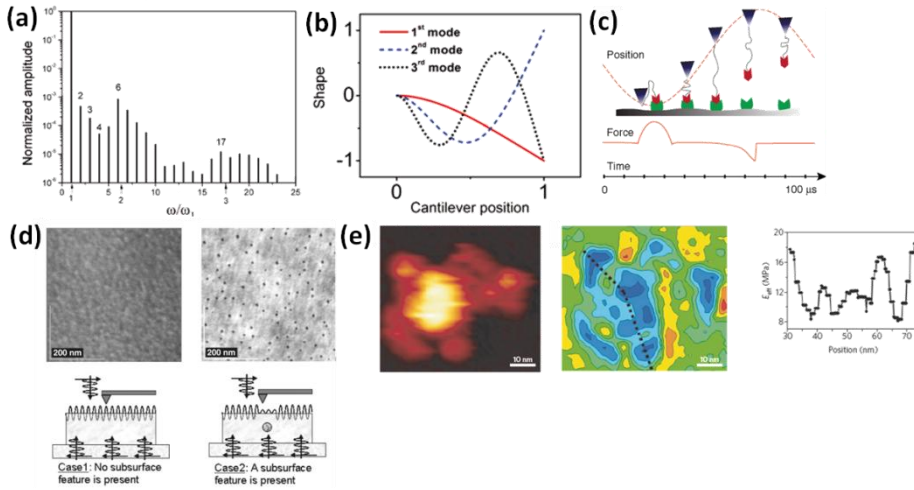
Figure 1.7. Multifrequency AFM. (a) Frequency response of a rectangular cantilever under the influence of a non linear force, adapted from [55]. (b) Modal shaped of the first three flexural eigenmodes for a rectangular cantilever, adapted from [55]. (c) Single molecule force spectroscopy scheme for a torsional harmonics cantilever, adapted from [66]. (d) Topography and phase image of gold nanoparticles buried in a polymer coated substrate. The bottom part shows a schematic description of the method. In the first scheme the wave is not perturbed because no subsurface scattering feature is present. On the contrary, in the second scheme the acoustic wave is perturbed as a result of subsurface scattering, adapted from [67]. (e) Topography and flexibility map of an IgM antibody taken simultaneously by bimodal AFM, adapted from [69].

1.4 Quantitative AFM methods: State of the art

In this section, the main AFM methods developed to obtain quantitative measurements will be reviewed. The methods will be divided in two sections, contact modes or out of resonance and dynamic modes.

Contact modes or non-resonant modes

The first AFM mode developed to obtain quantitative properties of a sample simultaneously with the topographic image was the method called Force volume [70]. This method consists of recording a force curve in contact mode at each pixel in an image. The set-point value of the force curve will be in the cantilever deflection or in the applied force. The nanomechanical properties of the sample surface can be calculated by fitting each curve. Each force curve is made in contact mode and will have from 2^7 to 2^{14} data points, the accuracy of the obtained values will improve with the number of points. To change from one pixel to another, the z-piezo movement is triangular, meaning that a triangular voltage wave is applied to the scanning piezoelectric. The large amount of points and z-piezo movement make the acquisition time very slow. To reduce it, the number of pixels should be reduced, decreasing the resolution of the image.

In order to solve the above problem the Pulsed Force mode was developed [71]. In this mode the cantilever performs the force curve at a certain frequency far from the resonance frequency, in such a manner that the acquisition speed of each pixel is improved. Besides, the z-piezo movement is sinusoidal (a sinusoidal voltage wave is applied to the scanning piezoelectric) in contrast to the triangular voltage wave used in Force volume. Each force curve has a determined distance value, also called oscillation amplitude, and the approach and retract force-distance curve are recorded.

To determine the quantitative properties in real time, it calculates them by using the difference between the set-point force and the minimum force in the curve, the adhesion force, instead of using the full curve fitting. This makes the calculation of the quantitative properties not very accurate.

Pulsed Force mode was enhanced by developing Peak force tapping mode. In Peak force tapping mode, the noise in the deflection channel has been reduced along with the data acquisition and the processing speed so it is possible to fit the curve directly and simultaneously with the acquisition of the topography image as opposed to Pulsed Force mode. Normally, the tip-sample deformation is calculated from the approach curve and the elastic modulus is fitted from the retract curve.

Jumping mode was developed in 1998 [72] and works as Pulsed force mode. In 2012, some enhancements were added to the method to eliminate the dragging effect of the oscillation on the tip-sample interaction [73]. This new method is called Jumping Plus mode.

Dynamic modes

Contact resonance is a technique that was first developed in 1994 by Yamanaka and Arnold groups [74, 75], under the name of Ultrasonic force microscopy (UFM) and Acoustic microscopy, respectively. It is based on contact mode imaging but in order to measure the contact resonance between tip and sample, it applies a small oscillation amplitude by driving either the sample or the cantilever. In this way, it measures the frequency shift of the contact resonance, which is related to the stiffness of the sample contact, along with the changes in the quality factor of the contact resonance, which are related to the sample dissipation. Several AFM techniques based on the idea of contact resonance, described hereafter, were developed by varying the range of frequencies in which the sample or the cantilever are excited and also the way the response is analyzed.

1) In Dual AC resonance tracking (DART) [76] the actuator drives two different frequencies surrounding the resonance frequency and then, the changes in the driving frequencies are analyzed. 2) Another technique based on contact resonance is Band excitation [77]. In this technique a continuous band of frequencies is excited and the full spectral response is studied. All the data generated in this kind of experiments provides enormous information about the sample properties, thus the technique becomes really resourceful to be applied to magnetic, electrical and mechanical imaging. 3) The last technique developed based on contact resonance is FT-nanoDMA [78]. In this technique the sample is excited at multiple harmonic oscillations and then the storage and loss elastic moduli are calculated through the Fourier transform of the deflection detected by the cantilever.

Intermodulation atomic force microscopy [79] is driving two frequencies that bracket the resonance frequency but it is analyzing the spectral response since other frequencies emerge as a consequence of the nonlinear tip-sample forces. These frequencies are called intermodulation products which are defined as linear combinations of integer multiples of the drive frequencies.

In 2007, Sahin and coworkers developed the torsional harmonic cantilever (THC) [80]. By using this kind of cantilever, it is possible to excite and measure the torsional deflection of the cantilever. Then the tip-sample interaction forces are reconstructed with a time-varying force algorithm. They have applied the method to multiple samples, polymers and membrane proteins as well as the detection of antibody-antigen interactions [66, 80-83].

Raman *et al*. [84] used the 0th, 1st and 2nd harmonic signals that are excited when the cantilever interacts with the sample. With those signals they were able to calculate the storage and loss elastic moduli. The method was applied in liquid to live cells by using acoustic and I-drive Lorentz force excitation methods.

As mentioned before, bimodal excitation provides versatile configurations depending on the purpose of our measurements and the information to be probed, qualitative or quantitative.

The first bimodal method developed to quantify the mechanical properties of a sample was FM-AM [69]. The method was applied in liquid to obtain the Elastic modulus map of an IgM antibody. To use this approach a correction factor, C, is necessary and it can be calculated by reconstructing the force curve by using the Sader-Jarvis equation. It has been shown that for stiff materials the use of the correction factor can lead into errors since the indentation values are very low.

Chapter 2

The influence of the force for biomolecules imaging

2.1 Introduction

The development of fields such as nanosciences and nanotechnology has become a reality thanks to instruments that allow the study of the properties at the nanoscale. The instrumentation has to provide accurate and precise measurements. Since its development, AFM has been a fundamental technique to map the topography of surfaces being one of the few instruments capable of sub-angstrom resolution in height. However, the determination of the true height of nanostructures is still under debate [85-88].

The most employed dynamic modes in AFM were already introduced in last chapter. Amplitude modulation (AM-AFM) and frequency modulation (FM-AFM) are widely used in all types of environments, from vacuum to liquids, and are the most established modes in dynamic AFM. As explained in Chapter 1, when the tip is approaching the surface, the dynamics of the cantilever suffers some changes due to the interaction forces. These changes are observed in the oscillation amplitude, the phase shift of the oscillation of the cantilever with respect to the excitation force, the resonance frequency and the deflection of the cantilever.

Dynamic modes use one of these observables as the feedback to track the topography of the sample. AM-AFM uses the changes in the oscillation amplitude and FM-AFM the changes in the resonance frequency.

Initially, AM-AFM was mainly used in liquid and air environment and FM-AFM in vacuum. As mentioned in Chapter 1, this was because of the different time responses for both methods ($\tau = \frac{2Q}{\omega_0}$ for AM-AFM and $\tau = \frac{1}{\omega_0}$ for FM-AFM) and their different dependence on the Q factor. Improvements in the deflection sensor sensitivity [45], enabled the application of FM-AFM in air and even liquids [47, 48]. Thus, a controversy about which one of the modes was better, in terms of high resolution and applied force, started. These studies were basically performed in liquid and air environments considering that both modes are able to work within the same operational parameters (same cantilevers and same free amplitudes) in these environments [89-95]. There are several parameters to consider when a comparison between the dynamic modes in AFM is made. First, it is possible to compare the modes in terms of high resolution, but it has been shown that both modes are able to provide atomic and molecular resolution in liquid [33, 34, 47, 48]. Second, since measuring soft samples gently is one of the main advantages in AFM, the force exerted by the tip on the sample has also been a parameter to compare dynamic AFM modes. When applying high forces, the deformation caused by the tip on the sample increases. As the deformation increases the apparent measured height of the biomolecules is reduced. The lower the height, the larger the applied force on the sample. This effect is the so-called height loss in AFM caused by the interactions between the tip in contact with the sample. This is general for a repulsive force when the contact between two bodies has already taken place but there is also a height loss, height gain or height inversion caused by the different interaction forces measured by the AFM tip between samples and substrates.

Air measurements performed in different samples [86-88, 94], biomolecules or self-assembled monolayers, have shown these effects when measuring samples that could present different regimes between the supporting surface and the biomolecules (support-tip and sample-tip interactions). In some cases, the height loss, height gain or height inversion may be caused by the presence of adsorbed water layers on the tip and the sample or supporting surface [88]. For experiments performed in liquid, height gain and height loss of biological structures measured in buffer solution [96] were shown as well. These artifacts are explained by the Derjaguin-Landau-Verwey-Overbeek (DLVO) theory [97] which combines the electrostatic repulsion between tip and sample along with the Van Der Waals attraction. Consequently, to make a reliable study of the applied force by the dynamic modes based on the apparent height, it is necessary to take into account that the sample-tip and support-tip interactions must have the same interaction nature.

In this chapter, a a study of the operational factors that control the applied force on soft matter samples in the main dynamic AFM operation modes has been made. The study focuses on the apparent height of different biomolecules and biomaterials as a cause of the applied force. The chapter is divided in two parts, as follows: The first part of the chapter shows the different height obtained in air for Immunoglobulin M (IgM) antibodies, G5 Polyamidoamine (PAMAM) dendrimers and DNA plasmid by AM-AFM and FM-AFM. This section also provides a theoretical expression to calculate the peak force in FM-AFM measurements performed in air. In the second part of the chapter, IgM antibodies and DNA plasmids are measured in liquid environment. The dynamic modes compared in this section are AM-AFM and Hybrid AFM at different free amplitudes and set-points. A meaningful difference for low free amplitudes is found and simulations are presented to clarify this effect.

2.2 Experimental methods

In order to perform a reliable comparison, similar working conditions have to be set in both modes. The resonance frequency was set while the cantilever was several microns away from the sample. On the other hand, the free amplitude in AM-AFM was set when the tip was few nanometers away from the sample and this amplitude was chosen to be the same for the amplitude feedback in FM-AFM or Hybrid AFM.

The set-point parameter in each mode, amplitude for AM-AFM, frequency shift for FM-AFM and driving amplitude for Hybrid AFM, was chosen so to achieve the best resolution in the topography AFM image. Measurements in liquid have been performed in distilled water to avoid DLVO forces and at a pH of 5.5.

For air measurements, different kinds of tips have been used. In order to prevent long range attractive forces and capillary forces, sharp tips were used and the measurements were performed under dry nitrogen environment. Under these conditions the dominant forces are short-range repulsive forces so the tip is in permanent contact with the sample in both dynamic modes. The differences in apparent height are considered as a direct measurement of the applied force. For IgM measurements, SSS-SEIHR cantilevers (Nanosensors) were used with typical values of $k \approx 9$ N/m, $f_0 \approx 118$ kHz. For the PAMAM dendrimers, SSS-NCLR cantilevers (Nanosensors) were used, with nominal values of $k \approx 30$ N/m, $f_0 \approx 154$ kHz and for the DNA plasmid sample, PPP-NCH cantilevers (Nanosensors) with typical values of $k \approx 40$ N/m, $f_0 \approx 300$ kHz.

In the experiments performed in liquid, AC-40TS cantilevers (Olympus) with typical values in liquid of $k \approx 0.07$ N/m, $f_0 \approx 25$ kHz were used. The free amplitude values and the set-point parameters for the experiments are depicted in Table 2.1.

	Air			Liquid	
	IgM	PAMAM Dendrimer	DNA Plasmid	IgM	DNA Plasmid
A_0 (**nm**)	23	12	7	3-6	4
A_{sp}	0.85	0.85	0.65	0.8-0.95	0.9
Δf (**Hz**)	10	10	20	-	-
Dissipation (fW)	-	-	-	3-9	30

Table 2.1: Free amplitudes and set-point parameters used in the experiments.

All the AFM images, in which a comparison is made, were taken in the same region of the sample and the height analysis was done for the same proteins or biomolecules. SPIP (Image Metrology) and WSxM (WSxM solutions) were used for the image analysis [98].

Sample preparation

For the experiments performed in this chapter, three different samples were imaged in air and liquid environments. All the experiments in liquid were carried out in distilled water. IgM antibodies and DNA plasmids were deposited on muscovite mica. Mica is a common substrate used in AFM measurements because it is flat, its roughness is ~40 pm, and is easy to reuse by cleaving it with scotch tape [99]. When a mica sheet is cleaved, it remains partially covered by potassium ions which bind together the two adjacent aluminosilicate layers through weak bonds. The cleaving operation leaves the mica negatively charged.

For the measurements on IgM antibodies sample, a 20 μl drop of 150 mM $NiCl_2$ was deposited for 30 seconds on freshly cleaved mica to functionalize the surface. Then, a 5 μl drop of human IgM antibodies (Chemicon, Inc) with a concentration of 40 μg/ml diluted in Phosphate buffered solution (PBS) was injected in the $NiCl_2$ drop. After 60 seconds, the sample was rinsed with distilled water in order to remove weakly attached proteins. For experiments in air the sample was blow-dried with nitrogen gas.

The DNA plasmid sample was prepared by depositing a 2 μl drop of DNA plasmids with a concentration of 0.5 μg/ml diluted in buffer solution of 15mM $MgCl_2$ on freshly cleaved mica. The use of divalent cations Mg^{2+} or Ni^{2+} or the functionalization of the mica surface with 3-aminopropyltriethoxysilane (APTES) are well-known methods to adsorb negatively charged molecules like DNA [100, 101]. In this case the DNA solution was diluted in $MgCl_2$ to avoid the mica functionalization step. After 60 seconds, the sample was rinsed with distilled water in order to remove weakly bound proteins. For experiments in air the sample was blow-dried with nitrogen gas.

G5 Polyamidoamine (PAMAM) dendrimers (Sigma-Aldrich) were deposited on Silicon substrates. Before the deposition step, Silicon substrates were cleaned with 2-propanol, acetone and distilled water (Sigma-Aldrich) by ultrasonic treatment for 5 min each. The substrates were then immersed in a H_2O_2–NH_4OH–H_2O (1:1:2) mixture and four ultrasound cycles of 10 min were performed. After the cleaning procedure, a 20 μl drop of PAMAM dendrimers with a concentration of 10 μg/ml was deposited on the silicon substrate for 20 seconds. The sample was rinsed with distilled water and blow-dried with nitrogen gas.

2.3 Comparative performance of AM and FM methods for biomolecules imaging in air

Several rounds of experiments have been performed to revisit the experimental results given in the literature for the AM-AFM and FM-AFM comparison in air. These studies established that FM-AFM is more sensitive to tip-sample interactions forces since the apparent height obtained in FM-AFM is higher than in AM-AFM [89, 91, 92, 95]. The enhanced sensitivity that FM-AFM presents can be attributed to the electronics or hardware capability to detect frequency variations of fractions of Hertz while the detection of amplitude changes in the picometre range is not possible.

Font *et al.* [91] performed a theoretical calculation of the limiting values and defined the spatial horizon, which is the limiting area where the interaction forces can be detected by the feedback parameter for a specific dynamic mode. They concluded that the spatial horizon in FM-AFM is larger than in AM-AFM, implying that FM-AFM can detect interactions relatively far from the tip while AM-AFM can only detect interactions under the tip.

Figure 2.1 depicts AM-AFM and FM-AFM images obtained on the samples described in the Section 2.2. The corresponding cross-sections are also shown along with the images. All cross-sections, regardless of the sample, exhibit higher height values in FM-AFM than in AM-AFM. This result validates what is stated in the literature, FM-AFM is more sensitive to the interaction forces than AM-AFM since the applied forces are lower in FM-AFM. By using the obtained height values (see Table 2.2), the height reduction in AM-AFM with respect to the height in FM-AFM can be calculated for each sample. For IgM antibodies (Figure 2.1 (a)) the height in AM-AFM is ~17% less than in FM-AFM. For the PAMAM dendrimers (Figure 2.1 (b)) is ~16% and finally 45% for the DNA Plasmid (Figure 2.1 (c)).

Based on the assumption that the applied force is higher if the apparent height is smaller, for the DNA measurement the applied force in AM-AFM with respect to FM-AFM was higher than in the other measurements. The difference in applied force might be caused by several factors, either the sample stiffness or the experimental parameters. However, reported values show that DNA is stiffer than IgM antibodies [69, 102, 103], therefore the difference in applied force between AM-AFM and FM-AFM is not correlated to the stiffness. If we look at the experimental parameters (Table 2.1) it is difficult to extract or predict a qualitative trend for the applied force in the images.

For instance, based on the set point parameter in both AM-AFM (0.65 for the DNA vs 0.85 for the other samples) and FM-AFM (20 Hz for the DNA vs 10 Hz for the other samples), the applied force was higher on the DNA measurement than in the others. Therefore, the set point parameter would not explain the unlike height reduction. By looking at the experimental parameters it is impossible to have a relevant conclusion about why, in the DNA experiment, the height in AM-AFM was almost 50% less than in FM-AFM. There is a need for a theoretical expression which can provide a manner to quantify the applied force in AM-AFM and FM-AFM.
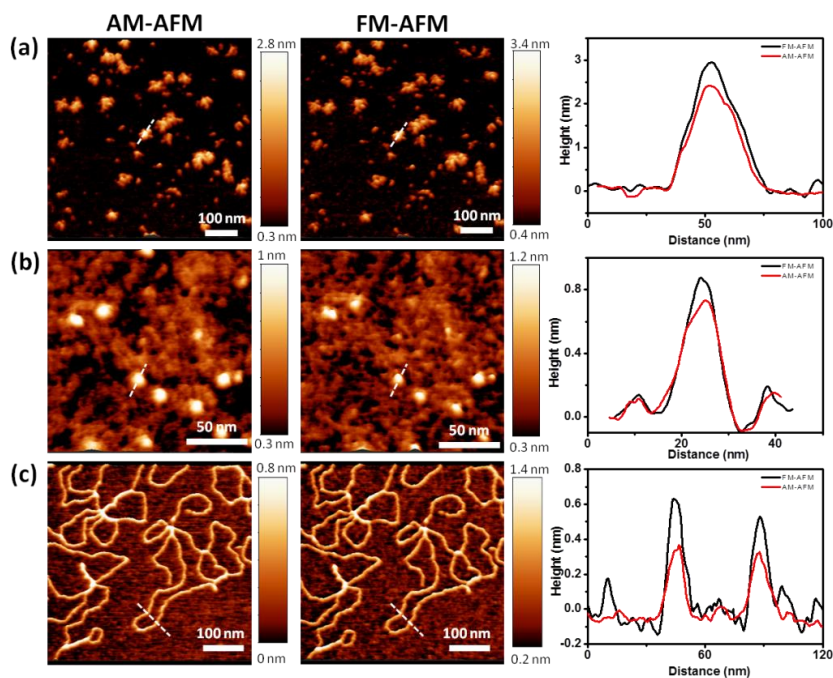

Figure 2.1. AFM images of the samples employed to compare AM-AFM and FM-AFM in air. (a) AFM images of IgM antibodies deposited on a mica surface measured in both dynamic modes and cross-section along the dashed lines. (b) AFM images of PAMAM dendrimers deposited on Silicon substrate measured in both dynamic modes and cross-section along the dashed lines. (c) AFM images of DNA plasmids deposited on a mica surface measured in both dynamic modes and cross-section along the dashed lines.

2.3.1 Theoretical approximations for the peak force in AM-AFM and FM-AFM

The quantification of the applied force in an AFM image taken in a dynamic mode opens the possibility to understand which is the role of the operational parameters and also is a key step to minimize the applied force when measuring soft matter. S. Hu and A. Raman obtained analytical equations for the applied peak force in AM-AFM [104]. These equations were extracted by using different attractive and repulsive interaction forces. The expressions are valid in air and vacuum conditions.

Throughout this chapter, Equation 2.1 for the repulsive regime is used:

$$F_{peak}(AM) = \frac{2^{1/8}\pi^{3/4}}{3^{1/4}} A_0^{9/8} \left(\frac{E_{eff}\sqrt{R}k_c^3}{Q^3} \right)^{1/4} \left(A_{sp} - A_{sp}^3\right)^{3/8} \qquad (2.1)$$

where A_0 is the free amplitude, E_{eff} is the reduced Young modulus, R is the tip radius, k_c is the spring constant of the cantilever, Q is the quality factor and A_{sp} is the ratio between the working amplitude, A', and the free amplitude, A_0, $A_{sp} = A'/A_0$.

The calculation of the maximum indentation is also possible,

$$\delta_{\max}(AM) = \frac{(3\pi)^{1/2} A_0^{3/4}}{2^{5/4}} \left(A_{sp} - A_{sp}^3\right)^{1/4} \left(\frac{k_c}{Q\sqrt{R}E_{eff}} \right)^{1/2} \qquad (2.2)$$

An analytical expression for the peak force in FM-AFM is not known so far. For the derivation of a theoretical expression to quantify the applied force in FM-AFM, the expression which relates the frequency shift with the fractional integral of the force has been used [105]:

$$\Delta f(d) = \frac{f_0}{k_c \sqrt{2\pi A_0^3}} \, I_-^{1/2} F(d) \tag{2.3}$$

where f_0 is the resonance frequency, k_c is the spring constant of the cantilever, A_0 is the free amplitude and $I_-^{1/2} F(d)$ is the half integral of the interaction force, F. The half integral is calculated by using the Riemann-Liouville fractional calculus [106]:

$$I_-^{1/2} F(z) = \frac{1}{\Gamma(1/2)} \int_z^\infty \frac{F(z)}{(t-z)^{1/2}} \, dt \tag{2.4}$$

In order to calculate equation 2.3, the Hertz model is assumed. The Hertz model is used to describe the force between two bodies in contact, so it can be applied in AFM measurements in the repulsive regime. The Hertz model will be presented more extensively in next chapter:

$$F_{Hertz} = \frac{4}{3} E_{eff} \sqrt{R} \, \delta^{3/2} \tag{2.5}$$

where R is the tip radius, δ is the indentation and E_{eff} is the reduced Young modulus.

By applying the Hertz model to equation 2.3 we obtain:

$$\Delta f(d) = \sqrt{\frac{R}{8A_0^3}} \frac{f_0}{k_c} E_{eff} \delta^2 \tag{2.6}$$

The combination of equation 2.5 with 2.6 allows the calculation of F_{peak} and δ for FM-AFM in the repulsive regime:

$$F_{peak}(FM) = \frac{2^{1/8}8}{3} A_0^{9/8} \left(E_{eff}\sqrt{R}\right)^{1/4} \left(\frac{\Delta f k_c}{f_0}\right)^{3/4} \qquad (2.7)$$

$$\delta_{max}(FM) = \frac{2^{3/4} A_0^{3/4}}{R^{1/4}} \left(\frac{\Delta f k_c}{f_0 E_{eff}}\right)^{1/2} \qquad (2.8)$$

where A_0 is the free amplitude, E_{eff} is the reduced Young modulus, R is the tip radius, Δf is the frequency shift, k_c is the spring constant of the cantilever and f_0 is the resonance frequency.

Some similarities are found between equation 2.1 and 2.7 as well as for equation 2.2 and 2.8. These similarities are studied in next section.

2.3.2 Results

In order to study the relationship between the peak forces in AM-AFM and FM-AFM through equations 2.1 and 2.7, the ratio between both forces has been calculated,

$$\frac{F_{peak}(AM)}{F_{peak}(FM)} = \frac{(3\pi)^{3/4}}{8} \left(\frac{f_0}{\Delta f}\right)^{3/4} \frac{\left(A_{sp} - A_{sp}^3\right)^{3/8}}{Q^{3/4}} \qquad (2.9)$$

The first thing to be noticed is that the ratio between these forces does not depend on the Young modulus, E_{eff}, neither the spring constant, k_c, nor the tip radius, R. The ratio depends on the operational set-point parameter related to each mode, A_{sp} in AM-AFM and Δf in FM-AFM, and the cantilever resonance frequency, f_0, and quality factor, Q.

Equation 2.9 can now be applied to understand the values extracted from the cross-sections in Figure 2.1. Table 2.2 shows the nominal height of the biomolecules and the height extracted in AM-AFM and FM-AFM in Figure 2.1 along with the values obtained for Equation 2.9.

	Air		
	IgM	PAMAM Dendrimer	DNA Plasmid
Nominal Height (nm)	7	5	2
Height-AM (nm)	2.42	0.73	0.34
Height-FM (nm)	2.94	0.83	0.62
Force ratio (Eq. 2.9)	5	6	9

Table 2.2. Nominal height and apparent height in AM-AFM and FM-AFM and the peak force ratio (Equation 2.9) in AM-AFM and FM-AFM for the samples showed in Figure 2.1.

The values provided by Equation 2.9 explain the difference in apparent height obtained. The ratio between the applied forces in the experiment where DNA plasmid was used is higher than in the others, contributing to a large difference in apparent height between AM-AFM and FM-AFM.
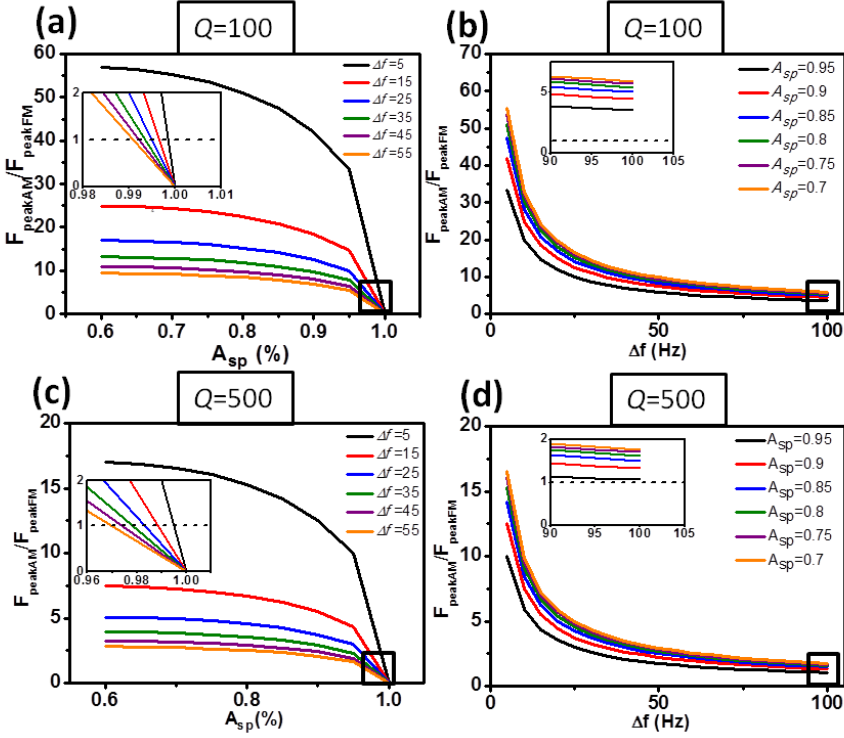
Figure 2.2. Plots of the applied force ratio between AM-AFM and FM-AFM *versus* the set-point in AM-AFM and FM-AFM. (a) Force ratio for constant Δf as a function of A_{sp}, for $Q = 100$. (b) Force ratio for constant A_{sp} as a function of Δf, for $Q = 100$. (c) Force ratio for constant Δf as a function of A_{sp}, for $Q = 500$. (d) Force ratio for constant A_{sp} as a function of $\Delta f A_{sp}$, for $Q = 100$. $f_0 = 300$ kHz. The insets show the zoom in for the region where the peak force in AM-AFM equals the peak force in FM-AFM. The dashed line indicates the points for which the peak force is the same in both dynamic modes.

Equation 2.9 can be studied as a function of the operational parameters. Figure 2.2 depicts the dependence of the applied force ratio, as calculated with equation 2.9, with set-point parameters, A_{sp} and Δf, for a cantilever of $f_0 = 300$ kHz and for two different Q, 100 and 500. Figure 2.2 allows the comparison of the applied force in AM-AFM for a constant set-point amplitude, A_{sp}, with the applied force in FM-AFM for a constant set-point frequency shift, Δf.

First of all, we observe that an increment in Q for the same resonance frequency produces a reduction in the applied force ratio. For example, in Figure 2.2 (a) the orange line for $\Delta f = 55Hz$ and $Q = 100$ shows that the applied force in AM-AFM is almost ten times higher than in FM-AFM, but in Figure 2.2 (c) this ratio is reduced by a factor of three for $Q = 500$.

Figures 2.2 (a) and (c), show the effect of decreasing the set-point amplitude at a constant Δf in the F_{peak} ratio. There is a sharp increment in the applied force for set-point amplitude values between 0.95-0.99. After this sharp increment, the ratio increases steadily until reaching a constant value. Regarding the Δf value, the force ratio decreases when the Δf increases, indicating that to apply the same force in AM-AFM than in FM-AFM, the applied force in FM-AFM has to increase considerably. The insets show the regions where the peak force in AM-AFM equals the peak force in FM-AFM. For the small Q, the set point amplitudes should be in the 0.99-1 range, which is clearly an unaccessible regime in AM-AFM experiments. However, for $Q= 500$, the range diminishes to 0.97-1.

Figures 2.2 (b) and (d), show the opposite experiment of increasing the set point in FM-AFM, Δf, for a constant A_{sp} in AM-AFM. The tendency is the same as in Figures 2.1 (a) and (c). The applied force in AM-AFM is higher than in FM-AFM and the difference becomes smaller when the set point in FM-AFM is dramatically increased. For $Q= 100$ and the operational parameters simulated, both modes would never exert the same force. On the contrary, for $Q= 500$, the peak force ratio decreases and, in agreement with Figure 2.2 (c), there is a compatible range for set-point amplitudes larger than 0.96 in which both modes would apply the same force.

Additionally, we have combined equations 2.2 and 2.8 to compare δ_{max}AM with δ_{max}FM,

$$\frac{\delta_{max}(AM)}{\delta_{max}(FM)} = \frac{(3\pi)^{1/2}}{4}\left(\frac{f_0}{\Delta f}\right)^{1/2}\frac{\left(A_{sp} - A_{sp}^3\right)^{1/4}}{Q^{1/2}} \tag{2.10}$$

Figure 2.3 shows the ratio between the maximum indentation in AM-AFM and the maximum indentation in FM-AFM for a cantilever of $f_0 = 120$ kHz and $Q = 450$. By following the same idea as in Figure 2.2, Figure 2.3 shows the indentation ratio between AM-AFM and FM-AFM, for a constant Δf, while decreasing A_{sp} (Figure 2.3 (a)), and for constant A_{sp}, when increasing Δf, (Figure 2.3 (b)). The line that crosses both graphs indicates the values for which both modes produce the same indentation value, thus the same applied force.
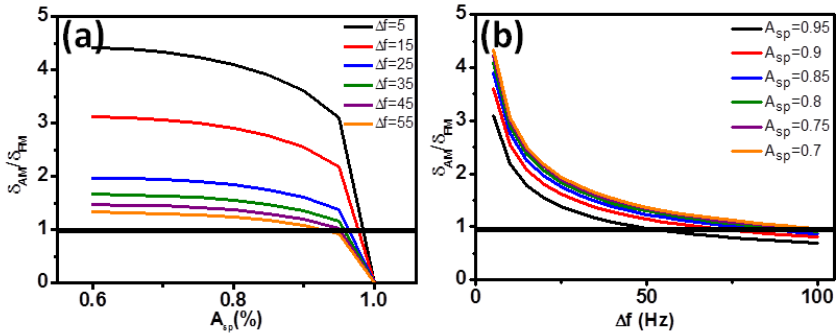

Figure 2.3. Plots of the indentation ratio between AM-AFM and FM-AFM *versus* the set-point parameter. (a) Indentation ratio for constant Δf as a function of A_{sp}. (b) Indentation ratio for constant A_{sp} as a function of Δf. $f_0 = 120$ kHz and $Q = 450$. The black line indicates the points for which the indentation is the same in both dynamic modes.

To check the validity of Equations 2.9 and 2.10, the conditions in Figure 2.3 were reproduced experimentally. Measurements on IgM antibodies were taken for different set-point values in AM-AFM and FM-AFM with SSS-SEIHR cantilevers. Since AM-AFM images in the repulsive regime at A_{sp} values higher than 0.95 in air are difficult to obtain, the experiment tried to fit the values of Figure 2.3 (b). The experiment was carried out as follows: first, an image in AM-AFM was taken with operational parameters of $A_0 = 23$ nm and $A_{sp} = 0.85$, and then FM-AFM images at $\varDelta f = 10$, 30, 50, 70 and 90 Hz were taken. According to the theoretical predictions in Figure 2.3 (b), the heights obtained at $A_{sp} = 0.85$ (blue line) and $\varDelta f = 80$ Hz should be the same.

To calculate the average height value, the height of the same twenty-two antibodies was analyzed. Table 2.3 summarizes the average height values obtained in this experiment.

	AM-AFM	FM-AFM				
Set-Point	0.85	10 Hz	30 Hz	50 Hz	70 Hz	90 Hz
Height (nm)	2.01	2.23	2.15	2.13	2.03	2.01

Table 2.3. Average height values of IgM antibodies imaged at different set-point values and dynamic modes.

By taking into account the values displayed in Table 2.3, we can conclude that in order to obtain the same applied force in AM-AFM as in FM-AFM, the set-point in FM-AFM must be higher than 70 Hz. This conclusion is in good agreement with the values extracted from Figure 2.3 (b) and, therefore, validates the application of equations 2.9 and 2.10.

2.4 Comparative performance of AM and Hybrid methods for biomolecules imaging in liquid

Here, a similar comparison of dynamic modes as in the previous section is performed however, in this section the experiments are performed in liquid. The comparison in this section is again carried out by considering the effect of the applied force. Hybrid AFM mode is now used instead of FM-AFM. As explained in Chapter 1, the difference between Hybrid AFM and FM-AFM is that Hybrid AFM mode uses the driving amplitude as the feedback in topography instead of the frequency shift, but both modes have the same loops. Equations 2.9 and 2.10 are no longer valid because they cannot be applied in liquid environment [104].
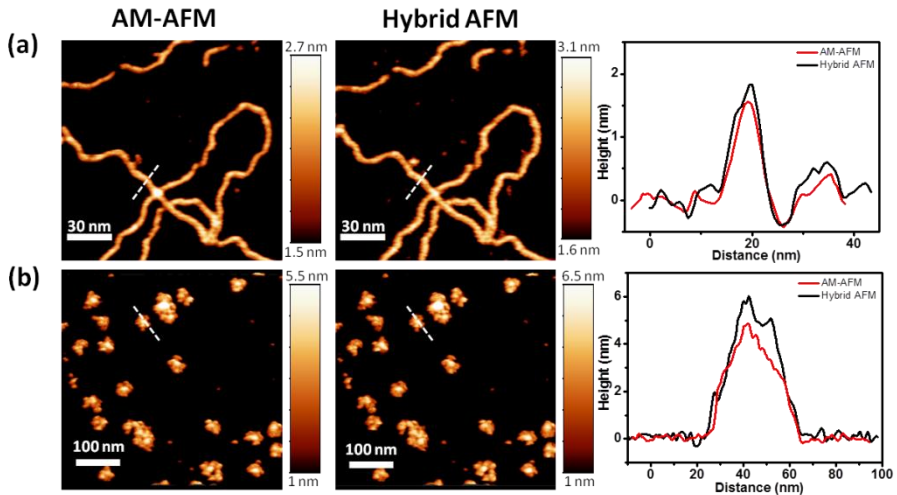
Figure 2.4. AFM images of the samples used to compare AM-AFM and Hybrid AFM in liquid. (a) AFM images of DNA plasmids deposited on a mica surface measured in both dynamic modes and cross-sections along the dashed lines. (b) AFM images of IgM antibodies deposited on a mica surface measured in both dynamic modes and cross-sections along the dashed lines.

Figure 2.4 shows AFM topography images of IgM antibodies and DNA plasmid taken in AM-AFM and Hybrid AFM. The cross-sections along the dashed lines are also shown. To record the IgM image, 3 nm of free amplitude was used and for the DNA, 4 nm (Table 2.1). Similar high resolution images are obtained for both dynamic modes but the cross-sections show a higher height value in Hybrid AFM than in AM-AFM for both, IgM antibodies and DNA. In order to quantify the difference in height, we have calculated the height reduction in AM-AFM with respect to the height obtained in Hybrid mode. Ten antibodies were chosen from the recorded images and the SPIP software was used to measure the average height value. In the case of the DNA sample, three regions displaying DNA plasmids were chosen from the images and the SPIP software was used for the analysis. The calculated height values are displayed in Table 2.4.

	Liquid	
	IgM	DNA Plasmid
Nominal Height (nm)	7	2
Height-AM (nm)	4.87	1.56
Height-Hybrid (nm)	5.92	1.82

Table 2.4. Nominal height and apparent height in AM-AFM and Hybrid AFM modes calculated from Figure 2.4 in both samples.

The results in table 2.4 show that there is a difference in the applied force between both modes, AM-AFM and Hybrid AFM, in liquid. For the same kind of tips and similar operational parameters, the height reduction is approximately 17% for the IgM and 14% for the DNA. As described in previous section, the difference in applied force depends on the operational parameters.

In order to study the dependence of the applied force with the operational parameters, we carried out measurements at two different A_0. To verify that the tip was not deforming the antibody irreversibly (plastic deformation), a sequence of images was taken in the same region of the sample. For each mode, 4 images were taken at $A_0 = 3$ nm and $A_0 = 6$ nm, as follows: first, AM-AFM was used to take the image at $A_0 = 6$ nm, then Hybrid AFM mode was used at the same amplitude and, finally, two more images, one in AM-AFM and the other one in Hybrid mode were performed at the former free amplitude. With this approach, it is possible to check if the produced deformation was irreversible. The sequence at $A_0 = 3$ nm was done following the same approach as for $A_0 = 6$ nm.

Figure 2.5 depicts the cross-sections along one of the imaged IgM antibodies. The cross-sections show that the height is recovered in the second scan of each mode, indicating that the applied force was not high enough to produce plastic deformations. Figure 2.5 (a) shows that the height in Hybrid AFM is always displaying higher values than in AM-AFM. Table 2.5 gives the average height values in AM-AFM and Hybrid AFM calculated using the cross-section profiles of the same ten antibodies. On the contrary, Figure 2.5 (b) shows similar height values for both modes. The height reduction in this case is 2 %. The values show that when increasing the free amplitude, A_0, there is no difference in applied force between AM-AFM and Hybrid AFM in liquid.

	Liquid	
	IgM $A_0 = 3$ nm	IgM $A_0 = 6$ nm
Nominal Height (nm)	7	7
Height-AM (nm)	4.85	4.73
Height-Hybrid (nm)	5.5	4.83

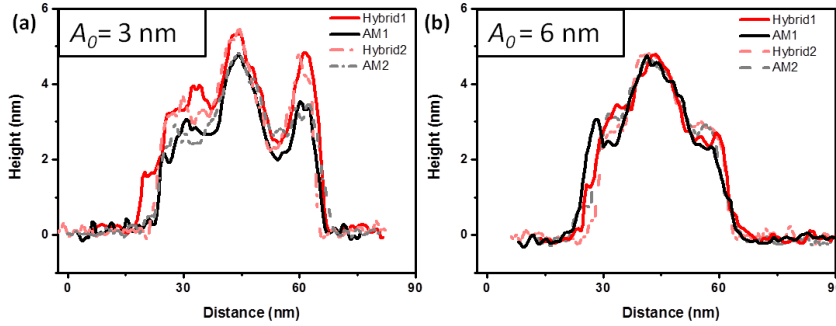**Table 2.5.** Nominal height and apparent height in AM-AFM and Hybrid AFM modes.

Figure 2.5. Cross-sections along one of the IgM antibodies measured in liquid. (a) Cross-sections of the same IgM antibody measured in the sequence of images taken by AM-AFM and Hybrid AFM at $A_0 = 3$ nm. (b) Cross-sections of the same IgM antibody measured in the sequence of images taken by AM-AFM and Hybrid AFM at $A_0 = 6$ nm.

To validate the experimental results, we have performed simulations in AM-AFM and FM-AFM with the same experimental parameters. Simulations were used to quantify the applied force, at the image set-point. The model used for the interaction force was the Hertz model (Equation 2.5) and the set parameters were $A_0 = 3$ nm and $A_0 = 6$ nm, $f_0 = 25$ kHz, $Q = 2$, $E_s = 5$ MPa, $E_t = 170$ GPa, $R = 8$ nm and $k = 0.07$ N/m.

For the FM-AFM simulations, the frequency shift was calculated with Equation 2.3 and then, the force was computed with Sader-Jarvis force reconstruction algorithm [107]:

$$F_{ts}(d) = 2k\int_d^\infty X_{sj}dx + 2k\int_d^\infty \frac{\sqrt{A}}{8\sqrt{\pi(x-d)}} X_{sj}dx - 2k\int_d^\infty \left(\frac{A^{3/2}}{\sqrt{2(x-d)}} \frac{\partial X_{sj}}{\partial d} \right)dx \quad (2.11)$$

$$X_{sj} = \frac{\Delta f(d)}{f_0} \quad (2.12)$$

where k is the spring constant of the cantilever, F_{ts} is the interaction force between tip and sample, f_0 is the unperturbed resonant frequency, Δf is the change in the resonant frequency, A is the amplitude of oscillation and d is the distance of closest approach between tip and sample in an oscillation.

The frequency shift obtained by the approximation (Equation 2.3) is in good agreement with the frequency shift obtained by simulating a PID controller and a PLL.

The AM-AFM simulations were done with the dForce simulator with acoustic excitation [108]. Figure 2.6 (a) depicts the oscillation amplitude, A, for the two different free amplitudes as a function of the minimum tip-sample distance. The dots mark the set-point amplitude at which the images were taken, $A_0 = 3$ nm, $A_{sp} = 0.8$ and for $A_0 = 6$ nm, $A_{sp} = 0.95$. The values are characterized by a tip-sample distance which is related to the applied force given by Figure 2.6 (c). Figure 2.6 (b) shows the frequency shift for the two different free amplitudes as a function of the minimum tip-sample distance. The set-point frequency shift was extracted from the frequency channel in the images, for the image at $A_0 = 3$ nm, $\Delta f = 900$ Hz and for $A_0 = 6$ nm, $\Delta f = 950$ Hz. For these frequency shift values, there is a tip-sample distance, and for this tip-sample distance the applied force is extracted (see Figure 2.6 (c)).
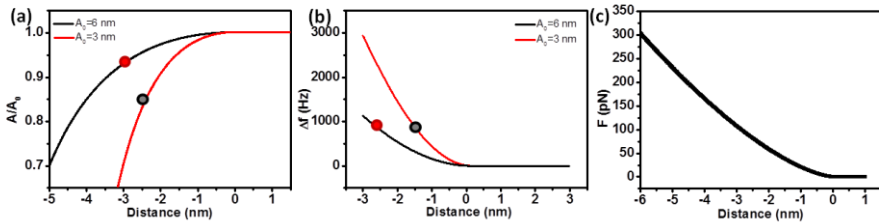

Figure 2.6. Simulations of force curves in AM-AFM and Hybrid AFM. (a) Amplitude curve for $A_0 = 3$ nm and $A_0 = 6$ nm. The dots mark the experimental set-point amplitude. (b) Frequency shift curve for $A_0 = 3$ nm and $A_0 = 6$ nm. The dots mark the experimental set-point frequency shift. (c) Force *versus* distance curve for the interaction force modeled with Hertz model.

The values extracted from the simulations are represented in Table 2.6. In the case in which the free amplitude is 3 nm, the applied forces are 38 pN, in Hybrid AFM, and 81 pN, in AM-AFM.

For the free amplitude set to 6 nm, the applied forces are 86 pN, in Hybrid AFM, and 97 pN, in AM-AFM. This difference in applied force could explain the observed height reduction. Besides, from the simulated indentation, we are able to quantify the height reduction for an initial height of the IgM antibody of 7 nm [103, 109]. The estimated height reduction in AM-AFM with respect to the height in Hybrid mode is 18% at $A_0 = 3$ nm, and 4% at $A_0 = 6$ nm, very close to the experimental values represented in Table 2.5.

A_0 (nm)	Dynamic mode	δ (nm)	Applied Force (pN)
3	AM-AFM	2.5	81
	Hybrid AFM	1.5	38
6	AM-AFM	2.8	97
	Hybrid AFM	2.6	86

Table 2.6. Indentation and applied force values extracted from the simulations.

2.5 Conclusions

In this chapter a comparison of the main dynamic modes operation in air and liquid environments is reported. The comparison is focused on the force that each dynamic mode applies on the surface sample. High resolution imaging of different soft samples by AM-AFM and FM-AFM in air provides the experimental evidence that AM-AFM applies higher forces in the repulsive regime than FM-AFM. Theoretical expressions, valid in air, were deduced to quantify the applied force in the AFM images with the operational parameters. The validity of these expressions was experimentally studied by considering the apparent height of several biomolecules.

The study in liquid environment shows a dependence on the applied force with the free amplitude A_0. The values show that the applied force is higher in AM-AFM than in Hybrid AFM for small free amplitudes (~3 nm) and low set-points (~0.8), but for high free amplitudes (~6 nm) and high set-points (~0.95), the applied force in both modes is almost equal. The conclusion is validated by theoretical simulations.

The difference in applied force found between the dynamic modes could have implications on measurements in which the true height characterization of nanostructures, such as nanoparticles, biomolecules or proteins, is a key factor.

Chapter 3

Stress-strain curve of a single antibody: forces and deformations on a single protein in liquid

3.1 Introduction

Proteins suffer continuous conformational changes due to thermal energy (k_bT 4.1pN·nm or 0.592 kcal/mol) and fluctuate within the different conformational energy landscapes allowed [110, 111]. Therefore, they have to deform repeatedly and adopt different conformations which are evidences of the proteins flexibility.

Mechanical properties at the nanoscale have a significant role in different molecular and cell biology processes [112]. Understanding the mechanical functionalities of complex biological systems requires the measurement of the mechanical compliance of their smallest components. For instance, tumor progression is favored by a remodellation of the mechanical stiffness of the extra-cellular matrix [113]. Improved extensibility such as the one found in fibrin proteins is achieved via the formation of repeated units of hydrogen bonds in alpha helical folds [114]. It has been reported that the misfolding mechanisms of amyloid proteins involves fibrils of different stiffness [115].

Some proteins polymerize into spirals to accumulate elastic energy and that energy is the driving force for lipid membrane deformation [116]. Immunoglobulin M (IgM) antibodies experience multiple unspecific collisions with other proteins, cells or extra-cellular matrix components without any loss of biological activity [117]. This implies that the antibody´s deformation is either negligible or that the antibody fully recovers its size and shape after a collision.

To describe the mechanical properties of a specific material, mechanical engineering concepts are used. The flexibility of a material is defined as the elasticity. The elasticity is measured by applying a force, *F*, measured in Newton, N, or a stress, defined by

$$\sigma = F/Area \tag{3.1}$$

measured in Pascal, N/m^2. This force will produce a deformation on the sample, *δ*, measured in meters, or a strain defined by

$$\varepsilon = \delta/Length \tag{3.2}$$

These parameters have a linear dependence and are related by, E, the Young modulus of elasticity [118]. When plotting the stress versus the strain the different regimes of the material, elastic and plastic, are represented. The elastic regime is characterized by a linear dependence between the stress and the strain. When a force is applied a linear deformation is observed, but once the force stops, the material recovers its initial height. However, when the material reaches the plastic regime, once the force is removed, the material does not recover its initial height and the yield point of the material is reached.

Measuring the mechanical response of a single protein near physiological conditions is challenging for at least two reasons.

(i) The small value of the forces involved in generating elastic deformations and (ii) the need to combine force measurements with high resolution images of single proteins. In this chapter a force microscopy method is presented with the aim of quantifying the softness of a single antibody pentamer by measuring its stress-strain curve with force and deformation resolutions, respectively, of 5 pN and 50 pm. The determination of the stress-strain curve of a single antibody will provide the mechanical properties that explain how these proteins are transported around the body to spot a specific target without any loss of biological functionality.

3.1.1 Nanomechanical properties of proteins in dynamic AFM: forces and deformations

There are several methods that can be employed for obtaining an estimation of protein flexibility. Among these methods, for instance, it has been shown that neutron scattering experiments can detect the average fluctuations of the atoms in a polypeptide chain which do provide an estimation of the protein softness [119]. Also, optical methods in combination with gold nanoparticles have been applied to measure the viscoelastic response of some enzymes [120]. However, these methods provide the average value of the mechanical response of an ensemble of millions of proteins, they are not suitable for proteins larger than 35 kDa or the proteins need to be crystallized preventing the study of their flexibility in their native environment. All these limitations can be overcome by using AFM in liquid.

AFM dynamic and contact methods have been developed to measure the flexibility of packed arrays of proteins [82, 121-124], and in some cases, of single proteins [69, 125-128]. However, force microscopy methods based on the acquisition of force curves have a major limitation when it comes to measuring the stress-strain curve of a single protein: there is only one observable, the cantilever deflection.

Therefore, forces and deformations are mixed in the observables which means that the cantilever deflection is an input in both the determination of the force and the deformation. Thus the error associated with the measurement of the deflection propagates in both the force and the deformation.

Contact mechanics models

In order to relate the observables obtained in AFM to the stiffness of the sample contact mechanics models are used. Next, the models that are going to be used throughout the chapter are introduced.

The model derived by Hertz in 1882 [129] attempted to describe the contact mechanics between two elastic spheres in contact. The Hertz model describes the interaction between a sphere and a semi-infinite plane and is defined by the following equation:

$$F_{Hertz} = \frac{4}{3} E_{eff} \sqrt{R} \, \delta^{3/2} \tag{3.3}$$

where F is the applied force, R is the tip radius, δ is the indentation and E_{eff} is the reduced Young modulus of the interface defined as,

$$E_{eff} = \left(\frac{1 - v_s^2}{E_s} + \frac{1 - v_t^2}{E_t} \right)^{-1} \tag{3.4}$$

where v is the Poisson coefficient, and the subscripts t and s express tip and sample, respectively.

The application of the Hertz model to quantify elastic properties has two main assumptions:

- The contact between the two spheres is purely elastic.

- The sample is considered as an elastic half-space with infinite thickness.

These assumptions can lead to significant errors in the calculation of the elastic properties.

In 2002, Dimitriadis and co-workers [130] developed an equation to solve the problem of finite thickness samples, and this model is called the Bottom Effect Hertz Correction (BEHC). Before this work, there had been some theoretical models [131, 132] which attempted to find a correction of the Hertz model for finite thickness samples, but these solutions required large numerical calculations thus, becoming inconvenient for their use in force spectroscopy. Dimitriadis and co-workers developed two corrections, the first, for samples which are not bonded to the substrate and the second for substrate bonded samples. The fact that a given sample is bonded to the substrate means that the sample is well attached to the surface sample and not only deposited on it.

The rigidity of a sample bonded to the substrate is larger than the one for a not bonded sample since it can change the location. For the case in which the sample is not bonded they apply the Method of images. For substrate samples bonded, they derive the Green´s function.

The obtained expression is valid for both cases, sample bonded to the substrate or not:

$$F_{BEHC} = \frac{4E}{3(1-v^2)} R^{1/2} \delta^{3/2} \left[1 - \frac{2\alpha_0}{\pi} \chi + \frac{4\alpha_0^2}{\pi^2} \chi^2 - \frac{8}{\pi^3} \left(\alpha_0^3 + \frac{4\pi^2}{15} \beta_0 \right) \chi^3 + \frac{16\alpha_0}{\pi^4} \left(\alpha_0^3 + \frac{3\pi^2}{5} \beta_0 \right) \chi^4 \right]$$

(3.5)

where $\chi = \sqrt{R\delta}/h$ and α_0 and β_0 are constants which depend on the material poisson´s ratio, v, and whether the sample is bond or not to the substrate.

In this chapter, for the calculation of the stiffness, the case for a sample bonded to the substrate will be applied:

$$\alpha_0 = -\frac{1.2876 - 1.4678v + 1.3442v^2}{1-v}$$

(3.6)

$$\beta_0 = \frac{0.6387 - 1.0277v + 1.5164v^2}{1-v}$$

(3.7)

3.1.2 IgM antibody

Innate immunity has been refined throughout evolution. The fact that we remain healthy or that we can fight illnesses guarantees that the immunity agents (antibodies, T cells, …) are well designed and working at their full capacity. Antibodies are the key element of the immune system. In particular, IgM antibodies are the first barrier in the humoral immune response. By answering questions about how they act and which factors preclude the stability of this heavy antibody (~950 kDa), almost five times bigger than other types of antibodies, it is possible to explain the response of these antibodies against bacteria or viruses, which opens the possibility to use them in cancer therapy and diagnosis [133, 134].

Several AFM studies have focused on antibodies [31, 60, 69, 135, 136] providing more insights and a better understanding of their structure and their conformational flexibility.

IgM antibodies present a non planar, mushroom-shaped structure with a central protrusion of about 15 nm in diameter from which several arms are projecting out radially (see Figure 3.1). The antibody is made of five IgM monomers, which are formed of a pair of antigen binding fragments (F_{ab}) and an F_c region. Five IgM monomers join the last domain of the F_c region giving rise to a pentameric structure. Two of these monomers are also bonded to the joining chain (J chain), see Figure 3.1.

IgM antibodies have a distinctive morphology, they present a well-defined pentameric structure which makes the identification of the proteins in the AFM images straightforward and the actual response of the antibodies in the same conformation can be explored.
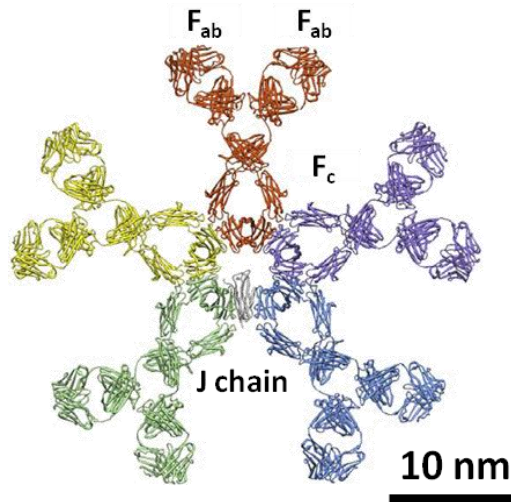
Figure 3.1. Molecular structure of the IgM antibody extracted from the Protein Data Base (code: 2RCJ), adapted from [28]. The IgM antibody is formed of five IgM monomers. Each monomer is Y-shaped and is composed of two antigen binding fragments (F_{ab}) and one crystallizable fragment (F_c). Two of the IgM monomers in the pentameric structure are bounded by a J chain.

3.2 Experimental methods

The experimental method to obtain the stress-strain curve involves the application of several forces on a single protein and the measurement of the resulting deformations. The range of the applied forces must be in such way that it explores the elastic and the plastic regimes of the antibody. The experiments were performed in Hybrid mode AFM (introduced in Chapter 1).

Experimental setup

The experiments were performed in liquid with a commercial Cypher S AFM microscope, (Asylum Research, Santa Barbara, USA). Photothermal excitation was applied to drive the cantilever oscillation. This method enables a proper tracking of the frequency shift of the AFM probe which in turn facilitates the accuracy in the measurements and the transformation of observables into forces.

High resolution images of IgM antibodies were acquired by using excitation forces as close as possible to the one used to excite the cantilever far from the surface $V_{exc,0} \approx 620$ mV. Images at different applied forces were generated by choosing different set-point values in the driving force, usually in the 650 to 720 mV range. The driving force was changed by 10 mV steps. During the imaging process, the dissipated power is calculated by [137, 138]

$$P_{ts} = P_0 \left[\frac{V_{exc}}{V_{exc,0}} - \frac{f}{f_0} \right] \tag{3.8}$$

where $P_{ts} = \pi f_0 \dfrac{kA^2}{Q}$ is the power dissipated by the microcantilever in

the absence of tip-protein forces (for example, with the tip 10-100 nm above the protein surface). In the experiments the power dissipated in the sample was in the 0.3 to 12 fW range.

For the applied forces, a single microcantilever cannot cover the range of forces needed to overcome the elastic regime of the protein (20 to 300 pN). In order to apply forces around 20 pN a soft cantilever has to be used. These cantilevers have their stiffness close to the IgM stiffness value, so when reaching a certain force the cantilever deflects without increasing its applied force on the protein. For that reason very soft cantilevers, AC-40TS cantilevers (Olympus, Japan) with typical values of $k \approx 0.07$ N/m, $f_0 \approx 25$ kHz and $Q \approx 2$ (water), have been used to apply forces in the 20 to 120 pN range. Stiffer cantilevers, OMCL-RC800PSA (Olympus, Japan) characterized by $k \approx 0.76$ N/m, $f_0 \approx 16$ kHz and $Q \approx 2.2$ (water), have been used to apply forces in the 100 to 300 pN range. There is a force region around 100 pN were both cantilevers could be used to perform the measurements. This overlap will enable to record the stress-strain curve without discontinuities. The force constant and the quality factor of the cantilevers were determined using the thermal noise method [23, 24]. The amplitudes used were in the 1.8-2.4 nm range. The AFM images have been processed by using the WSxM software (WSxM solutions) [98].

Sample preparation

To deposit the IgM antibodies and proceed with the measurements, we chose Muscovite mica as a substrate [99]. The first deposition (see Figure 3.2 (a)) was performed by depositing a 20 µl drop of distilled water and injecting a 5 μl drop of IgM antibodies (Chemicon, Inc.) with a concentration of 40 μg/ml on freshly cleaved mica. Figure 3.2 (a) shows an image of the mica with IgM deposited on it. Most of the IgM antibodies do not present the common morphology known in AFM measurements, with a central protrusion [69, 109]. Some of the antibodies which present a hollow in the centre are rounded by a red circle. The conclusion is that these antibodies are adsorbed on the substrate upside-down leaving the central protrusion looking down.

There are other works in the literature in which they show the same results when depositing the antibodies with distilled water [128].

In order to check this assumption, we used $NiCl_2$ to change the charge of the mica surface. The Ni^{2+} ions cover the mica and leave the surface positively charged [135]. A 20 μl drop of 50 mM $NiCl_2$ was deposited for 30 seconds on freshly-cleaved mica to functionalize the surface, and then a 5 µl drop of 40 µg/ml IgM antibodies diluted in PBS was injected. Figure 3.2 (b) shows the mica with IgM deposited on it using $NiCl_2$ solution. The majority of the antibodies display the central protrusion (green circles in Figure 3.2 (b)).
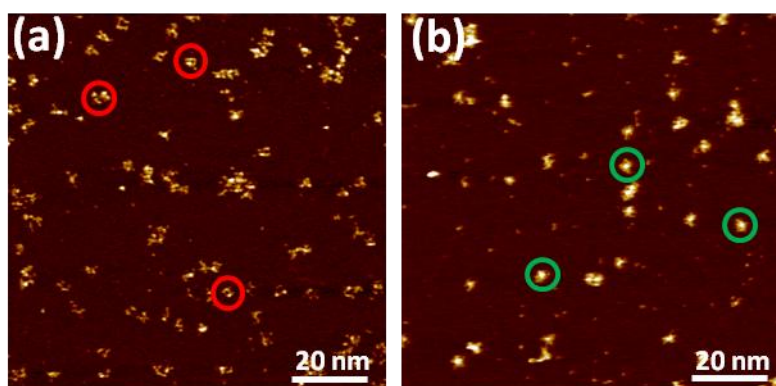
Figure 3.2. AFM topography images of IgM antibodies deposited on mica. (a) IgM antibodies deposited in distilled water solution. (b) IgM antibodies deposited in $NiCl_2$ solution. Red circles mark IgM antibodies with upside down conformations. Green circles show IgM antibodies displaying the central protrusion.

In Figure 3.3 (a) we can observe a small region of the sample, where several individual IgM antibodies can be recognized as well as some aggregated ones. The height values of the antibodies observed in the topography are between 5-7 nm (see Figure 3.3 (b) and the cross section along the dashed line). Considering that there should be a deformation of the antibody when it is adsorbed on the mica due to the interaction between the mica and the antibody, the height measured must be lower than the nominal height.

The measurements were performed with both the proteins and the cantilever-tip ensemble immersed in water at 30ºC. The random deposition process and the flexibility of the proteins generate several morphologies. Notably some molecules show a pentameric structure (Figure 3.3 (b)). The images are in agreement with the structure deduced from homology considerations and cryo-microscopy measurements [109]. Also previous AFM measurements show similar morphologies [69]. The above images represent raw data without corrections from the tip-protein convolution effects.
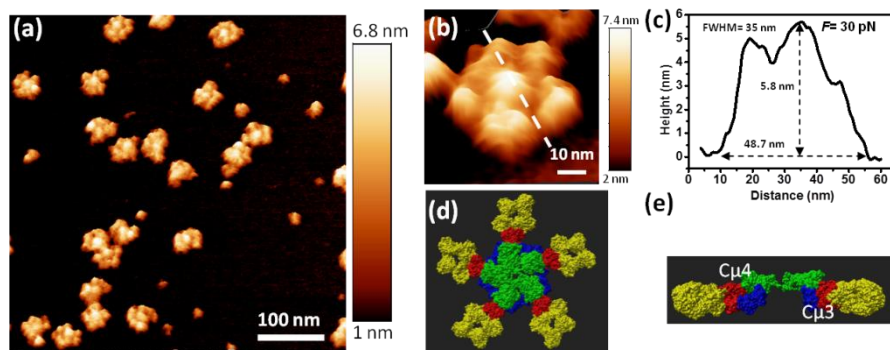
Figure 3.3. High resolution AFM images of IgM antibodies in water. (a) IgM antibodies deposited on a mica surface. Several individual IgM pentamers are imaged. (b) High resolution AFM image of a single IgM. The pentameric structure is fully resolved. (c) Cross-section along the dashed line. Full width at half height maximum is provided. (d) IgM pentamer model. F_{ab} domains are colored in yellow and the central region formed by the association of the F_c tails of the monomers is shown in green, adapted from [94]. (e) Cross-section of the IgM antibody (only two monomers are shown). The Cµ4 and Cµ3 domains are marked, adapted from [94].

Estimation of the deformation

The deformation was calculated by acquiring high resolution images with lateral and vertical values, respectively, of 2 nm and 0.05 nm. By measuring the height difference of the protein before, during and after the application of a given force, we can determine the protein's deformation and its nature, either elastic or plastic (see Figures 3.6 and 3.7). A force causing a plastic deformation will produce a permanent reduction of the maximum protein height. The height measurements are taken on the protein central region, since this region can be easily identified and it is independent of variations in the orientation with respect to the mica surface.

The quantitative data presented in Figures 3.6, 3.7 and 3.8 are values averaged over 10 antibodies which remained in the same conformation with respect to the substrate throughout the experiment.

The deformation of the antibody as a function of the applied forces has been determined by comparing the height of the top of the IgM before and after the application of a force. However, the IgM is also deformed at the smallest force applied here (22 pN). So the absolute deformation must take into account the initial deformation. The initial deformation δ_0 can be calculated from a force curve recorded on the central region of an IgM antibody. In the force curve, the drive voltage, ΔV_{exc}, and the deflection, z_0, as a function of the piezo displacement, z_c, are stored (see Figure 3.4).

The initial deformation can be calculated:

$$\delta_0 = \Delta z_c - z_0 \qquad (3.9)$$

where Δz_c is the difference in piezo displacement between the contact point, z_{c1}, and the imaging point (at the set-point value in the first image, 0.67 V), z_{c2}, and z_0 is the mean deflection of the tip.

By applying the experimental data extracted from the force curve (see Figure 3.4) to equation 3.9, an initial elastic deformation of the central region of 1.1 nm under a force of 22 pN was estimated. The averaged height of the antibody at 22 pN is 6 nm, thus the initial height of the antibody without deformation will be assumed as approximately 7.1 nm. This is also supported by Figure 3.6 (c) where the applied force is represented versus the height on the top of the antibody measured from the images. A height of 7.1 nm is extrapolated from the measured values at a force within the error force value ($\pm$ 5 pN).
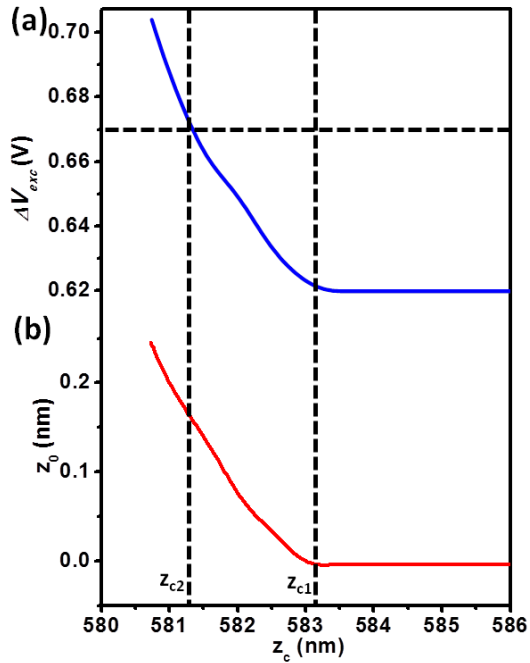
Figure 3.4. Drive voltage (a) and mean cantilever deflection (b) curves taken on top of a single IgM antibody; z_{c1} represents the piezo position at the contact point and z_{c2} is the piezo displacement during imaging. From the difference between z_{c2} and z_{c1}, Δz_c is calculated and the initial deformation, δ_0, is determined by Equation 3.9.

Force estimation

To transform the AFM observables into a quantitative value of force, we have recorded the frequency shift Δf, the driving voltage V_{exc}, and the mean deflection of the tip z_o as a function of the tip-surface distance (see Figures 3.4 y 3.5). The data are recorded by keeping the oscillation amplitude constant. The curves have been acquired at the end of the imaging process to minimize tip damage.

From the force curve data we can reconstruct the force versus tip-antibody distance by using the Sader-Jarvis force reconstruction algorithm [107].

$$F_{ts}(d) = 2k\int_d^\infty X_{sj}dx + 2k\int_d^\infty \frac{\sqrt{A}}{8\sqrt{\pi(x-d)}}\, X_{sj}dx - 2k\int_d^\infty \left(\frac{A^{3/2}}{\sqrt{2(x-d)}}\,\frac{\partial X_{sj}}{\partial d}\right)dx \quad (3.10)$$

$$X_{sj} = \frac{\Delta f(d)}{f_0} \quad\quad (3.11)$$

where k is the spring constant of the cantilever, F_{ts} is the interaction force between tip and sample, f_0 is the unperturbed resonant frequency, Δf is the change in the resonant frequency, A is the amplitude of oscillation and d is the distance of closest approach between tip and sample in an oscillation. By combining the panels of Figure 3.4 and 3.5 we can assign a force to a given ΔV_{exc}.
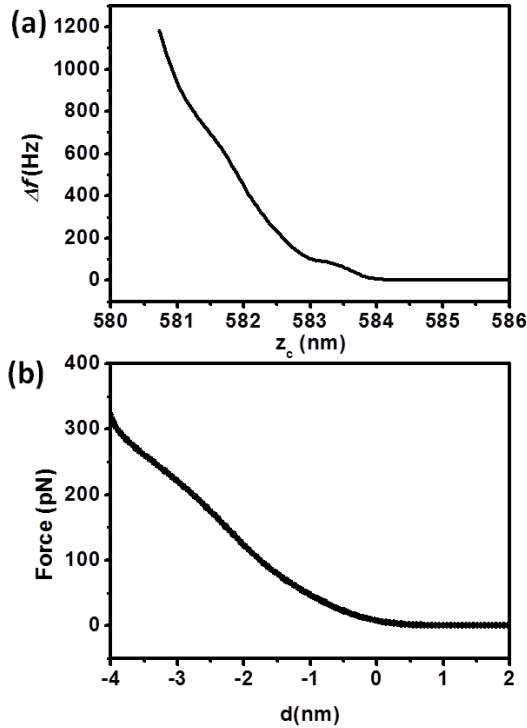
Figure 3.5. (a) Frequency shift curve taken on top of a single IgM antibody. (b) Force versus distance curve reconstructed from the data of (a).

Error in the force

The force is deduced from an integral expression which makes the application of the standard method to determine the error cumbersome. Here, ΔF have been estimated from the reconstructed force curve (see Figure 3.5 (b)) at a given distance d by taking the force values at $d+\Delta d$ and $d-\Delta d$, with $\Delta d=0.05$ nm.

$$\Delta F = |F(d + \Delta d) - F(d - \Delta d)| \qquad (3.12)$$

The uncertainty in the force increases with the force. This is because the slope of the frequency shift curve increases by increasing the indentation (Figure 3.5 (a)).

Error in the stress and the strain

The errors in the stress-strain curve have been calculated by error propagation. The equations used are the following:

$$\Delta\sigma = \sigma\sqrt{\left(\frac{\Delta F}{F}\right)^2 + \left(\frac{\Delta R}{R}\right)^2 + \left(\frac{\Delta\delta}{\delta}\right)^2} \qquad (3.13)$$

$$\Delta\varepsilon = \varepsilon\sqrt{\left(\frac{\Delta\delta}{\delta}\right)^2 + \left(\frac{\Delta h}{h}\right)^2} \qquad (3.14)$$

3.3 Experimental results: Stress-strain curve

The experiment to determine the stress-strain curve of a single IgM protein is divided in two steps. First we perform measurements in the elastic regime by applying very small forces (sub-80 pN range). Finally, we perform measurements at higher forces and observe if we have reached the plastic regime of the protein.

Figure 3.6 (a) shows the cross-section of the central region of the IgM as a function of the applied force. The force applied on the protein is determined by using the method explained in section 3.2. For the experiments exploring the elastic regime, we have applied six forces of 22, 30, 37, 47, 65 and 22 pN. To facilitate the comparison we plot the height cross-sections at F_1=22 pN, F_5=65 pN and F_6=22 pN (Figure 3.6 (b)). The top heights at the beginning of the experiment, F_1, and at the end of the experiment, F_6, coincide. This observation underlines the elastic character of the deformations. We note that by increasing the force from 22 pN to 65 pN the maximum height of the central region decreases by 0.9 nm (Figure 3.6 (c)). Similar results have been obtained with other IgM molecules. We also observe that the small peak associated with a F_{ab} fragment that has disappeared in the profile taken at 65 pN is recovered once the force is lowered to 22 pN.

The lateral component of the force during imaging induces some rotation in the IgM; this could explain the shape mismatches observed at the protein sides.
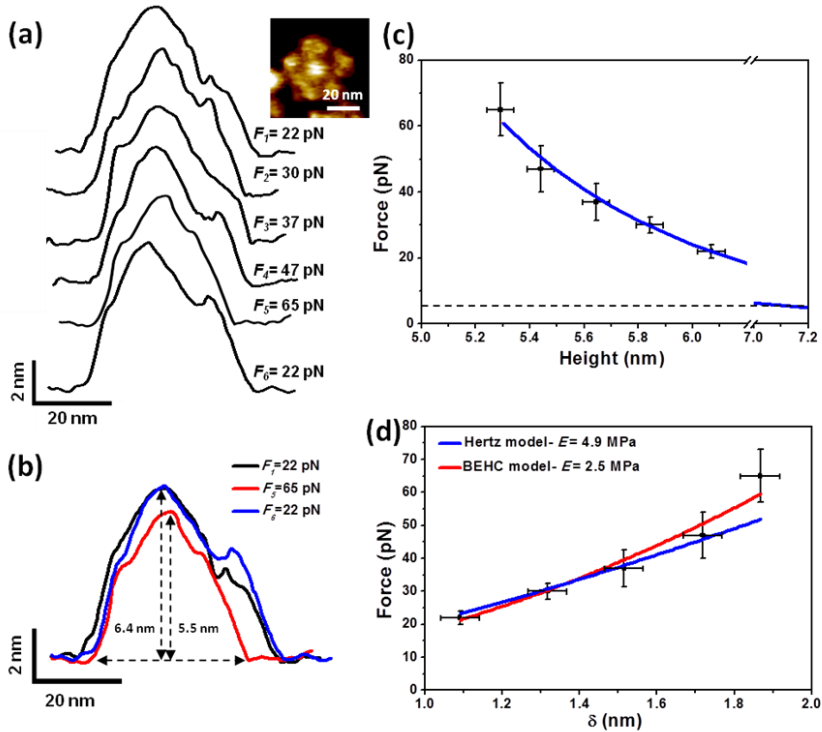

Figure 3.6. Forces and non-permanent deformations on single IgM antibodies in liquid. (a) Deformation of a single IgM under different forces. The experimental run involves the application of six different forces and the measurement of the resulting deformations in the sequential order of 22, 30, 37, 47, 65 and 22 pN. The height profiles have been vertically displaced for clarity. The inset shows an AFM image of the IgM. (b) Comparison of the height profiles for 22 pN (initial), 65 pN (maximum force in this experimental run) and 22 pN (final). (c) Experimental relationship between the applied force and the top height of an IgM. By extrapolating the height data obtained to the estimated height (7.1 nm), we deduce that a force of 5 pN (dashed line) will be needed to measure the IgM with a negligible deformation (~0.1 nm). (d) Plot of the force versus the deformation in the elastic regime. The data is fitted to BEHC and Hertz contact mechanics models.

By fitting the data to contact mechanics models (Figure 3.6 (d)) we can deduce the effective Young modulus of the central region of the IgM pentamer (F_c domains and J-chain). By applying the Hertz contact mechanics model, the value obtained for the Young modulus is 4.9 MPa while, by applying BEHC, a value of 2.5 MPa is calculated. The above values are the same order of magnitude as the ones deduced by computer simulations of AFM dynamics [108]. Hertz contact mechanics gives higher values because it is based on a semi-infinite solid. This assumption might not be satisfied when characterizing very thin specimens such as an IgM protein (~7 nm).

To determine the complete stress-strain curve of an IgM requires to apply forces that produce plastic deformations. By using a stiffer cantilever (~0.7 N/m) we were able to apply forces of a few hundreds of pN (Figure 3.7). The experiments show an IgM that has been imaged at 230 pN then at 315 pN and finally at 230 pN. The three height profiles do not coincide which indicates a plastic deformation. This is in contrast with what was obtained by applying smaller forces (Figure 3.6(b)).

To transform the data of Figures 3.6 and 3.7 into a stress-strain curve we have calculated a mean compressive stress over the protein central region by using the equation [139, 140]

$$\sigma = \frac{F}{\pi a^2} = \frac{F}{\pi R \delta} \tag{3.15}$$

where F is the applied force and a the contact radius, which is defined as $a = \sqrt{R\delta}$. The yield strength was determined from the above equation by measuring the smallest force F_m that generates a permanent deformation of the central region of the antibody. This also will determine the yield point.

By introducing the elastic and plastic deformation data into Equation 3.15 we generate the stress-strain curve of the central region of the antibody (Figure 3.8 (a)).
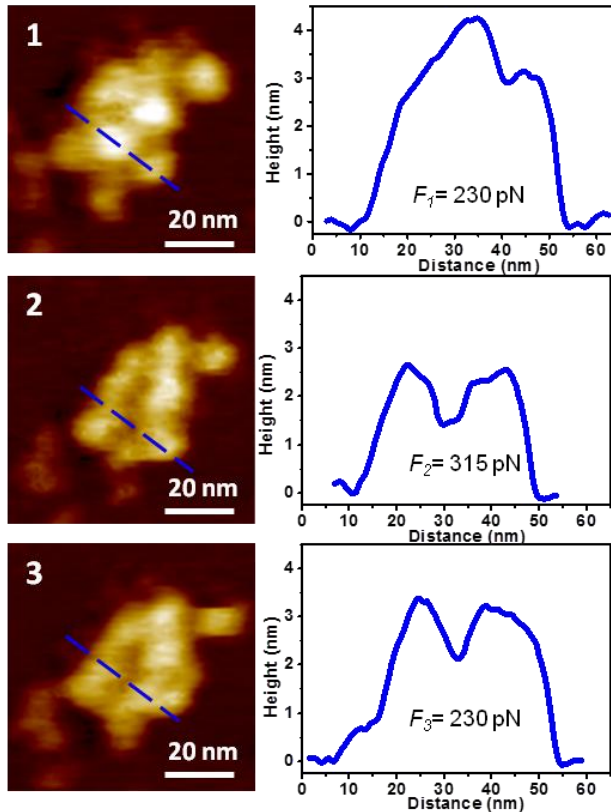

Figure 3.7. Protein plastic deformation. Images and height profiles of a single IgM before and after the onset of plastic deformation. The right panel shows the profile across the marked line in left panel. The forces applied during imaging are indicated.

The curve shown in Figure 3.8 shows the elastic and plastic regimes. In particular, the elastic region is divided in two sections. First, the stress increases linearly with the strain (0.15 to 0.3 range). We propose that the mechanical response in this region is dominated by the elastic deformation of Cμ4 domains (mostly beta-sheets) (see Figure 3.3 (e)).

At higher strains (0.3-0.4) there is a significant increase in the slope. This could indicate the participation of Cμ3 domains. Those domains lie below the Cμ4 domains in the mushroom shaped IgM structure [109]. The shaded region (strains below 0.15) has not been measured. To access that region requires the application of forces in the sub-10 pN range which is beyond the state-of-the-art of the AFM.
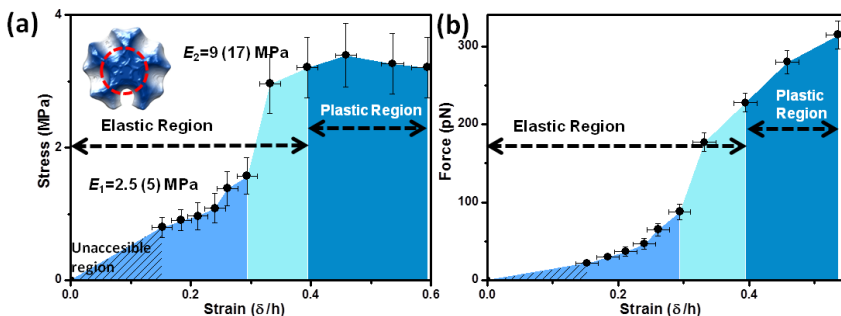

Figure 3.8. (a) Stress-strain curve of a pentameric IgM in liquid. The elastic and plastic regions are marked. The measurements are performed on the central region of the antibody (inset, ~15 nm in diameter). This region is formed by five F_c domains and the J-chain. The Young modulus values have been corrected from the influence of the substrate. The values obtained directly from the slope of stress-strain curve are indicated in parenthesis. (b) Forces applied to determine the stress-strain curve. The shaded region involves the application of forces beyond the state-of-the art of AFM.

The strain values can be compared to the ones obtained in previous studies on proteins. A previous study [141], in which the plastic regimes of Bovine Serum Albumin and Myoglobyn monolayers have been probed by micro-mechanical experiments, showed that the plastic regime of this globular proteins is reached at lower strains that the ones applied in the experiments, between 0.37-0.4. Those proteins consist predominantly of α-helices and have a molecular weight between 20-70 kDa. The region of the antibody that we are probing is the central protrusion. This protrusion is formed by linking the F_c region of each monomer by disulfide bonds and has a molecular weight of 52 kDa.

Interestingly, studies of protein unfolding show that proteins formed of β-sheet can withstand larger forces than proteins composed of α-helix [142]. According to these results, the antibody, consisting predominantly of β-sheet, will need higher strains to enter the plastic regime as compared to α-helix based proteins.

The shape of the above stress-strain curve has some similarities with some curves measured on macroscopic polycrystalline materials such as iron alloys [118]. However, the maximum stress of a single protein before plastic deformation is about two orders of magnitude smaller than the one of a metal. In addition, the central region of the IgM is about 10^2 times more deformable than some iron alloys. The stress-strain curve reported here shows similarities as well as differences with respect to the curves obtained from macroscopic measurements performed on elastic proteins [143-145]. These differences come from the fact that IgM antibodies present a complex structure so the elastic response of the different regions in the protein is mixed.

In the elastic regime, the Young modulus is the proportional factor between the stress σ and the strain ε

$$\sigma = E\varepsilon \qquad (3.16)$$

From the stress-strain curve we obtain slopes of 5 MPa and 17 MPa for the first and second elastic regions. However those numbers should take into account the influence of the rigid mica substrate on the measurements. After the correction we obtain 2.5 and 9 MPa. We note that at low strains the Young modulus derived from the stress-strain curve and the one deduced from the force curve (Figure 3.6 (d)) are identical. The central region (F_c fragments and J-chain) can sustain elastic strains of 0.4 (about 40% of the nominal protein height, 7.1 nm). These values explain the capability of IgM antibodies to sustain multiple collisions with other proteins, cells and tissues without any loss of biological functionality. The thermal energy, $k_b T \approx 4.1$ pN·nm, produces forces of 4 pN over distances of nanometers.

The maximum contact stress for thermal induced collisions is estimated from the thermal energy to be in the 0.1-0.5 pN/nm^2 range. This value is a few times smaller than the yield strength of the IgM (3.2 pN/nm^2). The yield strength of the protein also places a limit to the value of the forces used for high resolution and non-invasive imaging of biomolecules [31, 49, 83, 135, 146-148]. Those forces are going to depend on the measured protein. However, for globular proteins with a secondary structure dominated by β-sheets, we expect a similar trend, consequently forces above 200 pN (see Figure 3.8 (b)) should not be applied during AFM imaging.

Furthermore, if we look at some of the biological functions of the IgM antibody [133], such as complement activation or antibody-induced apoptotic effects on tumors, we note that the antibody elasticity has to be such as to allow the passing of several endothelial barriers of lymphatic and blood vessels. These endothelial barriers have a pore size of roughly 20 nm with a separation gap of 4 nm [149].

3.4 Conclusions

A force microscopy method has been developed to quantify the softness of a single antibody pentamer by measuring the stress-strain curve. The method enables to control the application of 20 pN forces in liquid and at room temperature with force and deformation resolutions, respectively, of 5 pN and 50 pm. The stress-strain curve shows three distinctive regions. For low strains, the protein's central region shows that the stress and strain are proportional (elastic regime). This region has an average Young modulus of 2.5 MPa. For strains between 0.25 and 0.4, the data suggests a different elastic region where the stress is roughly proportional to the strain with a Young modulus of 9 MPa. Higher strains lead to generation of irreversible deformations (plastic regime). The existence of two different elastic regions is explained in terms of the complex structure of the antibody central region.

The Young modulus of the central region of the protein measured from force curves and contact mechanics models coincides with the one deduced from the stress-strain curve. This agreement validates the hybrid dynamic AFM method to determine the stress-strain curve of proteins. The deformability of the antibody explains its capability to sustain multiple collisions without any loss of biological functionality.

Chapter 4

Bimodal force microscopy in the FM-FM configuration

4.1 Introduction

A method that combines high spatial resolution, quantitative and non-destructive mapping of surfaces and interfaces is a long standing goal in nanoscale microscopy. The method would facilitate the study of polymers, biomolecules and cells elasticity as well as the development of hybrid devices and materials made up of nanostructures of different properties.

In the recent years several methods have been proposed to complement the high spatial resolution of the force microscope with quantitative information about the mechanical properties of the interface [55, 59, 77-80, 123, 150, 151]. The nanomechanical information that a force microscope can obtain from a surface includes elastic and dissipative components. These components are contained in the force measured in quasi-static equilibrium, as a function of the tip-surface separation (force curve). Therefore, in order to determine the elastic and dissipative elements a dynamic measurement of the force is required.

Most of the new quantitative AFM methods use the combination of acquiring force curves at a single point of the surface with AFM imaging [152]. This approach has been very successful and it has been further developed in combination with several contact and near-contact AFM imaging configurations [121], however, it has some limitations. First, the sensitivity of the force curve depends on the cantilever force constant. Thus the use of the same cantilever for measuring heterogeneous surfaces is cumbersome, especially if the material has large variations in the elastic modulus. Second, it requires to collect a large number of data points per pixel in order to recover the material properties with reasonable accuracy. Those difficulties have set motivation to develop nanomechanical spectroscopy methods based on the use either amplitude or frequency modulation AFM methods. Besides, this approach allows the use of analytical expressions that relate the observables to the nanomechanical properties.

In this chapter, the bimodal AFM operated in the FM-FM configuration will be introduced. Bimodal FM-FM AFM method is based on the bimodal excitation concept. This mode enables the simultaneous mapping of the nanomechanical spectra of soft matter surfaces with nanoscale spatial resolution. The method has been implemented in a commercial microscope and has been applied to different samples in air and liquid. The fundamental steps for the implementation of the method are explained along with the experimental conditions to obtain good contrast in the bimodal channels. The nanomechanical properties include the Young modulus and the viscous or damping coefficients. In addition, it provides the peak force and the indentation. The method does not limit the data acquisition speed nor the spatial resolution of the force microscope. It is non-invasive and minimizes the influence of the tip radius on the measurements. The same tip has been used to measure in air heterogeneous interfaces with near four orders of magnitude variations in the elastic modulus, from 1 MPa to 3 GPa.

4.1.1 Theoretical model

The theoretical model described here was developed by Elena T. Herruzo and Ricardo García [105]. In order to obtain the nanomechanical properties simultaneously with the topography image in Bimodal AFM is necessary to relate the observables with the interaction force.

In bimodal frequency modulation AFM, the frequency shift of any mode is related to the force by [105, 151, 153]

$$\Delta f_i(d_m) = -f_{0i} \frac{\langle F_{ts} z_i \rangle_{Ti}}{k_i A_i^2} = \frac{f_{0i}}{k_i A_i^2} \frac{1}{T_i} \int_{T-\frac{T_i}{2}}^{T+\frac{T_i}{2}} F_{ts}(z_c - z_1 - z_2) z_i dt \qquad (4.1)$$

where f_{0i}, k_i and A_i stand, respectively, for the resonance frequency in the absence of a force, the force constant and the amplitude of mode i. z_c is the mean tip-surface separation and d_m is the closest distance between tip and sample in an oscillation cycle. The above Equation (4.1) can be considered a generalization of the expression used in conventional frequency modulation AFM for the fundamental mode [154].

The closest distance between tip and sample in an oscillation cycle is expressed as,

$$d_m = z_c - A_1 - A_2 \qquad (4.2)$$

On the other hand, because $A_1 \gg A_2$ the frequency shifts depend on the mode [105]. In particular for modes 1 and 2, the frequency shifts are expressed as

$$\Delta f_1(d_m) = \frac{f_1}{k_1 \sqrt{2\pi A_1^3}} I_-^{1/2} F(d_m) \qquad (4.3)$$

$$\Delta f_2(d_m) = \frac{f_2}{2k_2 \sqrt{2\pi A_1}} D_-^{1/2} F(d_m) \qquad (4.4)$$

Where the fractional integrals and derivatives are calculated by using the Riemann-Liouville fractional calculus [106],

$$I_{-}^{1/2}F(z) = \frac{1}{\Gamma(1/2)} \int_{z}^{\infty} \frac{F(z)}{(t-z)^{1/2}} dt \qquad (4.5)$$

$$D_{-}^{1/2}F(z) = \frac{(-1)}{\Gamma(1/2)} \frac{d}{dz} \int_{z}^{\infty} \frac{F(z)}{(t-z)^{1/2}} dt \qquad (4.6)$$

We have used two main hypotheses to deduce the Equations 4.9 and 4.10 as follows: (a) A_1 is larger than the typical length scale of the interaction force and (b) A_2 should satisfy Equation 4.7,

$$A_2 << 2 \left| \frac{F_{ts}''\ (z_1(t))}{F_{ts}'''\ (z_1(t))} \right| \qquad (4.7)$$

The fulfillment of the above hypothesis can be checked experimentally by recovering the force with Sader method [155] and comparing its numerical half integral with the results given by Equation 4.3 and its numerical half derivative with the results given by Equation 4.4.

The tip-surface force includes both conservative and dissipative interactions, which are modeled, respectively, by Hertz contact mechanics and the Kelvin-Voigt viscoelastic model. Then the tip-surface force is expressed by

$$F_{ts}(d) = F_{con} + F_{dis} = \frac{4}{3} E_{eff} \sqrt{R}\delta^{3/2} - \eta\sqrt{R\delta}\ \dot{\delta} \qquad (4.8)$$

where d is the instantaneous tip-sample distance, R is the tip radius, δ is the sample indentation ($\delta = a_0 - d$, with $a_0 = 0.165$ nm), η the viscous coefficient and E_{eff} is the effective Young modulus of the interface as introduced in Chapter 3 (Equation 3.4).

Since the probe Young modulus E_{tip} is at least two orders of magnitude larger than those of the samples studied, here $E_{eff} \sim E_s$. Long-range attractive forces and capillary forces have not been considered because the experiments are performed with sharp tips and under dry nitrogen environments. Under those conditions the dominant forces are short-range repulsive (contact) forces.

The fractional integrals and derivatives of a specific force, Equation 4.8, lead to a relationship between the frequency shifts and the effective Young modulus and the indentation,

$$\Delta f_1(d_m) = \sqrt{\frac{R}{8A_1^3}}\, \frac{f_{01}}{k_1}\, E_{eff}\, \delta^2 = \beta_1 E_{eff}\, \delta^2 \tag{4.9}$$

$$\Delta f_2(d_m) = \sqrt{\frac{R}{8A_1}}\, \frac{f_{02}}{k_2}\, E_{eff}\, \delta = \beta_2 E_{eff}\, \delta \tag{4.10}$$

where for $d_m \leq 0$, $\delta = a_0 - d_m$ with $a_0 = 0.165$ nm.

Similarly, the viscosity is related to the experimental observables by [156]

$$\Delta F_{01}(d_m) = F_{01}\left(\frac{\Delta f_1(d_m)}{f_1} + \frac{\sqrt{2\pi}Q_1 f_1}{k_1 A_1^{3/2}}\, I_-^{1/2} B(d_m) \right) \tag{4.11}$$

$$\Delta F_{02}(d_m) = F_{02}\left(\frac{\Delta f_2(d_m)}{f_2} + \frac{\sqrt{2\pi}Q_2 f_2}{k_2 A_1^{1/2}}\, I_-^{1/2} \Gamma(d_m) \right) \tag{4.12}$$

where

$$B(x) = 2\int \eta\sqrt{R\delta}\, dx \tag{4.13}$$

$$I_-^{1/2} B(d_m) = 0.5\sqrt{\pi R}\, \eta \delta^2 \tag{4.14}$$

The combination of Equation 4.1 with the use of fractional calculus methods [105, 155, 156] and the bimodal scheme developed here enables the application of the following analytical expressions relating the observables and material properties,

$$E_{eff} = \sqrt{\frac{8}{RA_1} \frac{k_2^2}{k_1} \frac{f_{01}}{f_{02}^2} \frac{\Delta f_2^2}{\Delta f_1}}$$ (4.15)

$$\eta = \sqrt{\frac{2}{\pi^2 RA_1} \frac{k_2^2}{Q_1 k_1} \frac{1}{f_{02}^2} \frac{\Delta f_2^2 (\Delta F_{01} f_{01} - \Delta f_1 F_{01})}{\Delta f_1^2 F_{01}}}$$ (4.16)

where F_{0i} and ΔF_{0i} are, respectively, the initial excitation force and the change in the excitation force needed to keep the A_i constant. The viscosity may be calculated with the first mode resonance frequency or with the second mode resonance frequency by using Equation 4.11 or 4.12. The indentation is calculated by

$$\delta = A_1 \frac{k_1 f_{02}}{k_2 f_{01}} \frac{\Delta f_1}{\Delta f_2}$$ (4.17)

4.2 Conditions for bimodal operation

To perform bimodal AFM experiments some key experimental requirements must be taken into account. They are mainly experimental considerations which have been studied along the development of this thesis but have been found to be crucial for the correct conversion of the observables to nanomechanical properties. These conditions are applicable to all bimodal configuration modes, although some of the ones presented here are studied in the bimodal AM-AM configuration.

Channel contrast

In order to transform the observables to nanomechanical properties through the equations presented before, the images have to present good contrast. Few previous studies have shown that the operational parameters selection, such us the relative kinetic energy between the higher mode and the first mode, plays an important role in bimodal operation [157-159]. In this section, the dependence of the amplitude ratio, first and second mode, on the contrast of the second mode amplitude and phase for Bimodal AM-AM operation in air is presented.

In Figure 4.1 the dependence of the free amplitude on the contrast of the second mode amplitude and phase channels is studied. The images display an area of a device with nanoscale patterns fabricated by oxidation scanning probe lithography (oSPL) obtained by a member of the Forcetool group (Dr. Yu Kyoung Ryu). The experimental parameters of the cantilever used in this experiment are $k_1 \approx$ 24 N/m, $k_2 \approx$ 1064 N/m, $f_{01} \approx$ 305 kHz, $f_{02} \approx$ 1.84 MHz, $Q_1 \approx$ 490, $Q_2 \approx$ 702, and the free amplitudes for each image are indicated in Figure 4.1. Silicon oxide (SiO_2) stripes and the silicon (Si) substrate covered by IgM antibodies can be distinguished in the image. For each image the set-point was chosen so that the measurements were carried out in the repulsive regime.

Figures 4.1 (a)-(b) and (d)-(e) show the enhancement in the contrast in both channels second mode amplitude and phase, when increasing the second mode free amplitude. In Figure 4.1 (b) and (e) the SiO_2 dots are clearly distinguishable from the Si substrate, which did not happen in the former configuration, see Figures 4.1 (a) and (d). Despite the fact that the amplitude ratio in (a)-(d) is larger than in (b)-(e) there is a minimum free amplitude of the second mode, in this case greater than 0.2 nm, required to obtain good contrast in the second mode channels. Figures 4.1 (b)-(c) and (e)-(f) are taken by increasing the first mode and second mode free amplitudes but maintaining the amplitude ratio constant. This increment is also contributing to the enhancement of both, second mode amplitude

and phase channels. It can be observed that, even though the contrast between the Si substrate and the SiO_2 dots was already achieved in Figure 4.1 (b), (e), the IgM antibodies did not present a different value than the SiO_2 dots, but in this third configuration they are certainly detectable in the second mode amplitude channel.
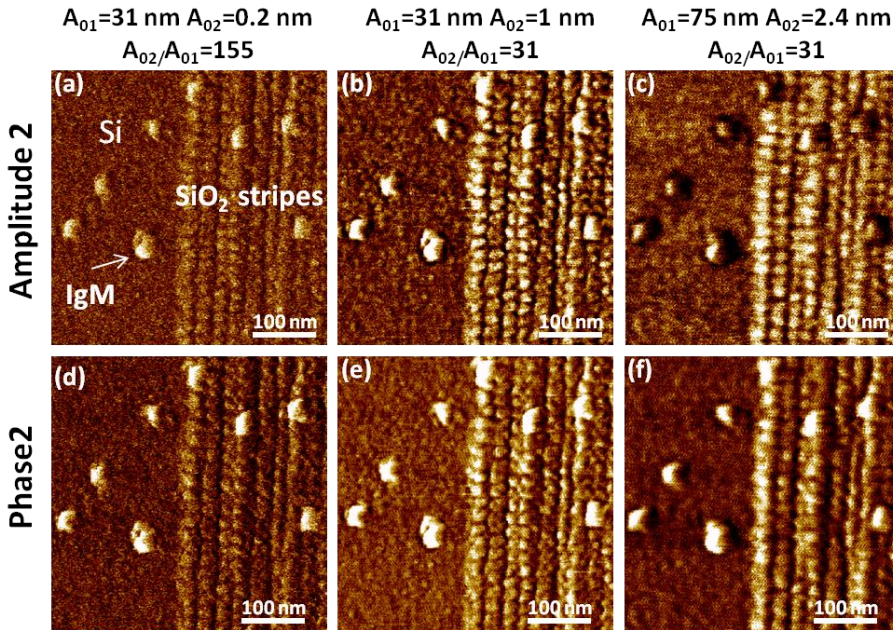

Figure 4.1. Bimodal contrast enhancement on a silicon substrate with SiO_2 dots made by oSPL and IgM antibodies. (a), (b) and (c) Second mode amplitude channel AFM image taken with the described conditions. (d), (e) and (f) Second mode phase channel AFM image taken with the described conditions.

In addition, the contrast in the bimodal channels could be different in the trace or the retrace image. This could be due to asperities on the tip which interact with the sample when the tip is scanning in one specific direction but not in the other. This was not demonstrated so the factors that can produce the difference in contrast between trace and retrace are not clear yet.

To summarize, an enhancement of the contrast in the second mode channels has been observed when the amplitude ratio is maximized but to have a minimum value of the second mode free amplitude is a fundamental requirement.

FM gains calculation

When operating in FM, the feedback gains need to be calculated. In the Asylum Research software these gains can be calculated automatically. The equations used for determining the gains are the ones presented in the paper by Kilpatrick *et al.* [52]. They modelled the mechanical response of the cantilever as well as the instrumental characteristics to calculate the gains for stable feedback loop tuning in low Q systems. The Asylum Research software allows choosing between the calculation of conservative gains (it extracts the *Q* factor from the thermal fit) or non-conservative gains (it extracts the *Q* factor from the tuning fit).

 It has been observed that there is no difference in using the conservative or the non-conservative gains in air but in liquid is an important factor. The gains calculated in the experiments performed in liquid are non-conservative. Most of the times, gains have to be changed while imaging in order to obtain good contrast in the channels. This is easy when the second mode is the one operating in FM because is not the main feedback for the topography and the stability of the measurement is not compromised. However, when using FM as the main feedback, the gains change may produce instabilities in the measurement and even the tip could get dirty or could break if the gains are not properly calculated.

Resonance peak selection

As previously shown [160], when the cantilever approaches to the sample the resonance frequency moves to the left (lower frequencies) before feeling the tip-sample interaction due to the hydrodynamic damping.

Sometimes it is very useful to place the resonance frequency a few Hertz to the left before engaging. This could make imaging more stable or even give a better contrast because the excitation frequency will be closer to the resonance frequency at the engage. This is valid for both first and second mode. Another possibility to avoid the shift in resonance frequency is to set it 50-100 nm above the sample. This approach is very accurate for cantilevers with high resonance frequencies.

4.3 Experimental setup

In Figure 4.2 the experimental setup for bimodal FM-FM AFM is shown. In this bimodal operation setup the two first eigenmodes are operated in frequency modulation. The frequency shift of the first flexural mode Δf_1 is kept at a fixed value during imaging while the oscillation amplitude is kept constant (A_1 = constant) in the presence of dissipation by changing the excitation signal ΔF_{01}. The changes in the frequency shift are followed by keeping the phase shift locked at 90° with a phase-locked loop (PLL). Thus, the first mode has two feedback loops. In the second mode the changes of the resonance frequency are recorded while imaging (ϕ_2=90° with a PLL) and the oscillation amplitude is kept constant (A_2 = constant). Therefore, the second mode has another two feedback loops. Altogether with the feedback to track the topography, the instrument has five different feedback loops for feedback control.
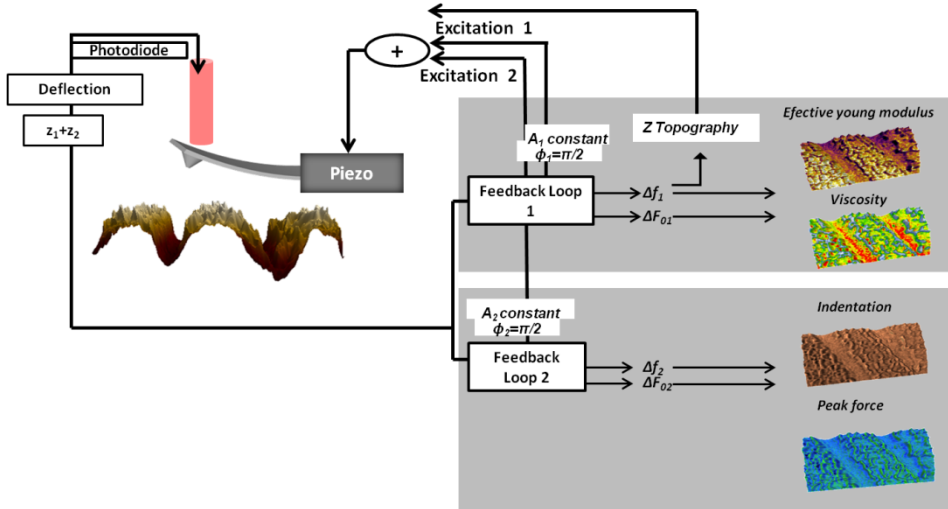
Figure 4.2. Experimental setup of FM-FM bimodal AFM. Four feedback loops keep the amplitudes of the first and second mode fixed, and the phase-shifts of the first and second modes to 90º as the cantilever scans heterogeneous sample. Analytical relationships enable the conversion of Δf_1 and Δf_2 data into quantitative maps. The additional feedback loop which generates the topographic image regulates the mean tip-sample distance by keeping the first mode frequency shift, Δf_1, constant.

In bimodal AFM, the amplitude of the first mode A_1 is more than one order of magnitude larger than the amplitude of the second mode. Two things are gained by using this asymmetry: first, the operation of the microscope is stabilized by the first mode; second, A_2 can be considered a small perturbation of the total amplitude (A_1+A_2) which facilitates the derivation of the analytical expressions explained in the theoretical model.

The experimental setup has been implemented in a commercial AFM (Cypher, Asylum Research). We have written all the codes and developed the user interface by using IgorPro software. Figure 4.3 shows the user interface. The FM panel window for the first mode is shown in Figure 4.3 (a). In this panel the user may select to turn both feedbacks phase and amplitude, either on or off.

The gains are also calculated here and the second mode amplitude is introduced. The FM panel is already programmed in the microscope software for FM imaging. Taking inspiration from this panel, the same panel for the second mode in FM has been programmed (see Figure 4.3 (b)). The new panel displays the same fields to fill in the parameters and to switch the feedbacks on or off. This panel will be the same as the one used in Chapter 5 for bimodal AM-FM AFM operation.
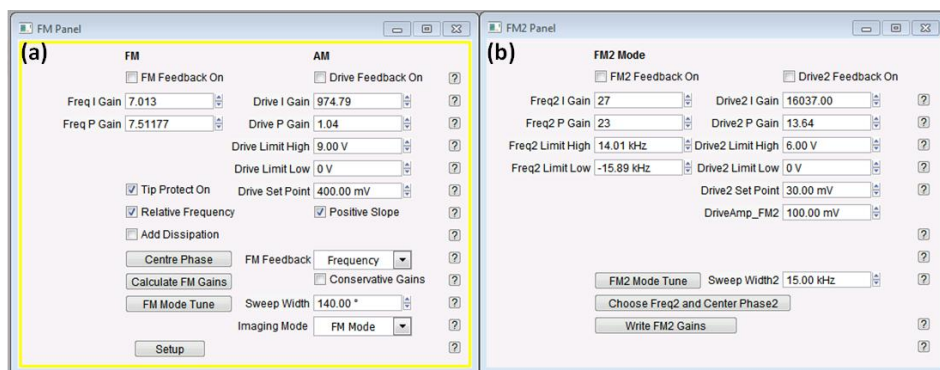

Figure 4.3. User interface to select the frequency modulation loops parameters. (a) Frequency modulation panel for the first mode. (b) Frequency modulation panel for the second mode.

4.4 Experimental results

Here, the application of the method on different samples is shown. All the AFM data showed in the next section has been acquired at a scan frequency for the fast x axis between 2-5 Hz. For the experiments performed in air, typical values for the first and second amplitudes were, respectively, 15-90 nm and 0.3-0.6 nm.

4.4.1 Experiments in air

Polymers

Three polymer samples have been used to apply the method. A polymer blend made of polystyrene (PS) regions (nominal value of $E_{PS} \approx 2.0$ GPa) and polyolefin elastomer (ethylene-octene copolymer) (LDPE) (nominal value of $E_{LDPE} \approx 0.1$ GPa). Two types of polydimethylsiloxane (PDMS) surfaces have been also used, with macroscopic elastic moduli of 3.5 MPa and 2.5 MPa. All samples were acquired from Bruker AFM probes.

The other polymer used is a block copolymer polystyrene-b-poly(methyl methacrylate) (PS-b-PMMA) layer. The length of the PS-b-PMMA is 34 nm and the layer thickness (average value) is about 50 nm. The polymer film was prepared as described in reference [161].

Calibration of the force constants

To obtain mechanical properties from the sample by using AFM, a contact mechanics model to describe the tip-sample interaction must be used (see Chapter 3). In order to select and apply a contact mechanics model some requirements have to be taken into account. First, contact mechanics models are not valid for all types of materials. There is a range of application of the different models based on the applied force, the deformation or the adhesiveness of the material [19, 162]. The adhesion map of Johnson and Greenwood [163] is a useful tool to select among contact mechanics models. Second, some experimental and material parameters, such as cantilever calibration or Poisson's ratio, must be known. In this section the calculation of some of these parameters, specifically, the tip radius and the cantilever stiffness are shown. The procedures presented here to calibrate the cantilever will be applied for all the experimental results unless stated otherwise.

The force constants and quality factors are determined by using the thermal noise method [24, 164]. All the data presented in this subsection (i.e. Experiments in air) was obtained by using two kinds of cantilevers. Cantilever 1 (SSS-NCL SuperSharpSilicon cantilever, Nanoworld) is characterized by f_{01}=152860 Hz, k_1=22 N/m, Q_1=366, f_{02}=950533 Hz, k_2=850 N/m, Q_2=474. Cantilever 2 (NCHV, Bruker) is characterized by f_{01}=292214 Hz, k_1=9.2 N/m, Q_1=434, f_{02}=1.8343 MHz, k_2=362 N/m, Q_2=620.

The calibration procedures of the optical sensitivity and the stiffness of the first mode of the cantilever have been explained in Chapter 1. For the calibration of higher eigenmodes two different calibration methods were used. The first method is the calculation of the stiffness through the resonance frequency of the first and second modes, f_{01} and f_{02}, and the expression for an ideal Euler-Bernoulli beam [55],

$$k_2 = k_1 \left(\frac{f_{02}}{f_{01}} \right)^2 \tag{4.18}$$

It has been recently shown by Labuda *et al.* [165] that since real AFM cantilevers cannot be described as ideal Euler-Bernouilli beam, the power-law relationship does not always scale to the square but to some arbitrary power exponent, ζ. They have calculated the power-law exponent, ζ, for some commercials cantilevers by interferometric calibration. For the measurements performed with PPP-NCH (Nanosensors) cantilevers, the second mode spring constant is determined by the theoretical relationship between the force constant of the 1st mode and the 2nd mode, Equation 4.18, but instead of using 2 as the power-law exponent, using ζ=2.17.

The second method is based in the relationship between the first and second mode optical lever sensitivity for an ideal Euler-Bernoulli beam,

$$s_2 = \frac{s_1}{3.47} \tag{4.19}$$

 With the second mode sensitivity known, the second mode stiffness is calibrated by the thermal noise method [23, 24].

Tip radius estimation

A protocol to obtain the tip radius and also to select or disregard the experimental data is developed in the bimodal FM-FM configuration. Equation 4.15 can be rewritten to show a linear relationship between Δf_1 and Δf_2^2 when the Hertz contact mechanics model is applied,

$$\Delta f_1(d_m) = \alpha(E_{eff}, R)\Delta f_2^2(d_m) \qquad (4.20)$$

where d_m is the closest distance between tip and sample. Consequently only the data compatible with Equation 4.20 can be used for the nanomechanical measurements. A factor to consider is that the presence of large adhesion forces and/or the use of a tip with an irregular geometry modifies the relationship between the excited frequencies so the above linear dependence is no longer observed. Besides, as mentioned before, the above relationship is strictly valid for Hertz contact mechanics. Materials described with different contact mechanics models, Sneddon model or Van der Waals forces, will have a different relationship between Δf_1 and Δf_2.

Figure 4.4 shows the relationship between Δf_1 and Δf_2^2 obtained for three polymer surfaces, polystyrene (PS) in Figure 4.4 (a), polyolefin elastomer (ethylene-octene copolymer) (LDPE) in Figure 4.4 (b) and Polydimethylsiloxane (PDMS) in Figure 4.4 (c), with their Young modulus (E_s) ranging from about 1 MPa to 3 GPa. The linear dependence between Δf_1 and Δf_2^2 shown in Figure 4.4 validates the use of the experimental data in Equations 4.15, 4.16 and 4.17 to obtain the nanomechanical properties.

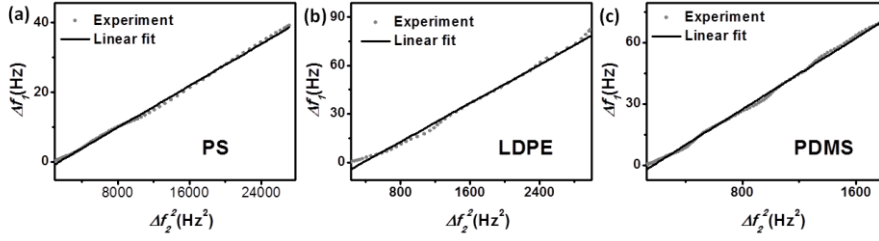Figure 4.4. Linear relationships between 1st and 2nd flexural modes. (a) PS (~2.0 GPa). (b) LDPE (~0.1 GPa). (c) PDMS (~2.5 MPa). The experimental data should bear a linear relationship between Δf_1 and Δf_2^2 to apply the method. A_1= 40 nm.

Once the data is validated, the tip radius can be determined from the slope of the linear fit, α, and the cantilever and operational parameters:

$$R = \frac{1}{\left(E_{eff}\alpha\right)^2} \frac{8}{A_1} \left(\frac{k_2^2 f_{01}}{k_1 f_{02}^2}\right)^2 \tag{4.21}$$

The same cantilever-tip system has been used to get the data (SSS-NCL, Nanoworld). For determining the effective tip radius in the experiments performed in air, a polystyrene sample with a nominal value of 2.7 GPa was used in the case of the blend sample and the block copolymer. For the PDMS sample, one of the PDMS calibrated samples was used.

Indentation

It is well-known that there is a dependence of the elastic modulus obtained in AFM measurements on the indentation depth [166, 167]. This dependence is an artifact produced by the tip sharpness and the adhesion between the tip and sample surfaces. In order to reach the bulk modulus of the material certain indentation is needed. Force curves have been performed to study the indentation depth necessary to obtain a constant value of the elastic modulus on different polymers. These materials are the same that have been used to validate the method.

In Figure 4.5 the dependence of the elastic modulus calculated by Equation 4.15 on the depth indentation is shown. For the PS, with a Young modulus of 2.1 GPa, the indentation needed to obtain the bulk modulus is almost 2.8 nm. For indentations smaller than 2.8 nm the obtained modulus is overestimated due to the stresses caused by the sharp tip and the surface material interaction. The softer the material is, the deeper the indentation required to reach the bulk modulus. Therefore, for the LDPE, an indentation of 7 nm is needed (see Figure 4.5 (b)). For the PDMS, two calibrated samples have been tested. The first one corresponds to 2.5 MPa and the second one to 3.5 MPa. The indentation needed for both samples is near 12 nm as displayed in Figure 4.5 (c). Given these results, the technique can be implemented now within the range of values calculated for the indentation depth.
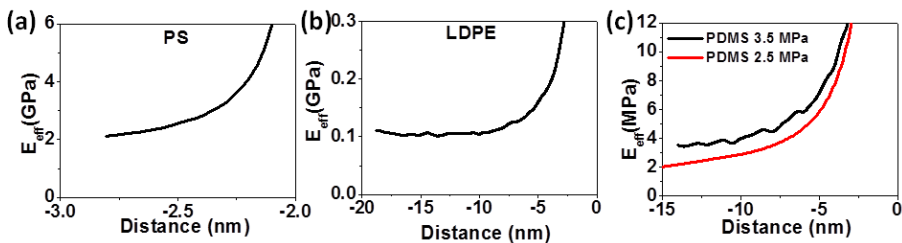

Figure 4.5. Indentation depth calibration curves. (a) Elastic modulus curve on PS. (b) Elastic modulus curve on LDPE. (c) Elastic modulus curve on the two PDMS calibrated samples.

Implementation of the technique

Bimodal AFM maps have been recorded on the polymer blend made of circular regions of LDPE embedded in a matrix of PS.

The above regions have nominal Young modulus of 100 MPa and 2.0 GPa. The Poisson ratio is 0.35 for LDPE and 0.34 for PS. In Figure 4.6 maps of the experimental observables, Δf_1, Δf_2, ΔF_{01} and ΔF_{02}, are shown. The AFM image shows a series of circular regions with a diameter that varies between 1 and 2 μm surrounded by relatively flat regions. The AFM image has been taken by changing the set-point parameter of the main feedback seven times from $\Delta f_1 = 37$ to 97 Hz (approximately every 450 nm in the *y*-axis). This is reflected in the color-coded maps of the observables (Figure 4.6 (a), (b), (c), (d)). The corresponding histograms show between 7 and 9 peaks (Figure 4.6 (e), (f), (g), (h)). In the case of $\Delta f_1(x,y)$, the peaks are imposed by changing the main feedback value while for the other maps the peaks reflect both the changes in the feedback and the changes of the nanomechanical response of the sample. For example, the $\Delta f_2(x,y)$ map show 9 peaks, seven coming from the PS regions and two from the elastomer.
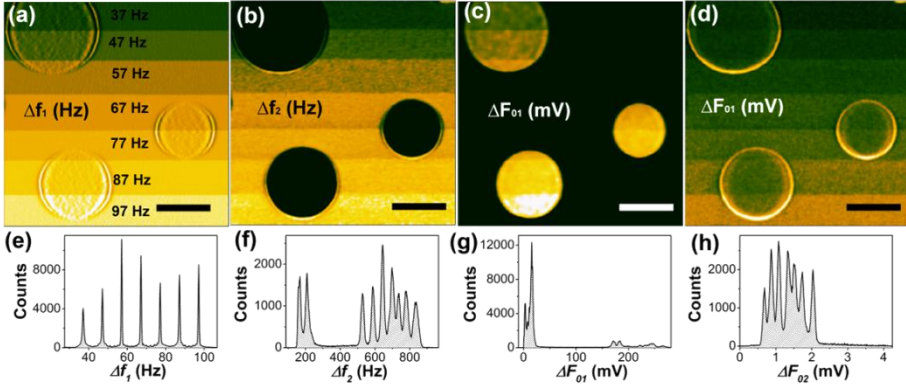
Figure 4.6. Experimental observables maps of a polymer (PS-LDPE) blend. (a) Map of $\Delta f_1(x,y)$. The image has been recorded by changing the main feedback approximately every 450 nm in the slow scanning direction (scale bar, 750 nm). (b) Map of $\Delta f_2(x,y)$. The changes in Δf_2 reflect both the changes in the elastic response of the blend and the changes of the main feedback (scale bar, 750 nm). (c) Map of $\Delta F_{01}(x,y)$. The map shows the changes in the driving force of mode 1 to compensate for the instantaneous changes in A_1 while imaging (scale bar, 750 nm). (d) Map of $\Delta F_{02}(x,y)$. The map shows the changes in the driving force of mode 2 to compensate for the instantaneous changes in A_2 while imaging (scale bar, 750 nm). (e) Histogram of Δf_1 obtained from (a). (f) Histogram of Δf_2 obtained from (b). (g) Histogram of $\Delta F_{01}(x,y)$ obtained from (c). (h) Histogram of $\Delta F_{02}(x,y)$ obtained from (d).

Those maps are taken simultaneously with the topography. The maps of the material properties (Figure 4.7 (a), (b), (c), (d)) are obtained by processing the data of Figure 4.6 ((a), (b), (c) and (d)) with the equations introduced above. The elastic modulus and viscosity coefficient maps show the existence of two regions that match the morphology of the polymer blend (Figure 4.7 (a), (b)).

The circular regions show a Young modulus of 168±30 MPa while the surrounding matrix has a mean value of 2.1±0.1 GPa (Figure 4.6 (e)). Those values coincide or are close to the expected values for the different regions of the blend (100 MPa and 2 GPa, respectively).

The viscosity (damping) maps taken at 1.8 MHz show two mean values, one centered at 11±4 Pa s (LDPE) and the other at 39±8 Pa s (PS) (Figure 4.7 (f)). The same maps taken at the frequency of the first mode (292214 Hz) give, respectively, 40 Pa s and 120 Pa s. The above nanomechanical measurements do not depend on the set-point values. This can be considered as an indication of the absence of artifacts in the measurements. The above maps have been acquired in less than 2 minutes.

The indentation map depends on the frequency set-point value because this controls the maximum force (peak force) exerted on the sample. It also depends on the local compliance of the sample. This is reflected in the corresponding histogram (Figure 4.7 (g)) where the observed peaks are grouped in two different regions: one corresponding to the PS and the other to the LDPE regions. In the relatively stiff regions (PS) the peaks are found between 2.5 and 5 nm while for the softer regions (LDPE) the peaks are scattered between 10 and 20 nm. These values are in good agreement with the results showed in Figure 4.5 in which the required indentation values for each material to obtain a constant value of the elastic modulus are shown. The peaks obtained in the LDPE regions are smaller because the area of the LDPE regions is smaller than the area of the PS.
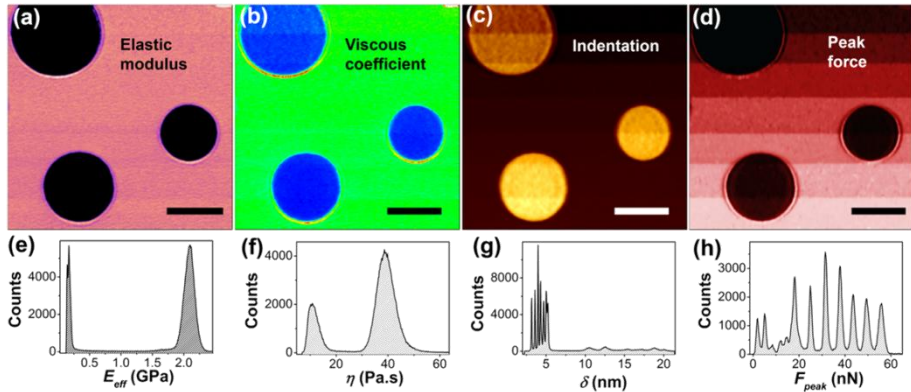
Figure 4.7. Nanomechanical maps of a polymer (PS-LDPE) blend.(a) Map of the elastic modulus across the surface. Two regions are observed. A softer region in the dark circles and a stiffer region in the rest of the surface. Those regions correspond, respectively, to the LDPE and PS (see histogram in (e)) (scale bar, 750 nm). (b) Map of the viscous coefficient. Two regions are observed. Lower damping (viscous) coefficients are found in the softer regions (LDPE) while the PS regions give higher damping coefficients (see histogram in (f)) (scale bar, 750 nm). (c) Map of the indentation. The indentation depends on both the elastic response and the set-point value (scale bar, 750 nm). (g) Map of the peak force (maximum force). It reproduces the trend observed in the indentation (scale bar, 750 nm). (e) Histogram of the E_{eff} values. The values do not depend on the feedback parameters. (f) Histogram of viscous coefficient. The values do not depend on the feedback parameters. (g) Histogram of the indentation. (h) Histogram of peak force values. The data has been recorded in 2 minutes.

The value of the peak force depends on both the compliance of the surface and the set-point frequency shift. Seven peak force values are found in the PS regions, ranging between 18 nN and 56 nN (Figure 4.7 (h)). In the LDPE regions we only distinguish five peaks with forces ranging between 2 nN and 14.5 nN.

Reconstruction of the topography

The AFM topography images cannot be considered as real topography especially while imaging soft matter [168, 169]. This is reflected in the dependence of the indentation on the set-point frequency shift (Figure 4.7 (c), (g)). Therefore, since by bimodal FM-FM AFM the indentation can be calculated, it is possible to reconstruct the real topography of polymer surfaces by combining the apparent topography with the indentation map.

The real topography of the PS-LDPE blend sample presented in Figures 4.6 and 4.7 has been reconstructed. Figures 4.8 (a) and (d) show the apparent AFM topography image and the cross-section taken along the line in (a). As can be observed, when the frequency set-point increases, the apparent height of the islands decreases. However, when the topography is reconstructed (see Figure 4.8 (c)-(f)) as the sum of the apparent height and the indentation (see Figure 4.8 (b)-(e)) we can see that the LDPE islands height remains constant with the force.
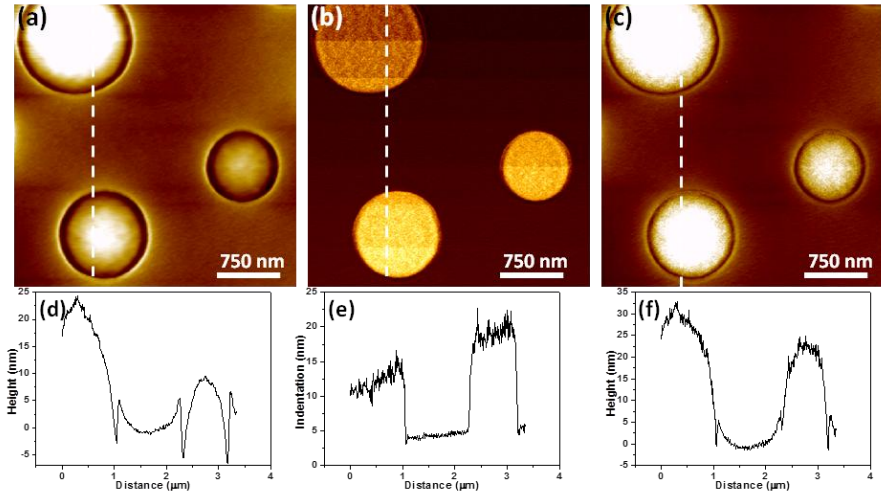
Figure 4.8. Real topography reconstruction. (a) Topography map taken in FM-FM bimodal AFM. (b) Map of the indentation. (c) Reconstructed topography image by adding (a) and (b) maps. (d) Cross section along the dashed line shown in (a). (e) Cross section along the dashed line shown in (b). (f) Cross section along the line in (c).

Sensitivity of bimodal FM-FM

To illustrate the capabilities of the technique to distinguish between different soft materials, two PDMS surfaces have been imaged, one characterized by a nominal Young modulus of 2.5 MPa and the other of 3.5 MPa. The measurements have been performed with the same tip and under the same experimental conditions.

Figure 4.9 shows the results obtained when applying the bimodal FM-FM method on the PDMS samples. Figure 4.9 (a) displays the AFM topography image of one of the PDMS samples. The AFM topography shows a granular structure with a grain diameter in the 10-25 nm range. The values of the E_{eff} and η are shown in the histograms (Figure 4.9 (b), (c)). The distributions show a mean value of 3.2±0.1 MPa and 2.1±0.1 MPa for the elastic modulus, and 7.8± 0.1 Pa s and 7.6± 0.1 Pa s (at 152997 Hz).

The ability of bimodal spectroscopy to distinguish between the two PDMS surfaces and to provide values of the elastic modulus very close to the nominal values (2.1±0.1 *versus* 2.5 MPa and 3.2±0.1 *versus* 3.5 MPa) gives an indication of the accuracy and sensitivity of the method. The damping coefficients measured at the frequency of the 1st mode (152860 Hz) give rather similar values, respectively, 7.6 Pa s for PDMS2 and 7.8 Pa s for PDMS1.
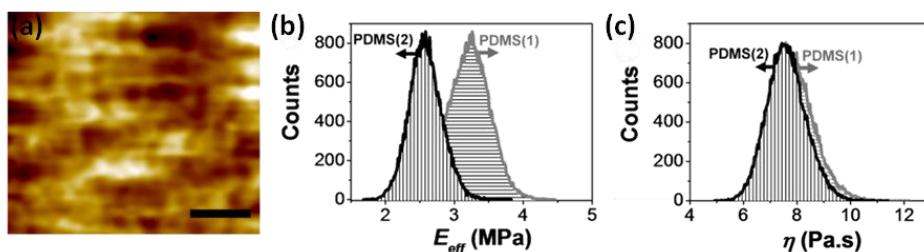

Figure 4.9. Bimodal FM-FM AFM on soft polymers. The same tip is used to map PDMS samples of different elastic moduli. (a) AFM topography image of a PDMS sample with a nominal E_{PDMS1} =3.5 MPa (scale bar, 50 nm). (b) Histogram of the elastic modulus. (c) Histogram of viscous coefficient.

High resolution

The present method does not interfere with the standard configuration of frequency modulation AFM, as a consequence the spatial resolution remains unaffected. To illustrate the spatial resolution, the surface of the block copolymer PS-b-PMMA thin film has been imaged. The diblock copolymer forms ordered structures alternating PS and PMMA domains. The elastic modulus and indentation maps (Figure 4.10 (a), (b)) show the presence of either flat or vertical PMMA cylinders (stiffer domains). The average diameter of the PMMA cylinders in both maps is of 17 nm. A cross-section taken from the indentation map (Figure 4.10 (c)) demonstrates a lateral resolution in the sub-17 nm range. Identical resolution is obtained in the viscous coefficients map.

The histogram obtained from Figure 4.10 (b) show the presence of two peaks (Figure 4.10 (d)). A dominant peak centered at 2.11 GPa corresponding to the PS regions and another shoulder-like peak centered at 2.6 GPa that comes from the PMMA regions. The contrast in the indentation and Young modulus maps is inverted. The indentation is smaller in the PMMA domains than in the PS regions, because the Young modulus of PMMA is higher than the one of PS.
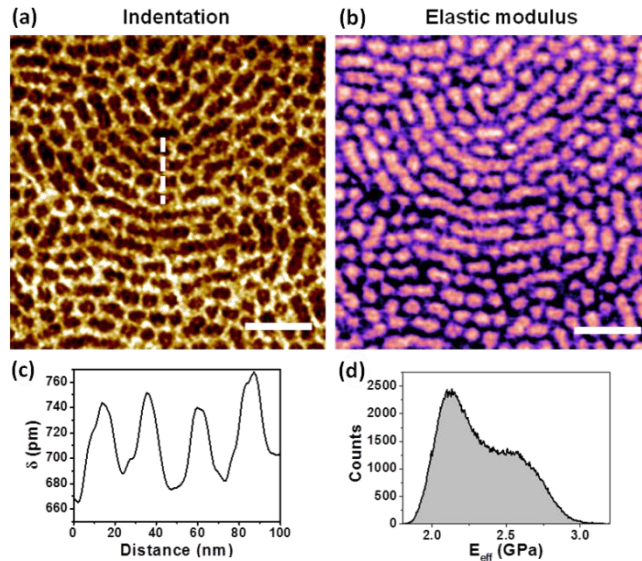

Figure 4.10. Spatial resolution in the elastic modulus map. (a) Indentation map in a block copolymer (PS-b-PMMA) thin film (scale bar, 100 nm). (b) Map of the elastic modulus of PS-b-PMMA (scale bar, 100 nm). (c) Cross-section along the dashed line shown in (a). (d) Histogram of the elastic modulus obtained from (b).

4.4.2 Experiments in Liquid

One of the goals of bimodal AFM operation is the quantitative mapping of material properties of proteins. For this purpose the mode must be applied in liquid medium.

In this section a proof of concept of the application of the FM-FM bimodal AFM method in liquid is shown. The results show that the application of the method in liquid is possible but the control of the FM-AFM loop has to be improved to obtain more accurate values.

First, the tip radius has been calibrated in distilled water on Teflon, which has a nominal elastic modulus of 0.9 GPa. The experimental values of the cantilever used in this experiment were $k_1 \approx 0.06$ N/m, $k_2 \approx 5.62$ N/m, $f_{01} \approx 25$ kHz, $f_{02} \approx 244$ kHz, $Q_1 \approx 2$, $Q_2 \approx 4$, and the free amplitudes used $A_{01} \approx 7.8$ nm and $A_{02} \approx 0.11$ nm. Figure 4.11 show the topography AFM image, the elastic modulus map and the histogram of the elastic modulus for the Teflon sample, respectively, for a tip radius of 3 nm. The image was taken at $\Delta f_1 \approx 700$ Hz. The distribution shows a mean value of 0.7±0.3 GPa very close to the nominal value of 0.9 GPa.
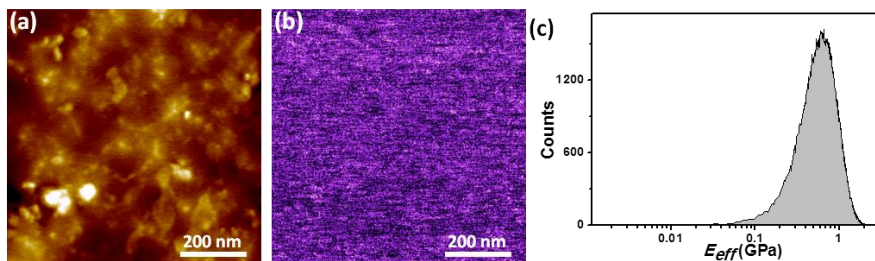

Figure 4.11. Nanomechanical map of Teflon in liquid. (a) Topography map in Teflon sample (b) Map of the elastic modulus of Teflon. (c) Histogram of the elastic modulus obtained from (b). The Teflon sample has been used to calibrate the tip radius for the measurements in liquid.

Once the tip radius has been calibrated, the IgM antibodies sample prepared on mica following the experimental preparation described in Chapter 2 is analyzed. Figure 4.12 shows the topography of an IgM antibody and the elastic modulus map along with the cross sections. The image was acquired by using $A_{01} \approx 5.8$ nm and $A_{02} \approx 0.3$ nm, and at a set-point of $\Delta f_1 \approx 600$ Hz.

The height of the antibody is near 6 nm which indicates that the measurement has been taken at a force of approximately 40 pN. The elastic modulus map shows a minimum value of 100 MPa. This value is one order of magnitude higher than the reported values in the literature. The value obtained for the mica is 1GPa. The elastic modulus of stiff materials measured with soft cantilevers is always underestimated [69, 82]. Even though the values are not accurate these results establish a proof of concept of the technique in liquid.

The control of the FM-AFM loop has to be improved, maybe with the use of stiffer cantilevers. The advantage of FM-AFM of using stiff cantilevers and small amplitudes to measure soft matter has already been shown [49, 135] and opens the door for the application of bimodal FM-FM AFM in liquids.
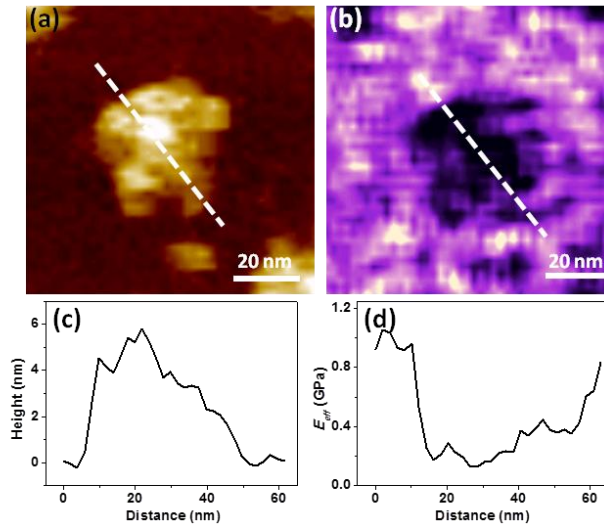

Figure 4.12. Nanomechanical map of an IgM antibody in Liquid. (a) Topography map. (b) Map of the elastic modulus. (c) Cross section along the dashed line shown in (a). (d) Cross section along the dashed line in (b).

4.5 Conclusions

The bimodal FM-FM AFM mode enables the measurement of several mechanical properties with nanoscale spatial resolution. Elastic and dissipative parameters of heterogeneous surfaces have been measured simultaneously with the apparent topography and the indentation. The method also provides the maximum value of the force exerted on each point of the surface.

Several features set this method apart from other force microscopy methods. This method requires four data points per pixel (frequency shift and dissipation of the first and second mode) to provide a nanomechanical description of the surface (stiffness, viscosity, deformation and peak force). The above feature speeds up data acquisition and minimizes the amount of data processed by the instrument. The same cantilever-tip system can be used to measured elastic properties covering a near four order of magnitude range. We have explored materials from 1 MPa to ~3 GPa.

The theory behind this method enables to determine beforehand the accuracy and/or suitability of a given measurement. In addition, the nanomechanical measurements are insensitive to the imaging parameters which prevent the cross-talk between topography and material properties. Finally, this nanomechanical spectroscopy is compatible with standard cantilevers and dynamic force microscopy configurations.

Chapter 5

Bimodal force microscopy in the AM-FM configuration

5.1 Introduction

One of the main goals of bimodal AFM is the nanomechanical mapping of soft matter in native environment. In light of the measurements performed in liquid in Chapter 4 with bimodal FM-FM AFM, there is a need for a better control of the FM-AFM operation in liquid. On one hand, the use of FM-AFM is not trivial due to the non-monotonic behaviour of the frequency shift with the distance, while on the other hand, AM-AFM is a robust imaging mode which uses the oscillation amplitude as the feedback parameter to follow the topography. Also, it is widely used and very accessible. This has motivated the development of bimodal AM-FM AFM mode.

In this chapter bimodal AM-FM AFM is applied to obtain the nanomechanical mapping of different surfaces in air and liquid. The theoretical expressions to calculate the elastic modulus and the indentation are introduced along with bimodal AM-FM simulations performed to validate those expressions. The same materials as the ones described in Chapter 4 are used to apply the method in air, and the same sensitivity and spatial resolution as in bimodal FM-FM AFM are obtained.

To apply the method in a liquid environment, samples with elastic moduli ranging from 10 MPa to 70 GPa are measured. Atomic and molecular resolutions are also achieved in the topography and elasticity maps.

5.1.1 Theoretical framework of AM-FM bimodal AFM

The theoretical model described here has been developed by Amir F. Payam and Ricardo Garcia [170]. In the bimodal AM-FM scheme the relationship between the observables and the nanomechanical properties is derived through a series of intermediate steps. First, some approximations are made for the first mode, which works in AM-AFM.

Considering Hertz model and that the oscillation amplitude is considerably larger than the indentation of the tip into the sample, the closest tip-sample distance can be calculated as follows [171]:

$$d_m = a_0 - \delta = a_0 - \sqrt{\frac{k_1}{Q_1 E_{eff}}} \sqrt{\frac{2A_1\left(A_{01}^2 - A_1^2\right)}{R}} \tag{5.1}$$

where d_m, is the closest tip-sample distance, k_1 is the first mode spring constant, Q_1 is the first mode quality factor, E_{eff} is the effective Young modulus of the interface, A_{01} is the first mode free amplitude, A_1 is the first mode working amplitude and R is the tip radius.

From Equation 5.1, the indentation, δ, can be expressed as,

$$\delta = \sqrt{\frac{k_1\sqrt{2A_1\left(A_{01}^2 - A_1^2\right)}}{Q_1 E_{eff} \sqrt{R}}} \tag{5.2}$$

And finally the effective Young's modulus can be obtained by

$$E_{eff} = \frac{k_1 \sqrt{2A_1\left(A_{01}^2 - A_1^2\right)}}{Q_1 \delta^2 \sqrt{R}} \tag{5.3}$$

For the second mode, Equation 4.10 is considered,

$$\Delta f_2(d_m) = \sqrt{\frac{R}{8A_1}} \frac{f_{02}}{k_2} E_{eff}\delta = \beta_2 E_{eff}\delta \tag{5.4}$$

The two main hypotheses to deduce Equation 5.4 are: (a) A_1 is larger than the typical length scale of the interaction force and (b) A_2 should satisfy

$$A_2 << 2\left|\frac{F_{ts}''\ (z_1(t))}{F_{ts}'''\ (z_1(t))}\right| \tag{5.5}$$

Equations 5.3 and 5.4 have two unknowns. By combining both equations we find δ and E_{eff} related to the experimental observables,

$$\delta = \frac{f_{02}}{\Delta f_{02}} \frac{k_1}{2k_2} \frac{\sqrt{A_{01}^2 - A_1^2}}{Q_1} \tag{5.6}$$

$$E_{eff} = \left(\frac{\Delta f_{02}}{f_{02}}\right)^2 \frac{k_2^2}{k_1} \frac{4\sqrt{2}Q_1}{\sqrt{R}} \frac{\sqrt{A_1}}{\sqrt{A_{01}^2 - A_1^2}} \tag{5.7}$$

The behavior of the bimodal AM-FM configuration and the validity of Equations 5.6 and 5.7 were simulated using numerical simulations. The numerical simulations were carried out using a fourth-order Runge-Kutta algorithm and simulating an automatic-gain controller (AGC) and a PLL by other member of the Forcetool group (Carlos A. Amo). The simulations were performed with the typical operational parameters.

For air, the values used for the resonance frequencies, force constants, quality factors and free amplitudes of the first mode and second mode were $f_{01}=$ 330 kHz; $f_{02}=$ 2.07 MHz; $k_1=$ 40 N/m; $k_2=$ 1600 N/m; $Q_1=$ 300; $Q_2=$ 500; $A_{01}=$ 20 nm; $A_{02}=$ 0.5 nm. For liquid, the values used for the resonance frequencies; force constants, quality factors and free amplitudes of the first mode and second mode were $f_{01}=$ 31 kHz; $f_{02}=$ 263 kHz; $k_1=$ 0.1 N/m; $k_2=$ 2 N/m; $Q_1=$ 2; $Q_2=$ 4; $A_{01}=$ 5 nm; $A_{02}=$ 0.2 nm.
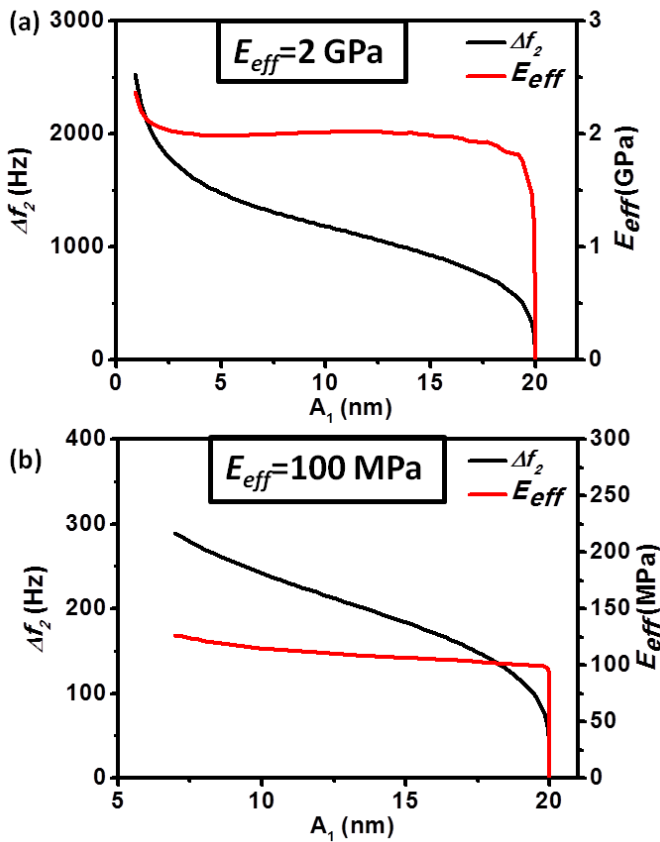
Figure 5.1. Simulated second mode frequency shift and calculated Young modulus in air, $Q_1=$ 300, with respect to the set-point first mode amplitude, A_1. (a) $E_{eff}=$ 2 GPa. (b) $E_{eff}=$ 100 MPa.

Figure 5.1 shows the results of the simulations for the air operational parameters. The black lines correspond to the $\mathit{\Delta f_2}$ simulated values as a function of the first mode working amplitude, A_1, plotted on the left side of the graph. On the other hand, the red lines depict the E_{eff} obtained by using Equation 5.7, plotted on the right side of the graph. Figure 5.1 (a) depicts the values for a sample characterized by $E_{eff} = 2$ GPa. The simulation shows that for a large range of working amplitudes the reconstructed value is in good agreement with the simulated one. For set-point amplitudes, $A_{sp}=A_1/A_{01}$, lower than 0.25, the reconstructed value increases and deviates from the correct value. Figure 5.1 (b) shows the simulated second mode frequency shift and calculated Young modulus for a sample characterized by $E_{eff} = 100$ MPa. In this case, the value deviates for set-point amplitudes lower than 0.5. As mentioned above, the assumptions used to approximate Equations 5.1 and 5.4 are that the first mode amplitude, A_1, must be higher than the length scale of the interaction force. As the first mode amplitude decreases, the indentation increases, making the first mode amplitude comparable to the indentation. For low set-point amplitudes the criteria is not met and the value deviates from the correct one.
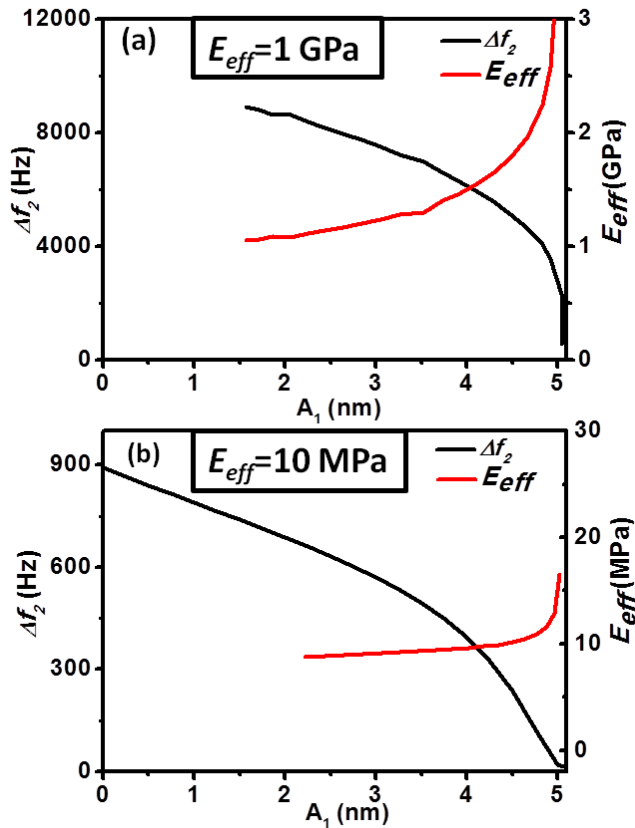
Figure 5.2. Simulated second mode frequency shift and calculated Young modulus in liquid, $Q_1 = 2$, with respect to the set-point first mode amplitude, A_1. (a) $E_{eff} = 1$ GPa. (b) $E_{eff} = 10$ MPa.

Figure 5.2 shows the results of the simulations for the liquid operational parameters (see page 108). The black lines correspond to the Δf_2 simulated values as a function of the first mode working amplitude, A_1, plotted on the left side of the graph. On the other hand, the red lines depict the E_{eff} obtained by using Equation 5.7, plotted in the right side of the graph. Figure 5.2 (a) shows the values for a sample characterized by $E_{eff} = 1$ GPa and Figure 5.2 (b) for a sample characterized by $E_{eff} = 10$ MPa.

The behavior for liquids is the same as in Figure 5.1, as the indentation increases the reconstructed value deviates from the simulated E_{eff}. The simulations show the validity of Equations 5.6 and 5.7 to calculate the nanomechanical properties of the sample. The assumptions are not fulfilled for set-point amplitudes, $A_{sp}=A_1/A_{01}$, lower than 0.40 so, for the experimental implementation of the technique, these set-point amplitudes will be avoided.

5.2 Experimental setup

Figure 5.3 shows the experimental setup for bimodal AM-FM AFM. In this bimodal operation setup the first eigenmode is operated in amplitude modulation and the second eigenmode is operated in frequency modulation. The resonance frequency of the first flexural mode f_{01} is kept fixed during imaging while the oscillation amplitude, A_1, is used as the feedback parameter to track the topography of the sample. In the second mode the changes of the resonance frequency are recorded while imaging and the oscillation amplitude is kept constant ($A_2 =$ constant). The changes in the frequency shift are followed by keeping the phase shift locked at 90º with a PLL.

This bimodal scheme has to be carried out by following the same conditions as explained in Chapter 4. For the quantitative nanomechanical mapping, the requirements of the derivation of the analytical expressions require the amplitude of the first mode A_1 to be more than one order of magnitude larger than the amplitude of the second mode.
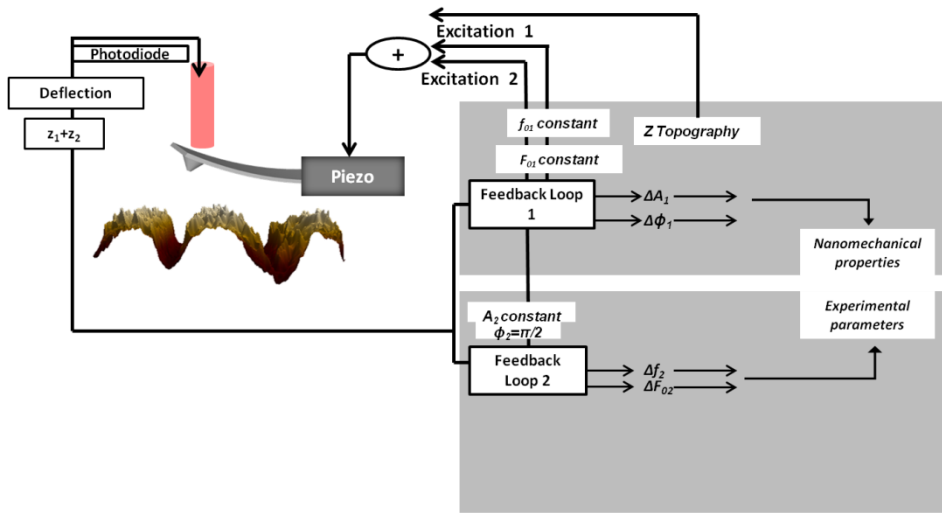
Figure 5.3. Experimental setup of AM-FM bimodal AFM. Two feedback loops keep the second mode amplitude constant and the second mode phase-shift at 90º as the cantilever scans the surface. The first mode operates in AM-AFM with the amplitude as feedback parameter to track the topography. Analytical relationships in Equations 5.6 and 5.7, enable the conversion of the observables data into quantitative maps.

The bimodal AFM experimental setup has been implemented in a commercial AFM hardware (Cypher, Asylum Research) using the IgorPro software and with the same user interface as presented in Chapter 4.

The calibration of the force constant has been carried out following the steps explained in Chapter 4 section 4.4. The tip radius estimation has been done either by using bimodal FM-FM tip radius calibration method (Chapter 4 section 4.4.1) or by looking at the lateral resolution achieved in the topography image.

Sample preparation

The bimodal AM-FM AFM method was applied to different samples in air and liquid. The samples used for the measurements in air were the same polymers as presented in Chapter 4, the PS-LPDE blend and the PS-b-PMMA block copolymer. For the measurements in liquid, three different samples were used: 1) the native purple membrane (PM) from *Halobacterium salinarum*. 2) Muscovite mica and 3) the Cerium Rare-earth Polymeric Framework 8 (Ce-RPF-8), an electric conducting Metal Organic Framework (MOF) synthesized by Dr. Felipe Gándara (ICMM-CSIC, Spain) [172].

Here, a description of the PM sample preparation is presented. PM from *Halobacterium salinarum* was provided by Dr. Ignacio Casuso (Universite Aix-Marseille, France). PM patches were deposited on freshly cleaved mica. Two different buffers were used, one for the sample deposition and the other one for imaging. The deposition buffer contains divalent cations to enhance the PM deposition on the mica surface (10 mM Tris-HCl, 150 mM KCl, 25 mM $MgCl_2$ pH 7.2). 15 µl of deposition buffer and 1 µl of PM solution were mixed in an eppendorf. Then, the solution was deposited on a circular mica of 1cm in diameter for 15 minutes. Finally, it was rinsed with imaging buffer (10 mM Tris-HCl, 150 mM KCl pH 7.2).

For the measurements on the MOF, the crystals were inmobilized on Silicon substrate. A mixture of polydimethylsiloxane (PDMS) (Sylgard 184, Sigma Aldrich) curing agent, PDMS elastomer base and hexane (Scharlau, Scharlab, S.L.), with proportions of 1:10:1000 (by weight) was spin coated on Silicon substrates at 5000 rpm for 60 s. The MOF crystals were then deposited on the PDMS and cured on a hot plate at 80 °C for 40 minutes. After the curing, an ultrasonic treatment of five seconds in distilled water was carried out in order to remove weakly attached crystals.

5.3 Experimental results

In this section the experimental results regarding the verification of the validity of Equations 5.6 and 5.7 to quantify nanomechanical properties and the bimodal AM-FM operation in liquid will be shown. This section is divided in two subsections as follows: first, the validity of the method in air will be discussed and second, the validity of the method in liquid showing molecular resolution and atomic resolution will be shown.

All the AFM data showed in the next section has been acquired at a scan frequency for the fast x axis in the 2 to 7 Hz range. The cantilevers used and the values applied for the first and second amplitudes will be mentioned in their corresponding subsections.

5.3.1 Experiments in air

In order to check the validity of the method in air, the PS-LDPE blend and the PS-b-PMMA block copolymer were measured. These samples illustrate two main points, the capability of the method to provide nanomechanical properties of samples ranging three orders of magnitude in E_{eff} with the same cantilever and the possibility to obtain quantitative high resolution images in air.

Figure 5.4 summarizes the results for both materials. Figures 5.4 (a) and (b) show the block copolymer and the PS-LDPE elastic modulus map obtained by applying Equation 5.7. Figures 5.4 (c) and (d) show the cross-sections along the dash lines in (a) and (b) along with the cross-sections taken from the indentation maps obtained by applying Equation 5.6. Indentation and elasticity show opposite behaviours, the higher the indentation the softer the material. The E_{eff} cross-section of Figure 5.4 (c) shows the presence of two dominant values, one at 2.2 GPa corresponding to the PS regions and another at 2.8 GPa that comes from the PMMA regions.

The average diameter of the PMMA cylinders is of 17 nm. The sensitivity to distinguish between both materials demonstrates the lateral resolution of the technique in the sub-17 nm range. The E_{eff} cross-section of Figure 5.4 (d) shows a Young modulus of 80 MPa for the circular regions while the surrounding matrix has a mean value of 2.1 GPa. Those values are in good agreement with the expected values for this material (100 MPa and 2 GPa, respectively).
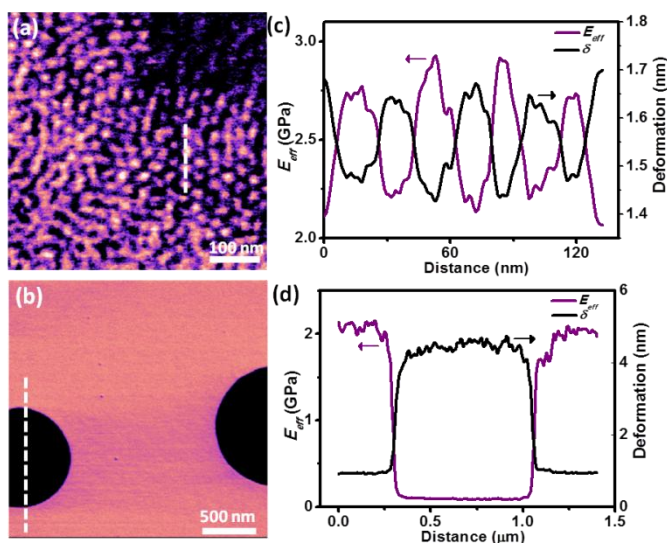

Figure 5.4. Map of the elastic modulus of the PS-LDPE blend and the PS-b-PMMA block copolymer. (a) Map of the elastic modulus of PS-b-PMMA. (b) Map of the elastic modulus of PS-LDPE blend. (c) Cross-section along the dashed line shown in (a) and in the indentation map. (d) Cross-section along the dashed line shown in (b) and in the indentation map.

5.3.2 Experiments in liquid

As mentioned in Chapter 4, one of the main goals of bimodal operation is the quantitative mapping of proteins in liquid environment. Few methods are able to provide quantitative mapping of materials in air, but only three of them have been applied to liquid environment:

PeakForce tapping mode [123, 173], torsional harmonics AFM [82] and bimodal FM-AM AFM [69]. PeakForce and torsional harmonics were applied to quantify the nanomechanical properties of PM and showed quantitative mapping with lateral resolution of 1 nm. Bimodal FM-AM AFM was applied to measure a single protein, the IgM antibody, and successfully obtain the nanomechanical map, but the main drawback of the technique is the need of a correction factor, C, determined by fitting force curves done at the beginning or the end of the experiment. In this section we will apply the bimodal AM-FM method in liquid, first, on the PM to check the validity of the method and second, to go a step further, the lateral resolution of the method will be shown on muscovite mica and MOF crystals at atomic level.

Bimodal AM-FM AFM on native membranes

PM from *Halobacterium salinarum* is a native membrane formed of lipids and the bacteriorhodopsin (BR) protein. BR protein is a light-driven proton-pump. It undergoes conformational changes to facilitate the proton path across the cellular membrane. PM is a very well-known sample in AFM studies since it is commercially available, robust and stable and it has become a reference sample for molecular resolution experiments [28, 174].

PM patches were imaged with AC-40TS (Olympus) cantilevers characterized by f_{01}=26.4 kHz, f_{02}=225.5 kHz, k_1= 79.83 pN/nm, k_2= 4.45N/m in liquid. Figure 5.5 (a) shows the topography AFM image of a PM patch exposing the cytoplasmic (CP) and the extracellular (EC) side. The image was taken at A_{01}= 4.4 nm, A_{sp}= 0.9 and A_{02}=0.35nm. The identification of the cytoplasmic and extracellular sides is performed from the apparent height measured. Given the fact that the extracellular side is more negatively charged than the cytoplasmic side, it repeals more the AFM tip and thus, the extracellular side protrudes more.

Additional ways to distinguish the membrane sides have been previously proposed [175]: 1) The cytoplasmic side exposes random protrusions while the extracellular side appears smooth, as observed in Figure 5.5 (a), and 2) The phase shift channel in AM-AFM is darker on the extracellular side than on the cytoplasmic side. The cytoplasmic side exhibits a height of 7.0 ± 0.2 nm and the extracellular side of 8.1 ± 0.2 nm (see Figure 5.5 (c)). These values are in good agreement with the reported values in the literature for measurements in buffer at an electrolyte concentration of 150 mM of KCl [173]. The unperturbed native membrane exhibits a thickness of 5.8 nm however, due to the DLVO forces, a height gain of 2-3 nm is produced (See Chapter 2 section 2.1).
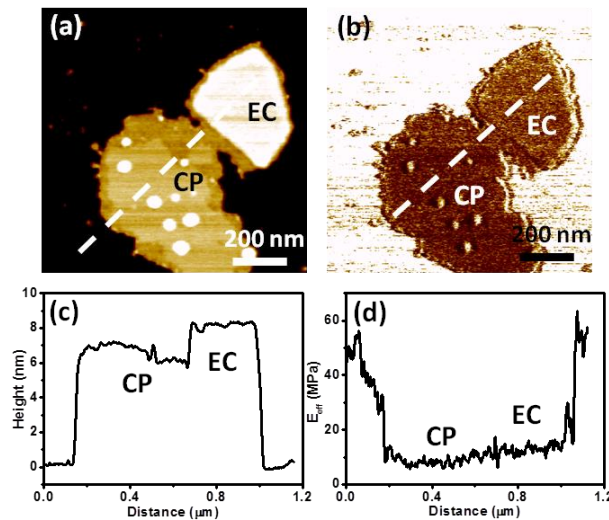

Figure 5.5. Purple membrane (PM) observed in buffer solution using AM-FM bimodal AFM. (a) Topography of a patch of PM exhibiting the cytoplasmic and extracellular surface. (b) Elastic modulus map. (c) Cross-section along the dashed line shown in (a). (d) Cross-section along the dashed line shown in (b).

Figure 5.5 (b) corresponds to the elastic modulus AFM image and Figure 5.5 (d) shows the cross-section taken along the dashed line in (b). The cytoplasmic side exhibits a Young modulus of 8 MPa, slightly lower than the one for the extracellular side, 12 MPa. These values correlate well with the calculated values by PeakForce tapping mode (10 MPa both sides) [123, 173] and torsional harmonic cantilevers (7 MPa for the cytoplasmic side and 35 MPa for the extracellular side) [82]. The deformation value for the PM patch calculated by Equation 5.6 was 4 nm for the cytoplasmic side and 3 nm for the extracellular side.

As mentioned before, the PM is formed by only one protein, the BR protein, which organizes into trimers, surrounded by about 10 membrane lipids [176]. In Figure 5.5, the contribution of the protein and the lipids is unnoticeable. To get structural details of the protein substructures we have to go deeper and obtain high resolution images with lateral resolution of at least 1 nm. Figure 5.6 shows high resolution AFM images taken on the extracellular side of the patch showed in Figure 5.5. The topography image (Figure 5.6 (a)) shows the arrangement of the BR trimers in a hexagonal lattice of 6.2 nm constant. The inset depicts the three-fold symmetrized cross-correlation averaged topography. Figures 5.6 (b), (c) and (d) shows the elastic modulus channel, the deformation channel and the second mode driving amplitude channel (dissipation), respectively. The raw images are noisy and do not give as much information as the topography image; due to this reason a further image processing is necessary. This analysis was realized as follows: first, a cross-correlation was done for the topography image with one of the BR trimers. From the cross-correlation each individual BR trimer was located. Second, the coordinates of each BR trimer were merged with the elastic modulus, deformation and dissipation channels. Finally, each unit cell is superimposed, averaged and three-fold symmetrized to obtain the corresponding insets. The averaged value of the three-fold symmetrized cross-correlation average of the elastic modulus is 30 MPa. Lipids surrounding the BR trimers appear much softer than trimers.

This difference in elasticity between lipids and BR may explain the biological processes that the PM performs, for instance the compliant lipids would form the flexible structure for the rigid BR trimers to undergo the conformational changes necessary for the proton pumping. The result is in accordance with the reported values in the literature not only by AFM but also by elastic neutron scattering [119].

The indentation is in agreement with the elastic modulus, the higher values are 1.9 nm for the lipids and 1.7 nm for the BR trimers (Figure 5.6 (c)). The dissipation channel (see Figure 5.6 (d)) indicates that the dissipated energy is higher over the BR protrusion than over the lipids.
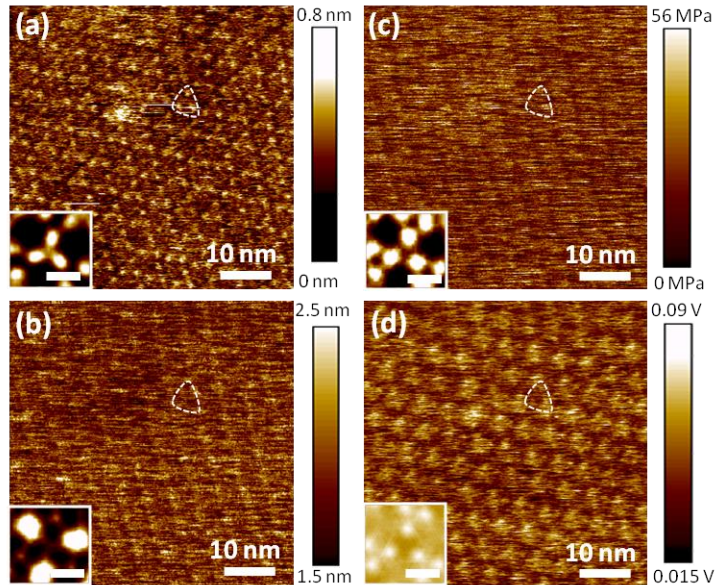

Figure 5.6. High resolution images by AM-FM bimodal AFM of the extracellular PM surface. (a) AFM topography image. (b) Deformation map. (c) Elastic modulus map. (d) Second mode driving amplitude channel (dissipation). Insets show three-fold symmetrized cross-correlation average of the BR trimer (scale bar, 4 nm).

High resolution images and maps allow us to distinguish elasticity changes within the three extracellular loops of the individual BR protein.

Figure 5.7 shows the cross-correlation averaging of the AFM topography image and the Young modulus map. The atomic structure is overlaid on the Young modulus map. Figure 5.7 (c) shows the Young modulus profiles of the interhelical loops of the BR extracellular surface. The most compliant loop is the B-C loop. The stiffness of BR obtained is approximately 0.2 N/m. This value of stiffness is comparable with the reported values of 0.33 N/m for the extracellular surface obtained by elastic neutron scattering [119].
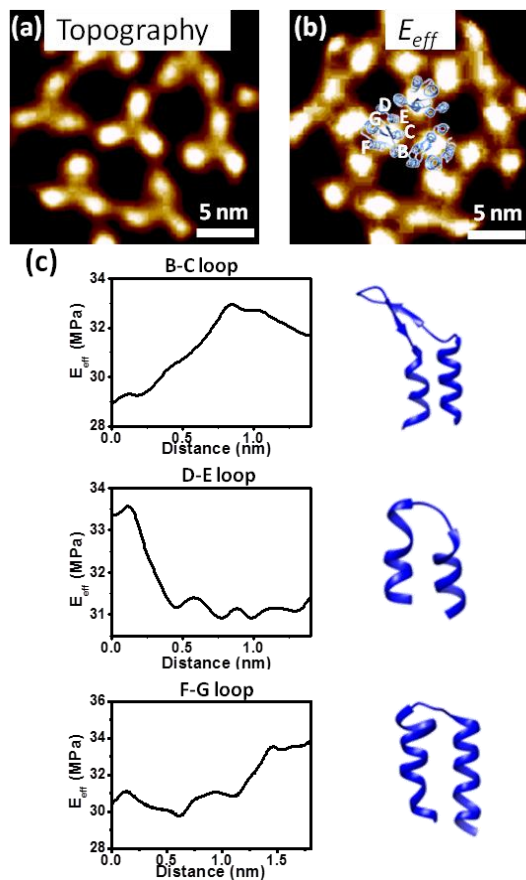

Figure 5.7. Three-fold symmetrized cross-correlation average of the topography channel (a) and Young modulus map (b) of the BR trimers. (c) Cross-sections of the Young modulus of the interhelical loops showed in the atomic structure of the BR protein of (b).

Bimodal AM-FM AFM on muscovite mica

Bimodal AM-FM AFM was also applied to obtain atomic-scale contrast on muscovite mica. The freshly cleaved mica was imaged in distilled water with a PPP-NCH (Nanosensors) cantilever characterized by f_{01}= 125 kHz, f_{02}= 870 kHz, k_1= 30 N/m, k_2= 1313 N/m in liquid.

Figure 5.8 shows the measurements performed at different free amplitudes of the first mode, A_{01}= 0.6 nm (Figure 5.8 (a)) and A_{01}=1.8 nm (Figure 5.8 (b)), and at $A_{sp}=A_1/A_{01}$= 0.6 on the mica surface. The second mode free amplitude was set to A_{02}= 0.14 nm. Figure 5.8 (a) depicts the topography channel and the second mode frequency channel, Δf_2 at A_{01}= 0.6 nm and A_{02}= 0.14 nm. In the topography channel atomic resolution can clearly be seen, however the Δf_2 channel shows a weaker atomic contrast. It is also worth noting that the tip changed during the image progress (bottom part of the image) and, although the contrast in topography was enhanced, the contrast in Δf_2 was deteriorated. This indicates a change in the tip-sample distance produced by a change in the tip apex.
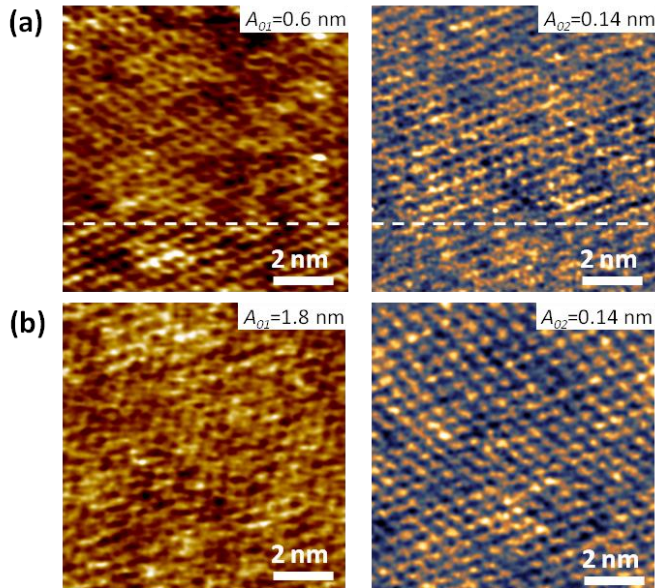
Figure 5.8. Atomic resolution images by AM-FM bimodal AFM on the mica surface. (a) Topography and second mode frequency shift channels taken at A_{01}= 0.6 nm and A_{02} =0.14 nm. (b) Topography and second mode frequency shift channels taken at A_{01}= 1.8 nm and A_{02} =0.14 nm.

Figure 5.8 (b) depicts the topography channel and the second mode frequency channel, Δf_2 at A_{01}= 1.8 nm and A_{02}= 0.14 nm. The Δf_2 channel displays atomic resolution; however, the topography channel is very noisy and shows a loss in resolution. This loss in resolution is caused by the increment in A_{01} and the subsequent appearance of anharmonicity in the tip dynamics due to the excitation of higher harmonics [177]. At small amplitudes the tip is oscillating in the solvation layers formed at the solid-liquid interface, but when the free amplitude increases the average tip-sample distance reduces and the tip temporarily touches the sample exciting higher harmonics of the resonance frequency. The enhancement in resolution in the Δf_2 channel may be triggered by the increment in A_{01}/A_{02} ratio as was explained in Chapter 4 but more experiments should be carried out.

The effective elastic modulus obtained for the mica in this experiments is $E_{eff} = 68 \pm 11$ GPa. To obtain the Young modulus of the mica, Equation 3.4 is applied. By using $v_t = v_s = 0.3$, $E_{mica} = 95$ GPa, which is in good correlation with the bulk value.

Bimodal AM-FM AFM on MOF crystal

Figure 5.9 displays the experimental results on the MOF crystal. The experiments were carried out with an Arrow-UHF (NanoWorld) cantilever. The experimental values for the cantilever were $f_{01} = 700$ kHz, $f_{02} = 2663$ kHz, $k_1 = 13$ N/m, $k_2 = 171$ N/m measured in liquid. The amplitudes used to obtain Figure 5.7 were $A_{01} = 1.1$ nm and $A_{02} = 0.12$ nm and at $A_{sp} = 0.6$.
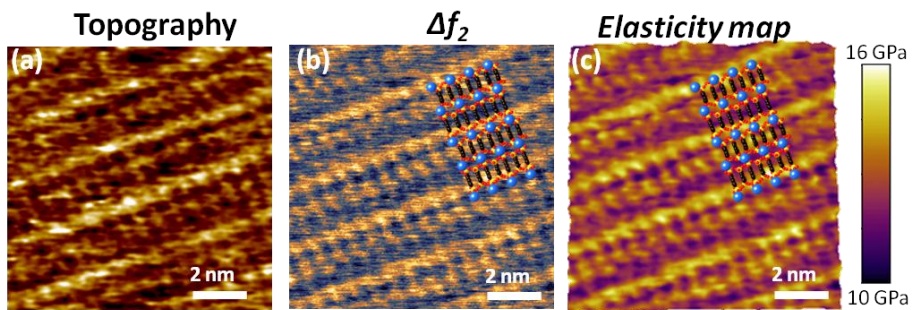
Figure 5.9. Atomic resolution images by AM-FM bimodal AFM on the MOF surface. (a) Topography AFM image. (b) Second mode frequency shift channel. (c) Elasticity map. The X-ray structure of the MOF is overlaid. The Ce, S, O and C atoms are represented as blue, yellow, red and black spheres.

The $\mathit{\Delta f_2}$ channel shows atomic resolution on the MOF crystal. It is possible to distinguish the position of individual Ce atoms in the rows as well as the carbon chains. The lattice is 7.01 Å x 21.7 Å and is in good agreement with the X-ray data.

The topography shows faint atomic contrast and it is related to the A_{01} used to take the measurement. As happened in Figure 5.8 (b), A_{01} much larger than the primary hydration layer leads to anharmonicity in the tip oscillation and the loss of atomic resolution. The elasticity map has been calculated and the effective Young modulus is $E_{eff} = 13\pm1$ GPa.

5.4 Conclusions

The bimodal AM-FM AFM mode has been described in this chapter. The method has been validated theoretically, through bimodal simulations, and experimentally, by measuring several samples in air and liquid environment. The method allows measuring the elastic modulus and the determination of several experimental parameters, such as the indentation or the peak force, simultaneously with the apparent topography.

The versatility of the method has enabled the measurement of the elastic properties of a wide range of materials, from biomolecules to polymers, to organic and inorganic materials in air and liquid with variations in the elastic modulus of near four orders of magnitude, from 1 MPa to 3 GPa. Also, the bimodal AM-FM AFM mode keeps all the benefits already gained in the bimodal FM-FM configuration presented in Chapter 4, such as nanoscale spatial resolution and fast data acquisition. The lateral resolution obtained on the biological systems is 1 nm and on the MOF is 0.5 nm. The atomic resolution achieved allows distinguishing the Ce atoms from the carbon chains. With the bimodal AM-FM configuration, the molecular and atomic resolution achieved in the nanomechanical maps in liquid medium is beyond the state-of-the-art of the AFM.

Conclusions

1. A study of the factors that control the applied force in the main operating modes, AM-AFM and FM-AFM in air and AM-AFM and Hybrid mode in liquid, for imaging biomolecules was performed. The study concluded that, at the same operational parameters such as free amplitude, scan speed or scan size, and with the same cantilever, in the repulsive regime AM-AFM applies higher forces than FM-AFM. The difference in applied force found between the dynamic modes could have implications on measurements in which the true height characterization of nanostructures, such as nanoparticles, biomolecules or proteins, is a key factor.

2. Theoretical expressions, valid in air, were deduced to quantify the applied force and the deformation in AFM images as a function of the operational parameters. The validity of these expressions was experimentally studied by considering the apparent height of single antibody pentamers.

3. The stress-strain curve of a single and isolated protein in physiological-like conditions was obtained. It is the first time that stress-strain curves are reported at the single molecule level. To determine the protein stress-strain curve, a force microscopy method was developed. The method has a force sensitivity of 5 pN and, lateral and vertical resolutions, respectively, of 2 and 0.1 nm. The stress-strain curve shows three distinctive regions. For low strains the protein's central region shows that the stress and strain are proportional (elastic regime). This region has an average Young modulus of 2.5 MPa.

For strains between 0.25 and 0.4, the data suggests a different elastic region where the stress is roughly proportional to the strain with a Young modulus of 9 MPa. Higher strains lead to generation of irreversible deformations (plastic regime). The existence of two different elastic regions is explained in terms of the complex structure of the antibody central region. With the stress-strain curve it is possible to explain why secreted proteins can experience multiple collisions with other biomolecules without any loss of biological functionality. The determination of the stress-strain curve also illustrates how standard macroscopic measurements (stress-strain curves) can be carried out at the nanoscale level.

4.   In bimodal AFM, the contrast provided by the second mode channels depends on the operational conditions of both the first and the second mode. An enhancement of the contrast in the second mode channels is observed when the amplitude ratio is maximized by either increasing the first mode amplitude or decreasing the second mode amplitude. A minimum value of the second mode free amplitude is a fundamental requirement to obtain contrast in the second mode channels.

5.   Bimodal AFM with FM-FM and AM-FM configurations was developed and implemented in a commercial microscope. Several features set this method apart from other force microscopy methods. This method requires four data points per pixel (frequency shift and dissipation or amplitude and phase of the first and second mode) to provide a nanomechanical description of the surface (stiffness, viscosity, deformation and peak force). The above feature speeds up data acquisition and minimizes the amount of data processed by the instrument. The same cantilever-tip system can be used to measure elastic properties covering a near four orders of magnitude range.

We have explored materials from 1 MPa to ~3 GPa. In addition, bimodal AFM can be operated at very small forces (sub-50 pN).

6.   Bimodal AFM provides a method to reconstruct the real topography of a surface sample. The determination of the indentation allows the reconstruction of the real topography by combining the apparent topography with the indentation map.

7.   A protocol that enables to check beforehand the accuracy and/or suitability of a given measurement was implemented in bimodal FM-FM AFM. Besides, this protocol can also be used to estimate the tip radius. The tip radius is a fundamental parameter for the determination of the mechanical properties.

8.   The bimodal AM-FM AFM mode was applied in liquid and has enabled the measurement of the elastic properties of polymers, lipid membranes, mica and MOF samples. With the bimodal AM-FM configuration, the molecular and atomic resolution achieved in the nanomechanical maps in liquid medium is beyond the state-of-the-art of the AFM. The lateral resolution obtained on the biological systems is 1 nm and on the MOF is 0.5 nm. The atomic resolution achieved allows distinguishing the Ce atoms from the carbon chains.

Conclusiones

1. Se ha realizado un estudio de los factores que controlan la fuerza aplicada en los principales modos dinámicos de operación de AFM, amplitud modulada (AM) y frecuencia modulada (FM) en aire y AM y el modo Híbrido en líquido para medidas en biomoléculas. Se concluyó que para los mismos parámetros operacionales, como la amplitud libre, la velocidad de escaneo y el tamaño de la imagen, y el mismo cantiléver, AM-AFM aplica fuerzas más altas que FM-AFM en el régimen repulsivo. Esta diferencia en fuerza aplicada puede tener implicaciones importantes en la caracterización de la altura real de nanoestructuras, nanoparticulas biomoléculas o proteínas.

2. Se han deducido expresiones teóricas, validas en aire, para cuantificar la fuerza aplicada en imágenes de AFM en función de los parámetros operaciones. La validez de las expresiones fue estudiada experimentalmente sobre anticuerpos de tipo Inmunoglobulina M (IgM).

3. Se ha obtenido la curva de tensión-deformación de un anticuerpo IgM en condiciones fisiológicas. Para obtener esta curva se ha desarrollado un procedimiento por el cual se consigue una sensibilidad en la fuerza aplicada de 5 pN y resoluciones laterales y verticales de 2 y 0.1 nm, respectivamente. La curva de tensión-deformación del anticuerpo IgM muestra tres regiones distintas. Para bajas deformaciones, entre 0 y 0.25, la proteína muestra una respuesta lineal, régimen elástico, con un modulo de Young de 2.5 MPa. Para deformaciones entre 0.25 y 0.4, se observa un comportamiento distinto pero aún en el región elástica. Esta región se caracteriza por un modulo de elástico de 9 MPa.

Deformaciones más altas de 0.4 producen deformaciones irreversibles, indicando que la proteína ha alcanzado el régimen plástico. La existencia de las dos regiones elásticas, con 2.5 MPa y 9 MPa, se puede explicar debido a la compleja estructura de la parte central del anticuerpo que muestra dos dominios diferentes, dominios Cμ4 y Cμ3. Con la determinación de las curvas de tensión-deformación es posible explicar cómo las proteínas segregadas pueden experimentar colisiones con otros componentes sin perder su función biológica. Esta es la primera vez que se determina la curva de tensión-deformación a nivel molecular.

4. Se ha estudiado también el contraste en los canales del segundo modo en excitación bimodal. Se estudiaron las condiciones experimentales del primer y segundo modo que producen una mejora en el contraste. Se determinó que cuando la razón entre las amplitudes del primer modo y del segundo modo se maximizaba, el contraste obtenido aumentaba, siempre y cuando hubiese un mínimo de excitación en el segundo modo.

5. Las configuraciones bimodales FM-FM y AM-FM han sido desarrolladas e implementadas en un microscopio comercial. Los métodos bimodales presentan múltiples ventajas que las separan de otros métodos de AFM. Estas configuraciones disminuyen el tiempo de adquisición de datos debido a que sólo son necesarios 4 puntos por pixel para el cálculo de las propiedades nanomecánicas de la muestra (Modulo elástico y viscosidad). Además con estas configuraciones es posible el cálculo de otros parámetros operaciones como la fuerza aplicada o la deformación. Se han aplicado los dos métodos en aire sobre polímeros con módulos de Young entre 2 MPa y 3 GPa.

6. Se ha mostrado que la reconstrucción de la topografía real de la muestra es posible en las configuraciones bimodales.

La determinación de la indentación proporciona la reconstrucción de la topografía real mediante la suma del canal de topografía y el de indentación.

7. La configuración bimodal FM-FM AFM proporciona también un método para revisar y asegurar la validez de los datos obtenidos. Mediante este método es posible también obtener el radio de la punta, que es un valor fundamental para la obtención de las propiedades mecánicas.

8. La configuración bimodal AM-FM AFM se aplicó en medio líquido sobre membranas lipídicas, mica y redes de materiales organometálicos. Se ha conseguido resolución molecular y atómica en los mapas de propiedades mecánicas. La resolución espacial conseguida sobre las membranas lipídicas es de 1 nm y sobre las redes de materiales organometálicos es de 0.5 nm. La resolución atómica conseguida permite distinguir los átomos pesados (Ce) de las cadenas de átomos ligeros (C-H). Estos resultados se encuentran en el estado del arte del AFM

References

[1] G. Binnig, C. Quate, C. Gerber, Atomic Force Microscope, Physical Review Letters, 56 (1986) 930-933.

[2] Y. Sugimoto, P. Pou, M. Abe, P. Jelinek, R. Perez, S. Morita, O. Custance, Chemical identification of individual surface atoms by atomic force microscopy, Nature, 446 (2007) 64-67.

[3] N. Kodera, D. Yamamoto, R. Ishikawa, T. Ando, Video imaging of walking myosin V by high-speed atomic force microscopy, Nature, 468 (2010) 72-76.

[4] M. Bentley, in, Space Research Institute http://blogs.esa.int/rosetta/2014/12/17/midas-and-its-first-dust-grain/.

[5] E. Betzig, G.H. Patterson, R. Sougrat, O.W. Lindwasser, S. Olenych, J.S. Bonifacino, M.W. Davidson, J. Lippincott-Schwartz, H.F. Hess, Imaging Intracellular Fluorescent Proteins at Nanometer Resolution, Science, 313 (2006) 1642-1645.

[6] A. Yildiz, J.N. Forkey, S.A. McKinney, T. Ha, Y.E. Goldman, P.R. Selvin, Myosin V Walks Hand-Over-Hand: Single Fluorophore Imaging with 1.5-nm Localization, Science, 300 (2003) 2061-2065.

[7] S.T. Hess, T.P.K. Girirajan, M.D. Mason, Ultra-High Resolution Imaging by Fluorescence Photoactivation Localization Microscopy, Biophysical Journal, 91 (2006) 4258-4272.

[8] G. Binnig, H. Rohrer, C. Gerber, E. Weibel, Tunneling through a controllable vacuum gap, Applied Physics Letters, 40 (1982) 178-180.

[9] G. Binnig, H. Rohrer, C. Gerber, E. Weibel, Surface Studies by Scanning Tunneling Microscopy, Physical Review Letters, 49 (1982) 57-61.

[10] P.K. Hansma, J.P. Cleveland, M. Radmacher, D.A. Walters, P.E. Hillner, M. Bezanilla, M. Fritz, D. Vie, H.G. Hansma, C.B. Prater, J. Massie, L. Fukunaga, J. Gurley, V. Elings, Tapping mode atomic force microscopy in liquids, Applied Physics Letters, 64 (1994) 1738-1740.

[11] C.A.J. Putman, K.O. Van der Werf, B.G. De Grooth, N.F. Van Hulst, J. Greve, Tapping mode atomic force microscopy in liquid, Applied Physics Letters, 64 (1994) 2454-2456.

[12] W. Han, S.M. Lindsay, T. Jing, A magnetically driven oscillating probe microscope for operation in liquids, Applied Physics Letters, 69 (1996) 4111-4113.

[13] D. Ramos, J. Tamayo, J. Mertens, M. Calleja, Photothermal excitation of microcantilevers in liquids, Journal of Applied Physics, 99 (2006) 124904.

[14] G. Meyer, N.M. Amer, Novel optical approach to atomic force microscopy, Applied Physics Letters, 53 (1988) 1045-1047.

[15] R. Erlandsson, G.M. McClelland, C.M. Mate, S. Chiang, Atomic force microscopy using optical interferometry, Journal of Vacuum Science & Technology A, 6 (1988) 266-270.

[16] D. Rugar, H.J. Mamin, P. Guethner, Improved fiber-optic interferometer for atomic force microscopy, Applied Physics Letters, 55 (1989) 2588-2590.

[17] B.W. Hoogenboom, P.L.T.M. Frederix, J.L. Yang, S. Martin, Y. Pellmont, M. Steinacher, S. Zäch, E. Langenbach, H.-J. Heimbeck, A. Engel, H.J. Hug, A Fabry–Perot interferometer for micrometer-sized cantilevers, Applied Physics Letters, 86 (2005) 074101.

[18] T.E. Schäffer, H. Fuchs, Optimized detection of normal vibration modes of atomic force microscope cantilevers with the optical beam deflection method, Journal of Applied Physics, 97 (2005) 083524.

[19] R. García, Amplitude modulation atomic force microscopy, John Wiley & Sons, 2011.

[20] J.E. Sader, I. Larson, P. Mulvaney, L.R. White, Method for the calibration of atomic force microscope cantilevers, Review of Scientific Instruments, 66 (1995) 3789-3798.

[21] J.E. Sader, J.W.M. Chon, P. Mulvaney, Calibration of rectangular atomic force microscope cantilevers, Review of Scientific Instruments, 70 (1999) 3967-3969.

[22] J.E. Sader, J.A. Sanelli, B.D. Adamson, J.P. Monty, X. Wei, S.A. Crawford, J.R. Friend, I. Marusic, P. Mulvaney, E.J. Bieske, Spring constant calibration of atomic force microscope cantilevers of arbitrary shape, Review of Scientific Instruments, 83 (2012) 103705.

[23] J.L. Hutter, J. Bechhoefer, Calibration of atomic-force microscope tips, Review of Scientific Instruments, 64 (1993) 1868-1873.

[24] H.J. Butt, M. Jaschke, Calculation of thermal noise in atomic force microscopy, Nanotechnology, 6 (1995) 1–7

[25] C.M. Mate, G.M. McClelland, R. Erlandsson, S. Chiang, Atomic-scale friction of a tungsten tip on a graphite surface, Physical Review Letters, 59 (1987) 1942-1945.

[26] V. Moy, E. Florin, H. Gaub, Intermolecular forces and energies between ligands and receptors, Science, 266 (1994) 257-259.

[27] P. Steiner, E. Gnecco, F. Krok, J. Budzioch, L. Walczak, J. Konior, M. Szymonski, E. Meyer, Atomic-Scale Friction on Stepped Surfaces of Ionic Crystals, Physical Review Letters, 106 (2011) 186104.

[28] D.J. Müller, F.A. Schabert, G. Büldt, A. Engel, Imaging purple membranes in aqueous solutions at sub-nanometer resolution by atomic force microscopy, Biophysical Journal, 68 (1995) 1681-1686.

[29] Y. Martin, C.C. Williams, H.K. Wickramasinghe, Atomic force microscope–force mapping and profiling on a sub 100-Å scale, Journal of Applied Physics, 61 (1987) 4723-4729.

[30] R. García, R. Pérez, Dynamic atomic force microscopy methods, Surface Science Reports, 47 (2002) 197-301.

[31] A. San Paulo, R. García, High-Resolution Imaging of Antibodies by Tapping-Mode Atomic Force Microscopy: Attractive and Repulsive Tip-Sample Interaction Regimes, Biophysical Journal, 78 (2000) 1599-1605.

[32] H.V. Guzman, A.P. Perrino, R. Garcia, Peak Forces in High-Resolution Imaging of Soft Matter in Liquid, ACS Nano, 7 (2013) 3198-3204.

[33] K. Voitchovsky, J.J. Kuna, S.A. Contera, E. Tosatti, F. Stellacci, Direct mapping of the solid-liquid adhesion energy with subnanometre resolution, Nature Nanotechnology, 5 (2010) 401-405.

[34] S.A. Contera, K. Voitchovsky, J.F. Ryan, Controlled ionic condensation at the surface of a native extremophilemembrane, Nanoscale, 2 (2010) 222-229.

[35] M.B. Viani, T.E. Schäffer, G.T. Paloczi, L.I. Pietrasanta, B.L. Smith, J.B. Thompson, M. Richter, M. Rief, H.E. Gaub, K.W. Plaxco, A.N. Cleland, H.G. Hansma, P.K. Hansma, Fast imaging and fast force spectroscopy of single biopolymers with a new atomic force microscope designed for small cantilevers, Review of Scientific Instruments, 70 (1999) 4300-4303.

[36] M. Radmacher, M. Fritz, H.G. Hansma, P.K. Hansma, Direct observation of enzyme activity with the atomic force microscope, Science, 265 (1994) 1577-1579.

[37] T. Ando, T. Uchihashi, T. Fukuma, High-speed atomic force microscopy for nano-visualization of dynamic biomolecular processes, Progress in Surface Science, 83 (2008) 337-437.

[38] A. Toshio, High-speed atomic force microscopy coming of age, Nanotechnology, 23 (2012) 062001.

[39] M. Shibata, H. Yamashita, T. Uchihashi, H. Kandori, T. Ando, High-speed atomic force microscopy shows dynamic molecular processes in photoactivated bacteriorhodopsin, Nature Nanotechnology, 5 (2010) 208-212.

[40] T.R. Albrecht, P. Grütter, D. Horne, D. Rugar, Frequency modulation detection using high-Q cantilevers for enhanced force microscope sensitivity, Journal of Applied Physics, 69 (1991) 668-673.

[41] H. Ueyama, Y. Sugawara, S. Morita, Stable operation mode for dynamic noncontact atomic force microscopy, Applied Physics A, 66 (1998) S295-S297.

[42] F.J. Giessibl, Advances in atomic force microscopy, Reviews of modern physics, 75 (2003) 949.

[43] F.J. Giessibl, Atomic Resolution of the Silicon (111)-(7x7) Surface by Atomic Force Microscopy, Science, 267 (1995) 68-71.

[44] F.J. Giessibl, Atomic resolution on Si(111)-(7×7) by noncontact atomic force microscopy with a force sensor based on a quartz tuning fork, Applied Physics Letters, 76 (2000) 1470-1472.

[45] T. Fukuma, M. Kimura, K. Kobayashi, K. Matsushige, H. Yamada, Development of low noise cantilever deflection sensor for multienvironment frequency-modulation atomic force microscopy, Review of Scientific Instruments, 76 (2005) 053704.

[46] T. Fukuma, T. Ichii, K. Kobayashi, H. Yamada, K. Matsushige, True-molecular resolution imaging by frequency modulation atomic force microscopy in various environments, Applied Physics Letters, 86 (2005) 034103.

[47] T. Fukuma, K. Kobayashi, K. Matsushige, H. Yamada, True molecular resolution in liquid by frequency-modulation atomic force microscopy, Applied Physics Letters, 86 (2005) 193108.

[48] T. Fukuma, K. Kobayashi, K. Matsushige, H. Yamada, True atomic resolution in liquid by frequency-modulation atomic force microscopy, Applied Physics Letters, 87 (2005) 034101.

[49] S. Ido, K. Kimura, N. Oyabu, K. Kobayashi, M. Tsukada, K. Matsushige, H. Yamada, Beyond the Helix Pitch: Direct Visualization of Native DNA in Aqueous Solution, ACS Nano, 7 (2013) 1817-1822.

[50] B. Schuler, S. Fatayer, F. Mohn, N. Moll, N. Pavliček, G. Meyer, D. Peña, L. Gross, Reversible Bergman cyclization by atomic manipulation, Nature Chemistry, 8 (2016) 220-224.

[51] S.P. Jarvis, H. Tokumoto, H. Yamada, K. Kobayashi, A. Toda, Alternative method for the activation and measurement of lateral forces using magnetically controlled atomic force microscopy, Applied Physics Letters, 75 (1999) 3883-3885.

[52] J.I. Kilpatrick, A. Gannepalli, J.P. Cleveland, S.P. Jarvis, Frequency modulation atomic force microscopy in ambient environments utilizing robust feedback tuning, Review of Scientific Instruments, 80 (2009) 023701.

[53] M. Jaafar, D. Martínez-Martín, M. Cuenca, J. Melcher, A. Raman, J. Gómez-Herrero, Drive-amplitude-modulation atomic force microscopy: From vacuum to liquids, Beilstein Journal of Nanotechnology, 3 (2012) 336-344.

[54] R. García, A. San Paulo, Attractive and repulsive tip-sample interaction regimes in tapping-mode atomic force microscopy, Physical Review B, 60 (1999) 4961-4967.

[55] R. Garcia, E.T. Herruzo, The emergence of multifrequency force microscopy, Nature Nanotechnology, 7 (2012) 217-226.

[56] J. Legleiter, M. Park, B. Cusick, T. Kowalewski, Scanning probe acceleration microscopy (SPAM) in fluids: Mapping mechanical properties of surfaces at the nanoscale, Proceedings of the National Academy of Sciences of the United States of America, 103 (2006) 4813-4818.

[57] R.W. Stark, W.M. Heckl, Higher harmonics imaging in tapping-mode atomic-force microscopy, Review of Scientific Instruments, 74 (2003) 5111-5114.

[58] J. Schiener, S. Witt, M. Stark, R. Guckenberger, Stabilized atomic force microscopy imaging in liquids using second harmonic of cantilever motion for setpoint control, Review of Scientific Instruments, 75 (2004) 2564-2568.

[59] T.R. Rodriguez, R. Garcia, Compositional mapping of surfaces in atomic force microscopy by excitation of the second normal mode of the microcantilever, Applied Physics Letters, 84 (2004) 449-451.

[60] N.F. Martinez, J.L. Lozano, E.T. Herruzo, F. Garcia, C. Richter, T. Sulzbach, R. Garcia, Bimodal atomic force microscopy imaging of isolated antibodies in air and liquids, Nanotechnology, 19 (2008).

[61] C. Dietz, M. Zerson, C. Riesch, A.M. Gigler, R.W. Stark, N. Rehse, R. Magerle, Nanotomography with enhanced resolution using bimodal atomic force microscopy, Applied Physics Letters, 92 (2008) 143107.

[62] S. Kawai, S.-i. Kitamura, D. Kobayashi, S. Meguro, H. Kawakatsu, An ultrasmall amplitude operation of dynamic force microscopy with second flexural mode, Applied Physics Letters, 86 (2005) 193107.

[63] J.W. Li, J.P. Cleveland, R. Proksch, Bimodal magnetic force microscopy: Separation of short and long range forces, Applied Physics Letters, 94 (2009) 163118.

[64] E.T. Herruzo, A.P. Perrino, R. Garcia, Fast nanomechanical spectroscopy of soft matter, Nature Communications, 5 (2014).

[65] C. Moreno, O. Stetsovych, T.K. Shimizu, O. Custance, Imaging Three-Dimensional Surface Objects with Submolecular Resolution by Atomic Force Microscopy, Nano Letters, 15 (2015) 2257-2262.

[66] M. Dong, O. Sahin, A nanomechanical interface to rapid single-molecule interactions, Nature Communications, 2 (2011) 247.

[67] G.S. Shekhawat, V.P. Dravid, Nanoscale Imaging of Buried Structures via Scanning Near-Field Ultrasound Holography, Science, 310 (2005) 89-92.

[68] S. Patil, N.F. Martinez, J.R. Lozano, R. Garcia, Force microscopy imaging of individual protein molecules with sub-pico Newton force sensitivity, Journal of Molecular Recognition, 20 (2007) 516-523.

[69] D. Martinez-Martin, E. Herruzo, C. Dietz, J. Gomez-Herrero, R. Garcia, Noninvasive Protein Structural Flexibility Mapping by Bimodal Dynamic Force Microscopy, Physical Review Letters, 106 (2011) 198101.

[70] M. Radmacher, J.P. Cleveland, M. Fritz, H.G. Hansma, P.K. Hansma, Mapping interaction forces with the atomic force microscope, Biophysical Journal, 66 (1994) 2159-2165.

[71] A. Rosa-Zeiser, E. Weilandt, S. Hild, O. Marti, The simultaneous measurement of elastic, electrostatic and adhesive properties by scanning force microscopy: pulsed-force mode operation, Measurement Science and Technology, 8 (1997) 1333.

[72] P.J. de Pablo, J. Colchero, J. Gómez-Herrero, A.M. Baró, Jumping mode scanning force microscopy, Applied Physics Letters, 73 (1998) 3300-3302.

[73] A. Ortega-Esteban, I. Horcas, M. Hernando-Pérez, P. Ares, A.J. Pérez-Berná, C. San Martín, J.L. Carrascosa, P.J. de Pablo, J. Gómez-Herrero, Minimizing tip–sample forces in jumping mode atomic force microscopy in liquid, Ultramicroscopy, 114 (2012) 56-61.

[74] K. Yamanaka, H. Ogiso, O. Kolosov, Ultrasonic force microscopy for nanometer resolution subsurface imaging, Applied Physics Letters, 64 (1994) 178-180.

[75] U. Rabe, W. Arnold, Acoustic microscopy by atomic force microscopy, Applied Physics Letters, 64 (1994) 1493-1495.

[76] B.J. Rodriguez, C. Callahan, S.V. Kalinin, R. Proksch, Dual-frequency resonance-tracking atomic force microscopy, Nanotechnology, 18 (2007) 475504.

[77] S. Jesse, S.V. Kalinin, R. Proksch, A.P. Baddorf, B.J. Rodriguez, The band excitation method in scanning probe microscopy for rapid mapping of energy dissipation on the nanoscale, Nanotechnology, 18 (2007) 435503.

[78] M. Dokukin, I. Sokolov, High-resolution high-speed dynamic mechanical spectroscopy of cells and other soft materials with the help of atomic force microscopy, Scientific Reports, 5 (2015) 12630.

[79] D. Platz, E.A. Tholén, D. Pesen, D.B. Haviland, Intermodulation atomic force microscopy, Applied Physics Letters, 92 (2008) 153106.

[80] O. Sahin, S. Magonov, C. Su, C.F. Quate, O. Solgaard, An atomic force microscope tip designed to measure time-varying nanomechanical forces, Nature Nanotechnology, 2 (2007) 507-514.

[81] S. Ozgur, E. Natalia, High-resolution and large dynamic range nanomechanical mapping in tapping-mode atomic force microscopy, Nanotechnology, 19 (2008) 445717.

[82] M. Dong, S. Husale, O. Sahin, Determination of protein structural flexibility by microsecond force spectroscopy, Nature Nanotechnology, 4 (2009) 514-517.

[83] D. Kim, O. Sahin, Imaging and three-dimensional reconstruction of chemical groups inside a protein complex using atomic force microscopy, Nature Nanotechnology, 10 (2015) 264-269.

[84] A. Raman, S. Trigueros, A. Cartagena, A.P.Z. Stevenson, M. Susilo, E. Nauman, S. Antoranz Contera, Mapping nanomechanical properties of live cells using multi-harmonic atomic force microscopy, Nature Nanotechnology, 6 (2011) 809-814.

[85] C.-Y. Lai, S. Santos, M. Chiesa, General interpretation and theory of apparent height in dynamic atomic force microscopy, RSC Advances, 5 (2015) 80069-80075.

[86] S. Santos, V. Barcons, H.K. Christenson, J. Font, N.H. Thomson, The Intrinsic Resolution Limit in the Atomic Force Microscope: Implications for Heights of Nano-Scale Features, PLoS ONE, 6 (2011) e23821.

[87] A. Verdaguer, S. Santos, G. Sauthier, J.J. Segura, M. Chiesa, J. Fraxedas, Water-mediated height artifacts in dynamic atomic force microscopy, Physical Chemistry Chemical Physics, 14 (2012) 16080-16087.

[88] S. Santos, A. Verdaguer, M. Chiesa, The effects of adsorbed water layers on the apparent height of nanostructures in ambient amplitude modulation atomic force microscopy, The Journal of Chemical Physics, 137 (2012) 044201.

[89] Y. Chih-Wen, H. Ing-Shouh, C. Yen Fu, C. Chia Seng, T. Din Ping, Imaging of soft matter with tapping-mode atomic force microscopy and non-contact-mode atomic force microscopy, Nanotechnology, 18 (2007) 084009.

[90] E. Palacios-Lidón, B. Pérez-García, J. Colchero, Enhancing dynamic scanning force microscopy in air: as close as possible, Nanotechnology, 20 (2009) 085707.

[91] J. Font, S. Santos, V. Barcons, N.H. Thomson, A. Verdaguer, M. Chiesa, Spatial horizons in amplitude and frequency modulation atomic force microscopy, Nanoscale, 4 (2012) 2463-2469.

[92] H. Sekiguchi, T. Okajima, H. Arakawa, S. Maeda, A. Takashima, A. Ikai, Frequency shift feedback imaging in liquid for biological molecules, Applied Surface Science, 210 (2003) 61-67.

[93] Y. Chih-Wen, L. Yi-Hsien, H. Ing-Shouh, Imaging surface nanobubbles at graphite–water interfaces with different atomic force microscopy modes, Journal of Physics: Condensed Matter, 25 (2013) 184010.

[94] E. Palacios-Lidón, C. Munuera, C. Ocal, J. Colchero, Contrast inversion in non-contact Dynamic Scanning Force Microscopy: What is high and what is low?, Ultramicroscopy, 110 (2010) 789-800.

[95] Y. Maeda, T. Matsumoto, T. Kawai, Observation of single- and double-stranded DNA using non-contact atomic force microscopy, Applied Surface Science, 140 (1999) 400-405.

[96] D.J. Müller, A. Engel, The height of biomolecules measured with the atomic force microscope depends on electrostatic interactions, Biophysical Journal, 73 1633-1644.

[97] J. Israelachvili, Intermolecular and surface forces, Academic Press, London, 1994.

[98] I. Horcas, R. Fernández, J.M. Gómez-Rodríguez, J. Colchero, J. Gómez-Herrero, A.M. Baro, WSXM: A software for scanning probe microscopy and a tool for nanotechnology, Review of Scientific Instruments, 78 (2007) 013705.

[99] F. Ostendorf, C. Schmitz, S. Hirth, A. Kühnle, J.J. Kolodziej, M. Reichling, How flat is an air-cleaved mica surface?, Nanotechnology, 19 (2008) 305705.

[100] C. Bustamante, J. Vesenka, C.L. Tang, W. Rees, M. Guthold, R. Keller, Circular DNA molecules imaged in air by scanning force microscopy, Biochemistry, 31 (1992) 22-26.

[101] H.G. Hansma, J. Vesenka, C. Siegerist, G. Kelderman, H. Morrett, R.L. Sinsheimer, V. Elings, C. Bustamante, P.K. Hansma, Reproducible Imaging and Dissection of Plasmid DNA Under Liquid with the Atomic Force Microscope, Science, 256 (1992) 1180-1184.

[102] A. Ikai, The world of nano-biomechanics: mechanical imaging and measurement by atomic force microscopy, Elsevier, 2007.

[103] A.P. Perrino, R. Garcia, How soft is a single protein? The stress-strain curve of antibody pentamers with 5 pN and 50 pm resolutions, Nanoscale, 8 (2016) 9151-9158.

[104] S. Hu, A. Raman, Analytical formulas and scaling laws for peak interaction forces in dynamic atomic force microscopy, Applied Physics Letters, 91 (2007) 123106.

[105] E.T. Herruzo, R. Garcia, Theoretical study of the frequency shift in bimodal FM-AFM by fractional calculus, Beilstein Journal of Nanotechnology, 3 (2012) 198-206.

[106] R. Herrmann, Fractional Calculus, an Introduction for Physicists World Scientific, Singapore, 2011.

[107] J.E. Sader, S.P. Jarvis, Accurate formulas for interaction force and energy in frequency modulation force spectroscopy, Applied Physics Letters, 84 (2004) 1801-1803.

[108] H.V. Guzman, P.D. Garcia, R. Garcia, Dynamic force microscopy simulator (dForce): A tool for planning and understanding tapping and bimodal AFM experiments, Beilstein Journal of Nanotechnology, 6 (2015) 369-379.

[109] D.M. Czajkowsky, Z. Shao, The human IgM pentamer is a mushroom-shaped molecule with a flexural bias, Proceedings of the National Academy of Sciences, 106 (2009) 14960-14965.

[110] H. Frauenfelder, S. Sligar, P. Wolynes, The energy landscapes and motions of proteins, Science, 254 (1991) 1598-1603.

[111] F. Rico, A. Rigato, L. Picas, S. Scheuring, Mechanics of proteins with a focus on atomic force microscopy, Journal of Nanobiotechnology, 11 (2013) S3.

[112] P. Egan, R. Sinko, P.R. LeDuc, S. Keten, The role of mechanics in biological and bio-inspired systems., Nature Communications, 6 (2015) 7418.

[113] Jacky G. Goetz, S. Minguet, I. Navarro-Lérida, Juan J. Lazcano, R. Samaniego, E. Calvo, M. Tello, T. Osteso-Ibáñez, T. Pellinen, A. Echarri, A. Cerezo, Andres J.P. Klein-Szanto, R. Garcia, Patricia J. Keely, P. Sánchez-Mateos, E. Cukierman, Miguel A. Del Pozo, Biomechanical Remodeling of the Microenvironment by Stromal Caveolin-1 Favors Tumor Invasion and Metastasis, Cell, 146 (2011) 148-163.

[114] T. Ackbarow, X. Chen, S. Keten, M.J. Buehler, Hierarchies, multiple energy barriers, and robustness govern the fracture mechanics of α-helical and β-sheet protein domains, Proceedings of the National Academy of Sciences, 104 (2007) 16410-16415.

[115] S. Zhang, M. Andreasen, J.T. Nielsen, L. Liu, E.H. Nielsen, J. Song, G. Ji, F. Sun, T. Skrydstrup, F. Besenbacher, N.C. Nielsen, D.E. Otzen, M. Dong, Coexistence of ribbon and helical fibrils originating from hIAPP20–29 revealed by quantitative nanomechanical atomic force microscopy, Proceedings of the National Academy of Sciences, 110 (2013) 2798-2803.

[116] N. Chiaruttini, L. Redondo-Morata, A. Colom, F. Humbert, M. Lenz, S. Scheuring, A. Roux, Relaxation of Loaded ESCRT-III Spiral Springs Drives Membrane Deformation, Cell, 163 (2015) 866-879.

[117] W.E. Paul, Fundamental Immunology, Lippincott Williams & Wilkins, , Philadelphia, 2003.

[118] H.F. Boyer, Atlas of stress-strain curves, ASM International, 2002.

[119] G. Zaccai, How Soft Is a Protein? A Protein Dynamics Force Constant Measured by Neutron Scattering, Science, 288 (2000) 1604-1607.

[120] A. Ariyaratne, C. Wu, C.-Y. Tseng, G. Zocchi, Dissipative Dynamics of Enzymes, Physical Review Letters, 113 (2014) 198101.

[121] Y.F. Dufrene, D. Martinez-Martin, I. Medalsy, D. Alsteens, D.J. Muller, Multiparametric imaging of biological systems by force-distance curve-based AFM, Nature Methods, 10 (2013) 847-854.

[122] I.D. Medalsy, D.J. Müller, Nanomechanical Properties of Proteins and Membranes Depend on Loading Rate and Electrostatic Interactions, ACS Nano, 7 (2013) 2642-2650.

[123] F. Rico, C. Su, S. Scheuring, Mechanical Mapping of Single Membrane Proteins at Submolecular Resolution, Nano Letters, 11 (2011) 3983-3986.

[124] J. Preiner, A. Horner, A. Karner, N. Ollinger, C. Siligan, P. Pohl, P. Hinterdorfer, High-Speed AFM Images of Thermal Motion Provide Stiffness Map of Interfacial Membrane Protein Moieties, Nano Letters, 15 (2015) 759-763.

[125] A. Ikai, The World of Nano-Biomechanics, in, Elsevier B.V. , Amsterdam, The Netherlands, 2008, pp. 148-154.

[126] A. Ikai, R. Afrin, H. Sekiguchi, Pulling and pushing protein molecules by AFM, Current Nanoscience, 3 (2007) 17-29.

[127] M. Pfreundschuh, D. Alsteens, M. Hilbert, M.O. Steinmetz, D.J. Müller, Localizing Chemical Groups while Imaging Single Native Proteins by High-Resolution Atomic Force Microscopy, Nano Letters, 14 (2014) 2957-2964.

[128] A. Voss, C. Dietz, A. Stocker, R. Stark, Quantitative measurement of the mechanical properties of human antibodies with sub-10-nm resolution in a liquid environment, Nano Res., (2015) 1-10.

[129] H. Hertz, On the Contact Elastic Solids J. Reine Angew. Math, (1881) 25.

[130] E.K. Dimitriadis, F. Horkay, J. Maresca, B. Kachar, R.S. Chadwick, Determination of Elastic Moduli of Thin Layers of Soft Material Using the Atomic Force Microscope, Biophysical Journal, 82 2798-2810.

[131] B.B. Akhremitchev, G.C. Walker, Finite Sample Thickness Effects on Elasticity Determination Using Atomic Force Microscopy, Langmuir, 15 (1999) 4.

[132] K.D. Costa, F.C.P. Yin, Analysis of Indentation: Implications for Measuring Mechanical Properties With Atomic Force Microscopy, Journal of Biomechanical Engineering 121 (1999) 10.

[133] H.P. Vollmers, S. Brändlein, Natural IgM antibodies: The orphaned molecules in immune surveillance, Advanced Drug Delivery Reviews, 58 (2006) 755-765.

[134] H.P. Vollmers, S. Brändlein, Natural antibodies and cancer, Journal of Autoimmunity, 29 (2007) 295-302.

[135] S. Ido, H. Kimiya, K. Kobayashi, H. Kominami, K. Matsushige, H. Yamada, Immunoactive two-dimensional self-assembly of monoclonal antibodies in aqueous solution revealed by atomic force microscopy, Nature Materials, 13 (2014) 264-270.

[136] N.H. Thomson, The substructure of immunoglobulin G resolved to 25kDa using amplitude modulation AFM in air, Ultramicroscopy, 105 (2005) 103-110.

[137] B. Gotsmann, C. Seidel, B. Anczykowski, H. Fuchs, Conservative and dissipative tip-sample interaction forces probed with dynamic AFM, Physical Review B, 60 (1999) 11051-11061.

[138] C. Loppacher, R. Bennewitz, O. Pfeiffer, M. Guggisberg, M. Bammerlin, S. Schär, V. Barwich, A. Baratoff, E. Meyer, Experimental aspects of dissipation force microscopy, Physical Review B, 62 (2000) 13674-13679.

[139] V. Vahdat, R.W. Carpick, Practical Method to Limit Tip–Sample Contact Stress and Prevent Wear in Amplitude Modulation Atomic Force Microscopy, ACS Nano, 7 (2013) 9836-9850.

[140] V. Vahdat, D.S. Grierson, K.T. Turner, R.W. Carpick, Mechanics of Interaction and Atomic-Scale Wear of Amplitude Modulation Atomic Force Microscopy Probes, ACS Nano, 7 (2013) 3221-3235.

[141] M. Singh-Zocchi, J. Hanne, G. Zocchi, Plastic Deformation of Protein Monolayers, Biophysical Journal, 83 2211-2218.

[142] T. Hoffmann, L. Dougan, Single molecule force spectroscopy using polyproteins, Chemical Society Reviews, 41 (2012) 4781-4796.

[143] J. Gosline, M. Lillie, E. Carrington, P. Guerette, C. Ortlepp, K. Savage, Elastic Proteins: Biological Roles and Mechanical Properties, Philosophical Transactions: Biological Sciences, 357 (2002) 121-132.

[144] A. Gautieri, S. Vesentini, A. Redaelli, M.J. Buehler, Hierarchical Structure and Nanomechanics of Collagen Microfibrils from the Atomistic Scale Up, Nano Letters, 11 (2011) 757-766.

[145] L.F. Deravi, T. Su, J.A. Paten, J.W. Ruberti, K. Bertoldi, K.K. Parker, Differential Contributions of Conformation Extension and Domain Unfolding to Properties of Fibronectin Nanotextiles, Nano Letters, 12 (2012) 5587-5592.

[146] T. Uchihashi, R. Iino, T. Ando, H. Noji, High-Speed Atomic Force Microscopy Reveals Rotary Catalysis of Rotorless F1-ATPase, Science, 333 (2011) 755-758.

[147] H. Asakawa, K. Ikegami, M. Setou, N. Watanabe, M. Tsukada, T. Fukuma, Submolecular-Scale Imaging of α-Helices and C-Terminal Domains of Tubulins by Frequency Modulation Atomic Force Microscopy in Liquid, Biophysical Journal, 101 (2011) 1270-1276.

[148] I. Casuso, J. Khao, M. Chami, P. Paul-Gilloteaux, M. Husain, J.-P. Duneau, H. Stahlberg, J.N. Sturgis, S. Scheuring, Characterization of the motion of membrane proteins using high-speed atomic force microscopy, Nature Nanotechnology, 7 (2012) 525-529.

[149] J.A. Firth, Endothelial barriers: from hypothetical pores to membrane proteins, Journal of Anatomy, 200 (2002) 541-548.

[150] L. Tetard, A. Passian, K.T. Venmar, R.M. Lynch, B.H. Voy, G. Shekhawat, V.P. Dravid, T. Thundat, Imaging nanoparticles in cells by nanomechanical holography, Nature Nanotechnology, 3 (2008) 501-505.

[151] S. Kawai, F.F. Canova, T. Glatzel, T. Hynninen, E. Meyer, A.S. Foster, Measuring Electric Field Induced Subpicometer Displacement of Step Edge Ions, Physical Review Letters, 109 (2012) 146101.

[152] H.-J. Butt, B. Cappella, M. Kappl, Force measurements with the atomic force microscope: Technique, interpretation and applications, Surface Science Reports, 59 (2005) 1-152.

[153] M.D. Aksoy, A. Atalar, Force spectroscopy using bimodal frequency modulation atomic force microscopy, Physical Review B, 83 (2011) 075416.

[154] F.J. Giessibl, Forces and frequency shifts in atomic-resolution dynamic-force microscopy, Physical Review B, 56 (1997) 16010-16015.

[155] J.E. Sader, S.P. Jarvis, Interpretation of frequency modulation atomic force microscopy in terms of fractional calculus, Physical Review B, 70 (2004) 012303.

[156] J.E. Sader, T. Uchihashi, M.J. Higgins, A. Farrell, Y. Nakayama, S.P. Jarvis, Quantitative force measurements using frequency modulation atomic force microscopy—theoretical foundations, Nanotechnology, 16 (2005) S94.

[157] D. Ebeling, S.D. Solares, Amplitude modulation dynamic force microscopy imaging in liquids with atomic resolution: comparison of phase contrasts in single and dual mode operation, Nanotechnology, 24 (2013) 135702.

[158] D. Kiracofe, A. Raman, D. Yablon, Multiple regimes of operation in bimodal AFM: understanding the energy of cantilever eigenmodes, Beilstein Journal of Nanotechnology, 4 (2013) 385-393.

[159] C. Ishita, G.Y. Dalia, Cantilever energy effects on bimodal AFM: phase and amplitude contrast of multicomponent samples, Nanotechnology, 24 (2013) 475706.

[160] S. Basak, A. Raman, S.V. Garimella, Hydrodynamic loading of microcantilevers vibrating in viscous fluids, Journal of Applied Physics, 99 (2006) 114906.

[161] L. Oria, A. Ruiz de Luzuriaga, J.A. Alduncin, F. Perez-Murano, Polystyrene as a brush layer for directed self-assembly of block co-polymers, Microelectronic Engineering, 110 (2013) 234-240.

[162] M. Chyasnavichyus, S.L. Young, V.V. Tsukruk, Probing of Polymer Surfaces in the Viscoelastic Regime, Langmuir, 30 (2014) 10566-10582.

[163] K. Johnson, J. Greenwood, An adhesion map for the contact of elastic spheres, Journal of colloid and interface science, 192 (1997) 326-333.

[164] J.R. Lozano, D. Kiracofe, J. Melcher, R. Garcia, A. Raman, Calibration of higher eigenmode spring constants of atomic force microscope cantilevers, Nanotechnology, 21 (2010) 465502.

[165] A. Labuda, M. Kocun, M. Lysy, T. Walsh, J. Meinhold, T. Proksch, W. Meinhold, C. Anderson, R. Proksch, Calibration of higher eigenmodes of cantilevers, Review of Scientific Instruments, 87 (2016) 073705.

[166] M.E. Dokukin, I. Sokolov, On the Measurements of Rigidity Modulus of Soft Materials in Nanoindentation Experiments at Small Depth, Macromolecules, 45 (2012) 4277-4288.

[167] M.E. Dokukin, I. Sokolov, Quantitative Mapping of the Elastic Modulus of Soft Materials with HarmoniX and PeakForce QNM AFM Modes, Langmuir, 28 (2012) 16060-16071.

[168] A. Knoll, R. Magerle, G. Krausch, Tapping Mode Atomic Force Microscopy on Polymers: Where Is the True Sample Surface?, Macromolecules, 34 (2001) 4159-4165.

[169] J. Legleiter, The effect of drive frequency and set point amplitude on tapping forces in atomic force microscopy: simulation and experiment, Nanotechnology, 20 (2009) 245703.

[170] A.F. Payam, A.P. Perrino, C.A. Amo, R. Garcia, Fast bimodal force spectroscopy in liquid with atomic and molecular resolution, (Unpublished).

[171] H. Hölscher, U.D. Schwarz, Theory of amplitude modulation atomic force microscopy with and without Q-Control, International Journal of Non-Linear Mechanics, 42 (2007) 608-625.

[172] F. Gandara, N. Snejko, A.d. Andres, J.R. Fernandez, J.C. Gomez-Sal, E. Gutierrez-Puebla, A. Monge, Stable organic radical stacked by in situ coordination to rare earth cations in MOF materials, RSC Advances, 2 (2012) 949-955.

[173] I. Medalsy, U. Hensen, D.J. Muller, Imaging and Quantifying Chemical and Physical Properties of Native Proteins at Molecular Resolution by Force–Volume AFM, Angewandte Chemie International Edition, 50 (2011) 12103-12108.

[174] D.J. Müller, D. Fotiadis, S. Scheuring, S.A. Müller, A. Engel, Electrostatically Balanced Subnanometer Imaging of Biological Specimens by Atomic Force Microscope, Biophysical Journal, 76 (1999) 1101-1111.

[175] K. Voïtchovsky, S.A. Contera, M. Kamihira, A. Watts, J. Ryan, Differential stiffness and lipid mobility in the leaflets of purple membranes, Biophysical journal, 90 (2006) 2075-2085.

[176] A. Corcelli, V.M.T. Lattanzio, G. Mascolo, P. Papadia, F. Fanizzi, Lipid-protein stoichiometries in a crystalline biological membrane: NMR quantitative analysis of the lipid extract of the purple membrane, Journal of Lipid Research, 43 (2002) 132-140.

[177] K. Voïtchovsky, Anharmonicity, solvation forces, and resolution in atomic force microscopy at the solid-liquid interface, Physical Review E, 88 (2013) 022407.

Publications list

1. H.V. Guzman, **A.P. Perrino** and R. Garcia, *Peak forces in high-resolution imaging of soft matter in liquid*, *ACS Nano,* **4**, 3198-3204 (2013).

2. E.T. Herruzo, **A.P. Perrino** and R. Garcia, *Fast nanomechanical spectroscopy of soft matter, Nature Communications*, **5,** 3126-3204 (2014).

3. **A.P. Perrino** and R. Garcia, *How soft is a single protein?: Stress-Strain curve of antibody pentamers with 5 pN and 50 pm resolutions*, *resolutions*, *Nanoscale*, **8,** 9151-9158 (2016).

4. **A.P. Perrino**, Y.K. Ryu, C.A. Amo, M.P. Morales and R. Garcia, *Subsurface imaging of silicon nanowires circuits and iron oxide nanoparticles with sub-10 nm spatial resolution*, *Nanotechnology*, **27**, 275703 (2016).

5. J. Rodriguez-Ramos, **A.P. Perrino** and R. Garcia. *Dependence of the volume of an antibody on the force applied in a force microscopy experiment in liquid. Ultramicroscopy,* **171,** 153 (2016).

6. Amir F. Payam, **A.P. Perrino,** C.A. Amo and R. Garcia. *Fast bimodal force spectroscopy in liquid with atomic and molecular resolution.* In preparation.

7. **A.P. Perrino** and R. Garcia, *Influence of the force in AFM dynamic modes for biomolecules imaging.* In preparation